

**VIRTUAL MODELING OF A MANUFACTURING PROCESS TO CONSTRUCT  
COMPLEX COMPOSITE MATERIALS OF TAILORED PROPERTIES**

A Dissertation  
Presented to  
The Academic Faculty

By

Sima Didari

In Partial Fulfillment  
Of the Requirements for the Degree  
Doctor of Philosophy in Mechanical Engineering

Georgia Institute of Technology

May 2014

Copyright © Sima Didari 2014

Approved by:

Dr. Tequila A. L. Harris, Advisor  
G.W. Woodruff School of Mechanical  
Engineering  
*Georgia Institute of Technology*

Dr. Sankar Nair  
School of Chemical & Biomolecular  
Engineering  
*Georgia Institute of Technology*

Dr. Alexander Alexeev  
G.W. Woodruff School of Mechanical  
Engineering  
*Georgia Institute of Technology*

Dr. Yan Wang  
G.W. Woodruff School of Mechanical  
Engineering  
*Georgia Institute of Technology*

Dr. S. Mostafa Ghiaasiaan  
G.W. Woodruff School of Mechanical  
Engineering  
*Georgia Institute of Technology*

Date Approved: 01/21/2014

Dedicated to Dr. Yaser Bastani,

Without you the story of my life would be very different.

## ACKNOWLEDGEMENTS

First, I would like to thank my adviser Dr. Harris, who changed my life by giving me the opportunity to join her research group. I am really thankful for her advice, guidance and mentorship during my Ph.D. study. Without her continuous support I would not be able to accomplish my research tasks.

I would like to extend my appreciation to committee members: Dr. Alexeev, Dr. Ghiaasiaan, Dr. Nair and Dr. Wang for providing valuable research advice and insightful comments for the improvement of this work. I would like to specially thank Dr. Wang for his support and guidance through this project and giving me the opportunity to collaborate with his research group.

I would also like to thank Kanthi Bhamidipati, Xiaoyu Ding, Wei Huang, Zak Ahmad, and James Veldhorst for their collaboration in several parts of this work.

My parents, Robabeh Ghasemi and Jamshid Didari, my sister Sara and my brother Saeed, being far from you during my Ph.D. study was very painful. I cannot thank you enough for all of your love and encouragement during these years.

## TABLE OF CONTENTS

<b>ACKNOWLEDGEMENTS .....</b>	<b>iv</b>
<b>LIST OF TABLES .....</b>	<b>ix</b>
<b>LIST OF FIGURES .....</b>	<b>xi</b>
<b>NOMENCLATURE.....</b>	<b>xviii</b>
<b>SUMMARY .....</b>	<b>xxii</b>
<b>CHAPTER 1: INTRODUCTION.....</b>	<b>1</b>
1.1 Fibrous Porous Media and Their Structures .....	2
1.2 Application of Porous Media in the Energy Sector .....	6
1.2.1 Working Principle of Polymer Electrolyte Membrane Fuel Cells.....	7
1.2.2 Porous Media Used in PEMFCs .....	8
1.3 Research Motivations.....	10
1.4 Research Objectives.....	12
1.5 Key Question and Research Tasks.....	13
1.6 Thesis Layout .....	14
1.7 Summary.....	16
<b>CHAPTER 2: BACKGROUND .....</b>	<b>18</b>
2.1 Virtual Representation of Fibrous Porous Structures .....	19
2.2 Reconstruction of GDLs' Microstructure using Imaging Techniques.....	28
2.3 Geometrical Modeling of GDLs' Microstructure .....	31
2.4 Determining the Morphological Properties of Porous Media.....	33
2.4.1 Experimental Methods for Determining Morphological Properties of Porous Media .....	34
2.4.2 Numerical Methods for Determining Morphological Properties of Porous Media.....	38
2.5 Determining the Transport Properties of Porous Structures .....	42
2.6 Numerical Analysis of Complex Porous Media .....	46
2.6.1 Fabrication of Complex Porous Media .....	46
2.6.2 Penetration of Coating Solution into the Porous Media .....	47
2.7 Summary .....	51
<b>CHAPTER 3: MATERIALS .....</b>	<b>53</b>
<b>CHAPTER 4: GEOMETRICAL MODELING OF FIBROUS POROUS MEDIA, METHODOLOGY .....</b>	<b>54</b>
4.1 Periodic Surface Modeling Methodology.....	54
4.2 Periodic Surface Modeling of Paper Porous Media.....	56

4.3	Periodic Surface Modeling of Felt Porous Media.....	60
4.3.1	Rotation of the Generalized PS Model .....	61
4.3.2	Translation of the Generalized PS model .....	64
4.4	Periodic Surface Model for Woven Porous Media.....	67
4.5	Summary .....	69

**CHAPTER 5: GEOMETRICAL MODELING OF FIBROUS POROUS MEDIA, RESULTS ..... 70**

5.1	Periodic Surface Modeling of Carbon Paper Gas Diffusion Layers.....	70
5.2	Periodic Surface Modeling of Felt Gas Diffusion Layers .....	79
5.2.1	Geometrical Modeling of Felt Gas Diffusion Layers using Generalized PS Model.....	80
5.2.2	Energy Coupled Modeling of Felt Gas Diffusion Layers using Generalized PS Model.....	83
5.2.3	Effect of Optimization on the Characteristics of Virtual Felt GDL.....	87
5.3	Periodic Surface Modeling of Cloth Gas Diffusion Layers.....	90
5.4	Periodic Surface Modeling of Carbon Paper Gas Diffusion Layers Including the Binder.....	92
5.5	Summary .....	95

**CHAPTER 6: MORPHOLOGICAL CHARACTERIZATION OF FIBROUS POROUS MEDIA, METHODOLOGY ..... 97**

6.1	Extracting Binary Representation of Porous Media .....	97
6.2	Determining Porosity of Porous Media .....	99
6.3	Determining Pore Size Distribution of Porous Media .....	100
6.4	Determining Chord Length Distribution of Porous Media.....	101
6.5	Determining the Shortest Paths Distribution of Porous Media.....	102
6.6	Skeletonization of porous medium .....	104
6.7	Summary .....	105

**CHAPTER 7: MORPHOLOGICAL CHARACTERIZATION OF FIBROUS POROUS MEDIA, RESULTS..... 106**

7.1	Determining Morphological Properties of Carbon Paper GDL.....	106
7.2	Effect of Binder Modeling on the Characteristics of a Composite GDL.....	109
7.3	Effect of Binder Volume Fraction on the Morphological Properties of the GDL .....	112
7.4	Determining Morphological Properties of Felt GDL.....	116
7.5	Summary .....	121

**CHAPTER 8: TRANSPORT PROPERTIES OF FIBROUS POROUS MEDIA, METHODOLOGY ..... 124**

8.1	Mesh Generation for Computational Fluid Dynamic Simulations .....	124
8.1.1	Generating Volumetric Mesh for Geometries with Pre-Dominant Axes	125
8.1.2	Generating Surface Mesh for Complex Geometries.....	127
8.1.3	Generating Volumetric Mesh for Complex Geometries.....	129

8.2	Determining Permeability Tensor of Porous Media .....	132
8.2.1	Governing Equation .....	133
8.2.2	Computational Domain and Boundary Conditions .....	133
8.2.3	Numerical Discretization .....	134
8.2.4	Mesh Study .....	135
8.2.5	Determining Size of RVE .....	136
8.3	Determining Tortuosity of Porous Media .....	140
8.4	Determining Diffusivity of Porous Media .....	141
8.4.1	Determining the Diffusion Mode .....	142
8.4.2	Governing Equations and Computational Domain .....	143
8.5	Determining Tortuosity Factor of Porous Media .....	144
8.6	Summary .....	145
<b>CHAPTER 9: TRANSPORT PROPERTIES OF FIBROUS POROUS MEDIA, RESULTS .....</b>		<b>146</b>
9.1	Transport Properties of Paper, Felt and Woven Gas Diffusion Layers .....	146
9.2	Interplay of Morphological and Transport Properties of Porous Structure ...	150
9.3	Effects of Matrix Properties on the Characteristics of Composite Media .....	153
9.4	Effects of Porosity of Felt Porous Media on the Transport Properties .....	155
9.5	Summary .....	157
<b>CHAPTER 10: VIRTUAL CHARACTERIZATION OF COMPLEX POROUS MEDIA, METHODOLOGY .....</b>		<b>159</b>
10.1	Multi Scale Simulation Approach for Modeling Coating Process .....	159
10.2	Macro Scale Modeling of Coating Process .....	163
10.2.1	Governing Equations .....	164
10.2.2	Computational Domain and Boundary Conditions .....	165
10.2.3	Verification of the Numerical Method .....	166
10.3	Micro Scale Simulation of Penetration Process .....	168
10.3.1	Boundary Conditions of the Micro Scale Simulation .....	169
10.3.2	Governing Equations .....	170
10.4	Summary .....	171
<b>CHAPTER 11: VIRTUAL CHARACTERIZATION OF COMPLEX POROUS MEDIA, RESULTS .....</b>		<b>172</b>
11.1	Coupling of Flow Field in the Coating Bead and Porous Media .....	172
11.2	Effect of Operating Conditions on the Penetration of Coating Solution into the Porous Web .....	174
11.3	Effect of Viscosity and Surface Tension of the Coating Solution on the Penetration into the Porous Web .....	182
11.4	Summary .....	186
<b>CHAPTER 12: CONCLUSION AND CONTRIBUTIONS .....</b>		<b>188</b>
12.1	Conclusions .....	190
12.1.1	Virtual Representation of Porous Media .....	190
12.1.2	Virtual Characterization of Porous Media .....	194

12.1.3	Analyzing Complex Porous Media.....	197
12.2	Key contributions.....	198
12.2.1	Fundamental contributions.....	198
12.2.2	Engineering contributions.....	199
<b>CHAPTER 13: FUTURE WORK.....</b>		<b>200</b>
13.1	Modeling non-Fibrous Porous Structures .....	200
13.2	Physics-based Empirical Force Field to Model Deformation of Fibers .....	201
13.3	Mechanical Behavior of Fibrous Porous Media .....	202
13.4	Coating of Porous Media .....	204
<b>REFERENCES.....</b>		<b>205</b>



## LIST OF TABLES

Table 2.1: The common types of tomography .....	20
Table 3.1: Properties of GDLs selected as the case studies in this research.....	53
Table 4.1: The parameters for the PS model of a rod shape .....	57
Table 4.2: The basis vectors for rods in x- direction and y- direction.....	57
Table 4.3: The elements of the rotation matrix.....	62
Table 4.4: The basis vectors for bent rods in x- direction and y- direction .....	67
Table 5.1: The genetic algorithm optimization procedure for minimizing the volume of intersection.....	76
Table 5.2: The intersection volume in geometrical modeling approach, porosity 0.78....	89
Table 5.3: The stored strain energy in geometrical modeling approach, porosity 0.78....	90
Table 5.4: Translation vectors of the six woven fibers.....	91
Table 7.1: The average chord lengths of felt GDL generated by the geometrical and energy coupled modeling approaches.....	117
Table 8.1: Through-plane permeability of paper GDL porosity of 0.82 and computational domain size of $100 \times 100 \times 100 \mu\text{m}$ according to the Brinkman screening length criteria. ....	138
Table 8.2: Through-plane permeability of paper GDL porosity of 0.82 and computational domain size of $200 \times 200 \times 200 \mu\text{m}$ . ....	138
Table 8.3: Through-plane permeability of paper GDL with binder, porosity of 0.78 computational domain size of $200 \times 200 \times 200 \mu\text{m}$ .....	139
Table 8.4: In-plane permeability of paper GDL porosity of 0.82 and computational domain size of $200 \times 200 \times 200 \mu\text{m}$ .....	139
Table 8.5: In-plane permeability of paper GDL with binder, porosity of 0.78 computational domain size of $200 \times 200 \times 200 \mu\text{m}$ .....	140

Table 8.6: In-plane and through-plane permeability of paper GDL with and without binder, computational domain size of $200 \times 200 \times 200 \mu\text{m}$ and $400 \times 400 \times 400 \mu\text{m}$ . .....	140
Table 8.7: Average Knudson number in Toray 060 GDL at $T=100^\circ\text{C}$ and $P=100 \text{ KPa}$ .	143
Table 9.1: Transport properties of Toray 060 GDL.....	148
Table 9.2: Transport properties of Freudenberg H2315 GDL.....	149
Table 9.3: Transport properties of woven GDL, in the through-plane direction.....	150
Table 9.4: Transport properties of Toray 060 GDL modeled with different structure elements .....	151
Table 9.5: Transport properties of Freudenberg H2315 GDL.....	152
Table 10.1: Material properties of glycerin .....	168
Table 11.1: Setting for determining the pressure distribution over the porous web.....	173
Table 11.2: Settings for simulation of penetration depth versus coating gap ( $H$ ) .....	176
Table 11.3: Settings for simulation of penetration depth versus slot gap ( $W$ ).....	179
Table 11.4: Settings for simulation of penetration depth versus Flow rate ( $Q$ ).....	180
Table 11.5: Settings for simulation of penetration depth versus coating speed ( $u_w$ ). ....	182
Table 11.6: Settings for simulation of penetration depth versus viscosity ( $\mu$ ) .....	183
Table 11.7: Settings for simulation of penetration versus surface tension ( $\sigma$ ).....	185
Table 12.1: The total curvature of fibers in the felt structures.....	194
Table 12.2: Effect of operating conditions on the penetration of the coating solution into the porous web. The arrows pointing up represent a proportional behavior while the arrows pointing down represents an inverse relationship between operating conditions and final penetration depth.....	198

## LIST OF FIGURES

Figure 1.1: The various applications of porous media.....	1
Figure 1.2: Common types of fibrous porous media, SEM image of (a) woven, (b) paper, (c) felt, (d) coated; complex porous medium.....	2
Figure 1.3: Carbon fibers roll.....	3
Figure 1.4: Direct molding of fibrous porous media .....	3
Figure 1.5: Schematic of hydroentangling of fibrous felt media .....	5
Figure 1.6: (a) An example of a flexible electronics, coated Graphene textile for super capacitors, (b) A sample of electroactive textile, polyester woven fabric coated with conductive polyaniline polymers .....	6
Figure 1.7: Schematic of a polymer electrolyte fuel cell (PEMFC) .....	8
Figure 1.8: The catalyzed GDL coated with ionomer Nafion polymer .....	10
Figure 2.1: The schematic of X-ray tomography.....	20
Figure 2.2: Schematic of FIB-SEM tomography.....	21
Figure 2.3: A porous medium with predominant axes (a) SEM image of Polyacrylonitrile nano fiber used in Lithium rechargeable battery, (b) schematic of nano fibers with central axes found from the normal of the cross sections.....	22
Figure 2.4: A porous structure with complex topology .....	23
Figure 2.5: (a)The textile used in mattress, (b) Carbon nano tube arrays.....	25
Figure 2.6: Geometrical representation of woven carbon cloth in RVE.....	25
Figure 2.7: (a) Aligned, (b) layered with the fibers with in-plane angle of $\pi/4$ , (c) random structures.....	26
Figure 2.8: Schematic of a surface constructed by NURBS.....	27
Figure 2.9: An implicit surface model with two control points.....	28
Figure 2.10: The water distribution in GDL .....	29
Figure 2.11: The $\mu$ CT image of GDL, (a) woven, (b) felt, (c) paper.....	30

Figure 2.12: SEM image of composite paper GDL .....	33
Figure 2.13: Schematic of morphological description of the pore space.....	34
Figure 2.14 Pore size distribution for woven GDL, (b) Woven GDL .....	36
Figure 2.15: Schematic of a surface constructed by NURBS.....	36
Figure 2.16: . Schematic of pore size determining procedure. ....	39
Figure 2.17: Schematic of chord length inside a porous medium.....	40
Figure 2.18: (a) Voxel representation of fibrous porous media, (b) The shortest paths distribution in the porous domain .....	41
Figure 2.19: Schematic of a porous PN model .....	43
Figure 2.20: The schematic of slot die, doctor blade and dip coating processes.....	47
Figure 2.21: Schematic of slot die coating process and the pressure distribution on the web.....	48
Figure 4.1: Periodic surface models of cubic phase and mesophase structures.....	56
Figure 4.2: Cylinder approximated by the rod surface .....	58
Figure 4.3: Two compressed rod surfaces .....	60
Figure 4.4: A bent rod surface model with a sinusoidal shape .....	65
Figure 4.5: Illustration of the cross section change due to the shift (a) geometry and cross section before shift (b) geometry and cross section after shift .....	66
Figure 4.6: Illustration of a bent compressed fiber PS model (a) contact points (b) the cross section change.....	69
Figure 5.1: Schematic representation of a fiber in the RVE.....	71
Figure 5.2: SEM images of a GDL used to extract the distribution of the side and in-plane angles, (a) top view (b) cross sectional view .....	72
Figure 5.3: Schematic of RVE with two fibers, illustrating the implicit surface boundaries .....	73
Figure 5.4: Orientation of 20 fibers in RVE (a): With GA, (b): Without GA .....	75

Figure 5.5: Block diagram of generating the fibers skeleton.....	77
Figure 5.6: Fibers bundle top view from (a): SEM image, (b) PS model, cross sectional view from (c) SEM image, (d) PS model .....	78
Figure 5.7: Decrease in fiber intersections due to the genetic algorithm optimization ....	78
Figure 5.8: The SEM images of carbon felt GDL .....	80
Figure 5.9: Bent fiber in a RVE, (a) one cosine term, (b) superposition of two cosine terms.....	81
Figure 5.10: The geometrical PS model procedure .....	82
Figure 5.11: Freudenberg H2315 carbon felt GDL (a) and (b) top views (c) and (d) cross sectional views, from PS model and SEM images .....	83
Figure 5.12: (a) Original beam, (b) deformation of Euler-Bernoulli beam .....	85
Figure 5.13: Freudenberg H2315 carbon felt GDL reconstructed by energy coupled PS model (a) isometric view, (b) and (c) the zoom in view, (d) SEM image .....	87
Figure 5.14: The change in the intersection volume of felt GDL due to energy coupled modeling approach.....	88
Figure 5.15: The stored strain energy of the felt microstructures with porosity of 0.72 generated by to the energy coupled modeling approach.....	89
Figure 5.16: (a) An isometric view from modified generalized PS model of woven fibers (b) top view from SEM image .....	92
Figure 5.17: Block diagram for generating the composite fibrous porous structure .....	94
Figure 5.18: Fibrous matrix, (b) Minkowski summation with structure element, (c) Minkowski erosion with the same structure element.....	94
Figure 5.19: (a) Isometric view of virtually constructed Toray 060 GDL, (b) and (c) cross sectional views, virtual GDL (left side) and SEM images (right side). .....	95
Figure 6.1: Schematic of PS model and divided RVE.....	98
Figure 6.2: Schematic of a porous medium and its binary representation.....	98
Figure 6.3: Block diagram of generating the binary matrix.....	99

Figure 6.4: The schematic of pore size fitting procedure, deleting the smaller pore located inside the bigger pore.....	101
Figure 6.5: The schematic of pore size fitting procedure, deleting the dead end pore ...	101
Figure 6.6: (a) Hypothetical structure, (b) the graph representation of the porous domain to find the shortest paths from the bottom surface to the top surface .....	104
Figure 6.7: A 2D schematic of Skeletonization of porous media, (a) top view of a porous medium, (b) skeletonized pore space.....	105
Figure 7.1: Numerical pore size distribution of virtual Toray 060 GDL.....	107
Figure 7.2: MIP pore size distribution of Toray 060 GDL.....	107
Figure 7.3: Through-plane chord length distribution for virtual Toray 060 GDL.....	108
Figure 7.4: In-plane chord lengths distribution for virtual Toray 060 GDL.....	108
Figure 7.5: Distribution of the shortest path inside the pore space of Toray 060 GDL..	109
Figure 7.6: Pore size cumulative probability distribution for Toray 060 GDL modeled with different structure elements .....	110
Figure 7.7: Pore size distribution for Toray 060 GDL modeled with different structure elements .....	110
Figure 7.8: The shortest paths distribution for Toray 060 GDL modeled with different structure elements .....	112
Figure 7.9: The through-plane shortest paths distribution for Toray GDL.....	112
Figure 7.10: Effect of volume fraction of binder in GDL's structure on the pore size cumulative probability distribution.....	114
Figure 7.11: Effect of volume fraction of binder in the GDL's structure on the average chord length .....	114
Figure 7.12: Effect of volume fraction of binder on the through-plane cumulative probability distribution of the shortest paths .....	115
Figure 7.13: Effect of volume fraction of binder on the in-plane cumulative probability distribution of the shortest paths.....	115
Figure 7.14: Distribution of the shortest paths of virtually constructed Freudenberg H2315 felt GDL .....	117

Figure 7.15: The through-plane shortest paths distribution of felt GDL .....	118
Figure 7.16: Pore size distribution of virtually constructed Freudenberg H2315 felt GDL .....	118
Figure 7.17: Effect of a GDL structure on the pore size cumulative probability distribution .....	119
Figure 7.18: Effect of porosity of felt GDL on the average chord lengths.....	120
Figure 7.19: Effect of porosity of felt GDL on the through-plane cumulative probability distribution of the shortest paths .....	121
Figure 7.20: Effect of porosity of felt GDL on the in-plane cumulative probability distribution of the shortest paths .....	121
Figure 8.1: 3D reconstructed of the GDL and 2D views from z, x and y directions.....	126
Figure 8.2: Illustration of the tetrahedral mesh for straight fibers bundle in paper GDL. .....	127
Figure 8.3 Felt structure with one cosine term (a) geometric model, (b) unstructured volumetric mesh.....	127
Figure 8.4: The object file of triangular surface mesh of the RVE.....	128
Figure 8.5: Volumetric mesh generated for a paper GDL from the surface mesh .....	129
Figure 8.6: Schematic illustrating generation of volumetric mesh for nonwoven structure .....	131
Figure 8.7: Schematic of generation of volumetric mesh for woven structure.....	131
Figure 8.8: Computational domain and boundary conditions to calculate $K_{zz}$ . .....	134
Figure 8.9: Effect of the mesh size on the pressure drop, $V= 0.01$ m/s, $\varepsilon = 0.8$ .....	136
Figure 8.10: Pressure gradient inside the GDL as a function of inlet velocity and porosity .....	136
Figure 8.11: The schematic of a microstructure and the corresponding diffusion modes .....	143
Figure 8.12: The schematic of the computational domain and boundary conditions .....	144

Figure 9.1: The flow field inside Toray 060 GDL, contour of fluid path lengths .....	147
Figure 9.2: The flow field inside the woven carbon cloth, contour of velocity .....	149
Figure 9.3: Effect of volume fraction of binder in the GDL's structure on the permeability and relative diffusivity .....	154
Figure 9.4: Effect of volume fraction of binder in the GDL's structure on the tortuosity .....	154
Figure 9.5: Effect of volume fraction of binder in the GDL's structure on the effective tortuosity .....	155
Figure 9.6: Effect of porosity of felt GDLs on the permeability and diffusivity .....	156
Figure 9.7: Effect of porosity of felt GDLs on the effective tortuosity .....	157
Figure 10.1: Schematic of slot die coating process, the penetration depth and the pressure distribution on the web.....	160
Figure 10.2: The schematic of computational domain including the porous web .....	162
Figure 10.3: The schematic of computational domain including the porous web .....	163
Figure 10.4: The schematic of the experimental setup .....	167
Figure 10.5: (a) The cross section of the virtually generated microstructure (b) 2D view .....	169
Figure 11.1: The pressure distribution over the web, ignoring porosity of web and capillary forces, including porosity of the web, and considering porosity of the web and capillary forces .....	173
Figure 11.2: The transient pressure inlet boundary condition for the micro scale domain. ....	174
Figure 11.3: Penetration depth versus coating gap ( $H$ ).....	176
Figure 11.4: The transient pressure profile versus coating gap ( $H$ ).....	177
Figure 11.5: Transient Penetration depth profile versus coating gap ( $H$ ).....	178
Figure 11.6 Penetration depth versus coating gap ( $H$ ).....	179
Figure 11.7: Penetration depth versus Flow rate ( $Q$ ).....	180



Figure 11.8: Penetration depth versus coating speed ( $u_w$ ) .....	182
Figure 11.9: Transient pressure inlet boundary condition versus viscosity ( $\mu$ ), for a macro scale simulation.....	183
Figure 11.10: Time dependent behavior of penetration depth versus viscosity of coating solution ( $\mu$ ).....	184
Figure 11.11: Penetration depth versus viscosity of the coating solution ( $\mu$ ), found from analytical model .....	185
Figure 11.12: Penetration depth versus viscosity of coating solution ( $\sigma$ ).....	186
Figure 12.1: The framework for design of fibrous porous media.....	189
Figure 12.2: The framework for characterization of virtual and actual fibrous porous media.....	190
Figure 12.3 The PS model used for construction of (a) paper, (b) felt, (c) and (d) woven fibrous porous media.....	192
Figure 12.4: The PS model of (a) woven, (b) felt, (c) paper GDLs as samples of fibrous porous media.....	193
Figure 12.5: The SEM image of carbon paper with the impregnated binder .....	193
Figure 12.6: Numerical and experimental pore size distributions .....	196
Figure 13.1: (a) SEM image of micro porous layer, (b) G type periodic surface model	200
Figure 13.2: (a) Intersecting fibers, (b) the contacting bent fibers with compressed cross sections.....	202
Figure 13.3: Compression data for Toray 060 carbon paper and woven carbon cloth...	203

## NOMENCLATURE

$C$	Concentration
$C_\epsilon$	Material constitutive matrix
$D$	Diameter
$D_{bulk}$	Diffusivity
$D_{rel}$	Relative diffusivity
$D_0$	Binary diffusion coefficient
$E$	Modulus of elasticity
$fr$	Frequency of the minor phase
$fr_{lmst}$	Minor scale
$\mathbf{F}_{st}$	Surface tension force
$\mathbf{g}$	Gravity vector
$h$	Penetration depth
$H$	Coating gap
$I$	Second moment of area
$\mathbf{I}$	Identity vector
$j$	Diffusive flux
$k_B$	Boltzmann constant
$K$	Permeability
$Kn$	Knudson number
$l_x$	Translation along x axis
$l_y$	Translation along y axis

$l_z$	Translation along z axis
$l(r)$	Path length
$L$	Scale of implicit surface
$L_c$	Brinkman screening length criteria
$L_{ch}$	Chord length
$L_t$	Thickness
$m$	Number of terms of the minor phase
$m_g$	Molecular mass of gas
$n$	Number of fiber
$\mathbf{n}$	Normal vector
$N$	Number of particles
$P$	Pressure
$P_c$	Capillary pressure
$\mathbf{P}_m$	Basis vector
$\mathbf{q}_m$	Minor basis vector
$Q$	Flow rate
$\mathbf{r}$	Location vector
$\mathbf{R}$	Rotation matrix
$S$	The arc length
$t$	Time
$T$	Temperature
$\mathbf{T}$	Translation matrix
$u$	Amplitude of minor phase

$\mathbf{u}$	Velocity vector
$u_w$	Coating speed
$u_{lmst}$	Minor moment
$U$	Stored strain energy
$v_j$	Penetration speed at $j^{\text{th}}$ control point
$V$	Superficial velocity
$w$	Homogenous coordinate
$w_c$	Displacement of centroid
$W$	Slot gap
$\alpha$	VOF variable
$\Upsilon$	Initialization value for level set
$\delta$	Dirac delta function
$\varepsilon$	Porosity
$\epsilon$	Matrix of strain
$\theta$	Angle around x
$\kappa$	Curvature
$\kappa_l$	Scale parameter
$\lambda$	Mean free path
$\mu$	Viscosity
$\mu_l$	Periodic moment
$v$	Thermal velocity
$\rho$	Density
$\sigma$	Surface tension

$\tau$	Stress
$\tau_f$	Tortuosity factor
$\tau_p$	Tortuosity
$\varphi$	Angle around y
$\varphi_l$	Level set function
$\psi$	Implicit surface
$\psi_0$	Isovalue
$\omega$	Angle around z
$\Omega$	Intersection portion

## SUMMARY

Fibrous porous media are widely used in various industries such as biomedical engineering, textiles, paper, and alternative energy. Often these porous materials are formed into composite materials, using subsequent manufacturing steps, to improve their properties. There is a strong correlation between system performance and the transport and mechanical properties of the porous media, in raw or composite form. However, these properties depend on the final pore structure of the material. Thus, the ability to manufacture fibrous porous media, in raw or composite forms, with an engineered structure with predictable properties is highly desirable for the optimization of the overall performance of a relevant system. To date, the characterization of the porous media has been primarily based on reverse design methods i.e., extracting the data from existing materials with image processing techniques. The objective of this research is to develop a methodology to enable the virtual generation of complex composite porous media with tailored properties, from the implementation of a fibrous medium in the design space to the simulated coating of this media representative of the manufacturing space. To meet this objective a modified periodic surface model is proposed, which is utilized to parametrically generate a fibrous domain. The suggested modeling approach allows for a high-degree of control over the fiber profile, matrix properties, and fiber-binder composition. Using the domain generated with the suggested geometrical modeling approach, numerical simulations are executed to simulate transport properties such as permeability, diffusivity and tortuosity, as well as, to directly coat the microstructure, thereby forming a complex composite material. To understand the interplay between the

fiber matrix and the transport properties, the morphology of the virtual microstructure is characterized based on the pore size, chord length and shortest path length distributions inside the porous domain. In order to ensure the desired properties of the microstructure, the fluid penetration, at the micro scale, is analyzed during the direct coating process. This work presents a framework for feasible and effective generation of complex porous media in the virtual space, which can be directly manufactured.

# INTRODUCTION

Fibrous porous media have been used for a few decades in industries such as bioengineering, electronics, energy and environmental processes, filtration, textile, paper and composites manufacturing [1-8]. Fibrous porous media can be either woven or non-woven in raw or composite forms as shown in Figure 1.1. The rapid surge in the use of porous media in nontraditional applications is due to their superior properties such as their high porosity, strength-to-weight ratio, surface-area-to-volume ratio, and mechanical flexibility.

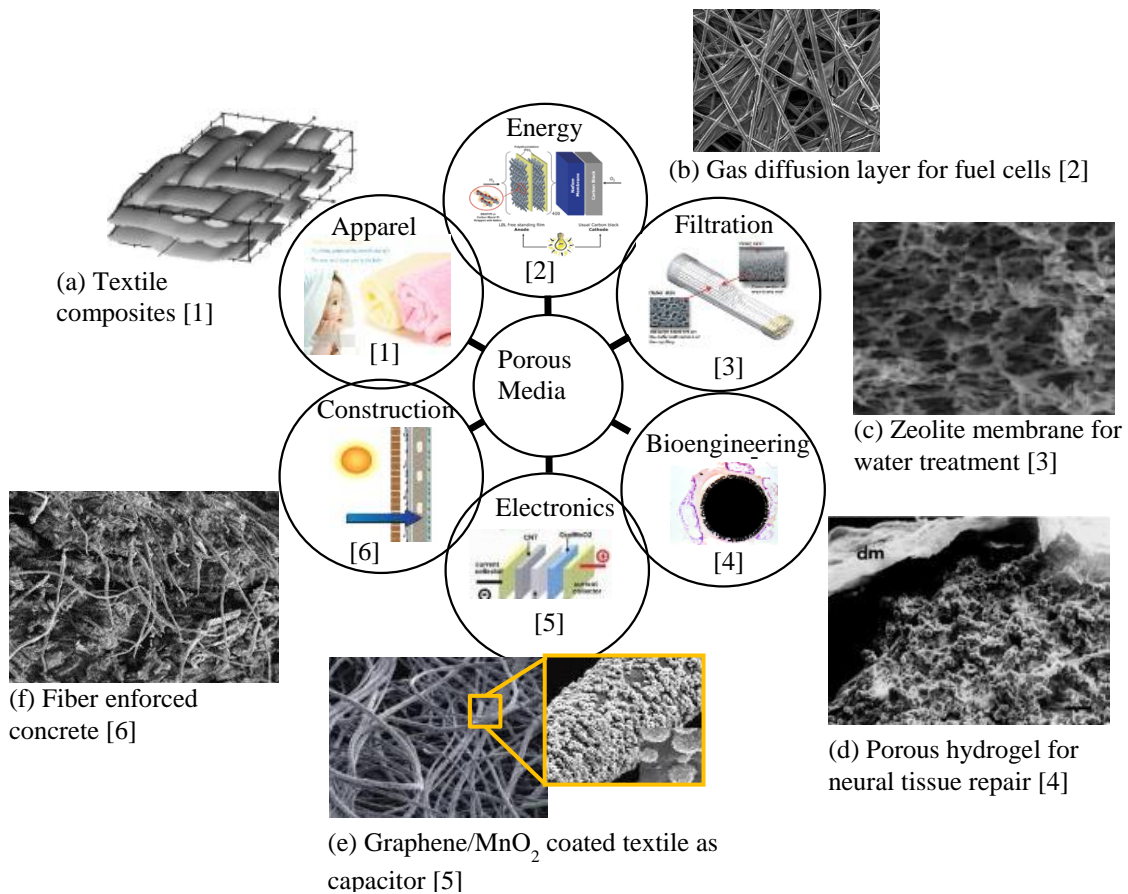


**Figure 1.1** The various applications of porous media.



## 1.1 Fibrous Porous Media and Their Structures

Individual fibers such as carbon, polymer polyester, polypropylene, acrylics, rayon, nylon, cotton, and glass are usually spun from a solution or a melt into a diameter usually less than 10  $\mu\text{m}$  [9]. These fibers are then formed into structural fibrous media as individual fibers or packed fibers called tows. Most common types of fibrous porous media, as shown in Figure 1.2, are woven, paper, felt and complex composite structures.

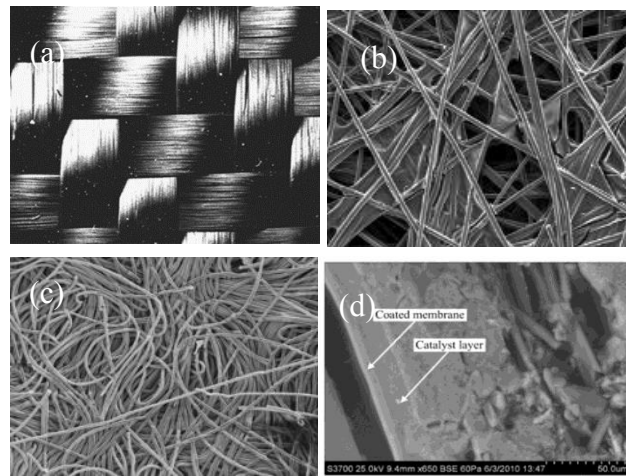


**Figure 1.2** Common types of fibrous porous media, SEM image of (a) woven, (b) paper, (c) felt, (d) coated; complex porous medium.

Woven fibrous porous media shown in Figure 1.2 (a), are manufactured by weaving or stitching bundles of fibers (shown in Figure 1.3). Fiber tows can be formed into 3-dimensional shapes using braiding and weaving techniques to provide structural support in various directions, depending upon the application. These tows are generally elliptical or circular in cross section, and may contain 100 to 50000 single fibers [10].

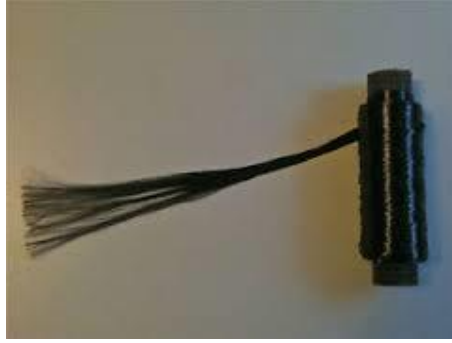


**Figure 1.3** Carbon fibers roll.

Nonwoven structures are either paper or felt as shown in Figures 1.2(b) and (c). Papers are composite structure, with long or short fibers that are bound together in a matrix of binder polymer. The paper porous media are commonly manufactured by two methods. The first manufacturing method is direct melting as shown schematically in Figure 1.4. In direct melting the polymer chip is loaded into the process equipment to extrude fibers and form the porous web simultaneously. This approach is usually the least expensive method because all the manufacturing tasks, from forming the webs to rolling the paper can be accomplished in a single-step.

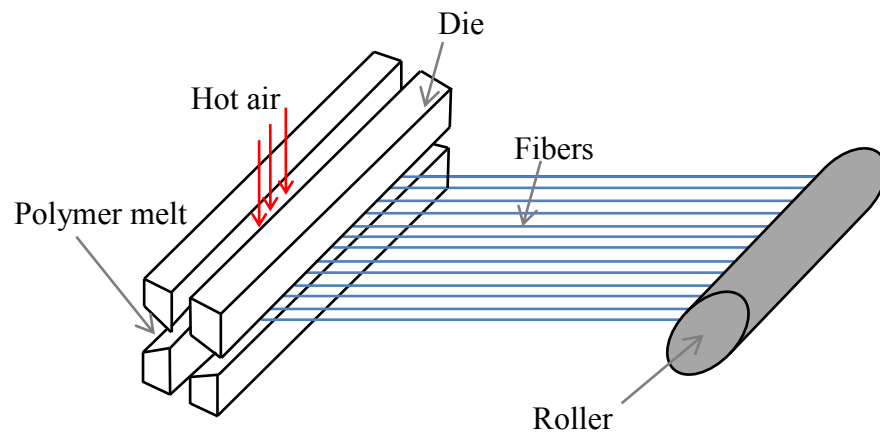


**Figure 1.4** Direct molding of fibrous porous media.

For enhanced applications the paper structures with special characteristics are required that cannot be made in a single step, and have to be manufactured with special manufacturing methods designed for the specific applications. In this category, fibers are bonded together in a matrix of resin to form a fibrous web that is strong against the shear forces and delamination resistance. The resins (also called as binder) that are either thermoset or thermoplastic should properly wet the fibers surface to form a good bond between the fibers and the matrix. The type of resin plays an important role in determining the manufacturing process. Thermoset materials are only 50 to 500 times more viscous than water and can impregnate the empty spaces between the fibers readily. They require an additional processing step that involves chemical reaction known as curing to cross-link the polymer chains. On the other hand, thermoplastic materials do not require this step but are highly viscous. Their viscosity can be as high as a million times more than water. Hence, it is difficult to make them flow and fill the small void spaces between the fibers [11].

The felt structures, as shown in Figure 1.2(c), are manufactured by carding of the fibers and forming a thin fiber fleece mat bound by hydroentangling. As shown schematically in Figure 1.5, in hydroentangling a curtain of very fine 80 – 150  $\mu\text{m}$  diameter water jets with spacing of 15 – 50 jets per cm is impinged onto a moving mat. This causes some fibers to orient in the through-plane direction and creates a mechanically bonded non-woven fabric [8, 12].

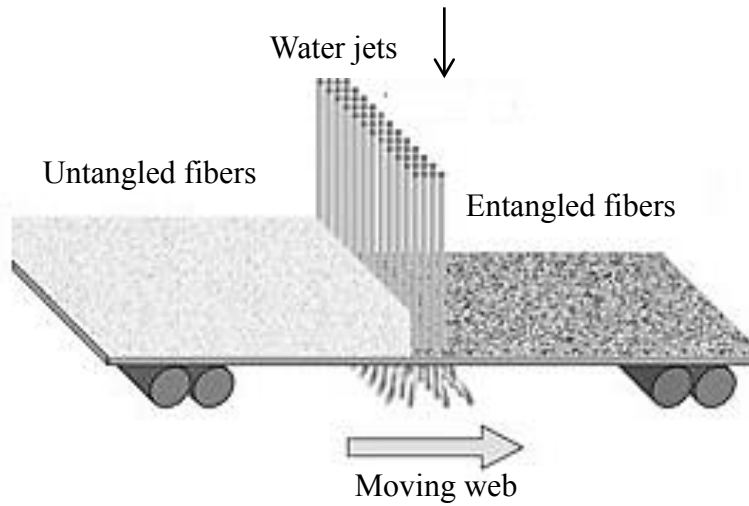


**Figure 1.5** Schematic of hydroentangling of fibrous felt media.

Complex composite structures, as shown in Figure 1.2(d), are fabricated by coating an additional layer on the top of a porous media. The addition of the layer to the surface of the woven or nonwoven porous media can be accomplished by decal transfer, hot pressing or direct coating procedures [13, 14]. Complex porous media are widely used by many industries such as paper, textile, energy and flexible electronics. In paper industry, various types of functional papers, such as papers with resistance to grease, moisture or ultraviolet radiation have been produced. In textile industry water proofed fabrics are manufactured by coating a thin film of PTFE or Polyurethane (PU) polymers [15]. The newly emerged technologies such as smart textile and wearable fabrics are utilizing various coating approaches to fabricate multifunctional devices as shown in Figure 1.6. However, the effects of manufacturing condition on the final properties of these materials are not fully investigated [16].

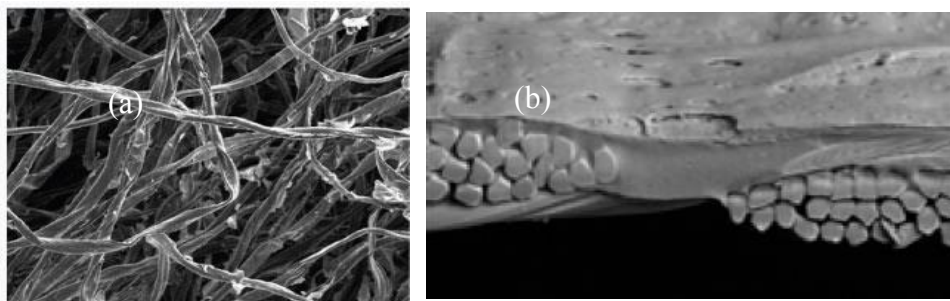


**Figure 1.6** (a) An example of a flexible electronics, coated Graphene textile for super capacitors [17]. (b) A sample of electroactive textile, polyester woven fabric coated with conductive polyaniline polymers [18].

## 1.2 Application of Porous Media in the Energy Sector

Due to the significant increase in the consumption of fossil fuels e.g., petroleum and natural gas and the exponential increase of the resultant emissions, new energy resources are needed. The alternative energy resources should be abundant to response to the surging demand of energy and to decrease emissions. According to the Department of Energy (DOE) the majority of the energy consumption is in transportation section [19]. The fuel consumption for the transportation needs will be approximately 16.38 million barrels per day by 2035 that accounts for 74% of the whole liquid fuel consumption [19]. Considering the limited oil and gas supply of the world and their growing global demand, a significant increase in the cost is eminent. Although emission restrictions have increased, the total carbon dioxide CO<sub>2</sub> emissions in 2035 is expected to increase 9% compared to 2008 [19]. Greenhouse gas emissions like CO<sub>2</sub> are believed to be the main contributor to the global warming [20]. Thus, renewable and green energy sources such as wind, solar and hydrogen are being integrated into viable devices to supply alternative

energy sources.

Among the alternative energy devices, polymer electrolyte membrane fuel cells (PEMFCs) are promising alternative to the conventional gas engines, due to their high power densities. Other than their high power densities, PEMFCs use hydrogen and oxygen as reactants and their only byproduct is water. Thus, the opportunity to have emission-free operation and fuel independency can theoretically be realized. In this work, PEMFCs are considered not only because of its promise as an alternative energy resource, but because each type of fibrous porous media previously discussed can be used in the cell.

### ***1.2.1 Working Principle of Polymer Electrolyte Membrane Fuel Cells***

A PEMFC is an electrochemical device that continuously converts chemical energy into electrical energy. As shown schematically in Figure 1.7, hydrogen gas used as fuel is injected to the bipolar plate located at the anode side and oxygen or air is injected to the bipolar plate located at the cathode side of the fuel cell. To uniformly distribute the reactants i.e., oxygen and hydrogen, they are forced to pass through gas diffusion layers (GDLs). In most of the fuel cells GDLs are loaded with platinum (Pt) nanoparticles as the catalyst, to form gas diffusion electrodes (GDE). A polymer electrolyte membrane (PEM) conducts protons and separates hydrogen and oxygen. Conventional PEMs are thin ionomer films with thickness of 20 to 100  $\mu\text{m}$ . For electrochemical reactions to take place a triple-phase boundary is required, which is the area where the GDE, PEM and fuel interface, identified as membrane electrode assembly

(MEA). In MEA hydrogen splits into protons and electrons as shown by Equation 1.1. The PEM conducts the generated protons and electrons are collected through an external circuit. Therefore, electricity is produced. At the cathode, oxygen combines with electrons and protons form water as described by Equation 1.2. The only byproduct of the ongoing electrochemical reactions in the PEMFC is water and the losses manifest as heat. The complete reaction is given by Equation 1.3.

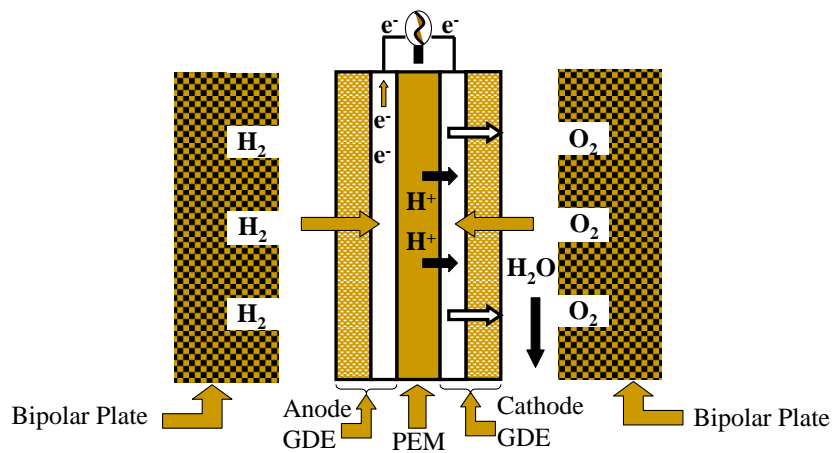


**Figure 1.7** Schematic of a polymer electrolyte fuel cell (PEMFC).



### 1.2.2 Porous Media Used in PEMFCs

GDLs that are carbon based fibrous porous media have several functions in the PEMFCs. They transport the reactant gasses from the bipolar plates' channels to the

catalyst layers and distribute the reactants uniformly. They help removal of water byproduct from the catalyst layer surface. GDLs provide the electronic conductivity from bipolar plates to the catalyst layers. GDLs are mechanical support for the PEM to maintain good contact with the catalyst layer, and not to compress into channels resulting in blocked flow [21]. Common types of GDL include woven, paper and felt structures, as shown in Figure 1.2 (a), (b) and (c).

It has been found that the morphological and transport properties of the GDL have large impact on the performance of the fuel cells. For example, it is shown that there is a correlation between the GDL's microstructure and the limiting current density of PEMFC. Because, smaller pores in the GDLs are not affected by capillary condensation, GDLs with smaller pores can transport oxygen more efficiently [4]. The multiphase nature of PEMFCs and the large impact of the GDLs properties on the fuel cell performance warrant the need for a profound study for the design and optimization of GDLs' transport and structural properties.

Recently to answer the demand for scalable manufacturing method in the renewable energy sector, Ding et al. developed a new fabrication process to manufacture a functional membrane that works as the MEA in PEMFCs. This functional membrane, shown in Figure 1.8, was fabricated by the slot die coating of the ionomer onto a catalyzed GDL [13]. The uniformity of the coated membrane and the penetration of the ionomer into the catalyst layer were found to be two important factors on the functionality of the newly fabricated MEA.



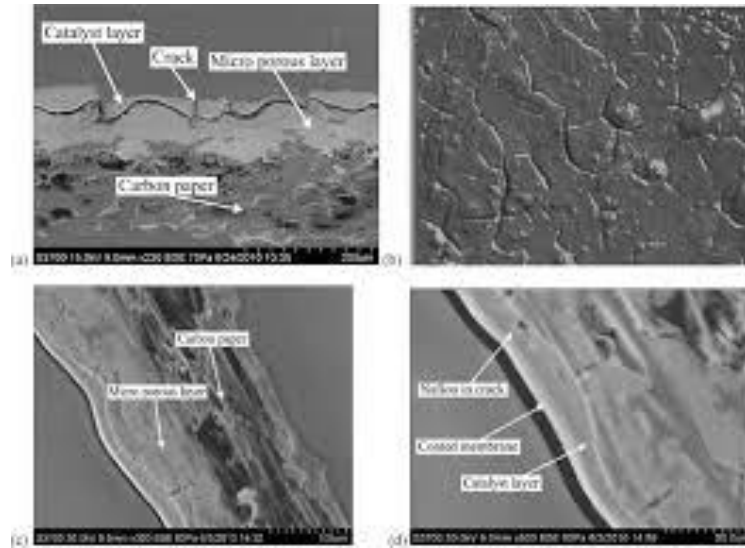


**Figure 1.8** The catalyzed GDL coated with ionomer Nafion polymer.

### 1.3 Research Motivations

The performance of systems incorporating porous media heavily depends upon the mechanical and transport properties of the porous media [22-25]. However, the mechanical and transport properties of a porous medium depend on its pore structure. Thus, the ability to manufacture fibrous porous media with an engineered structure and predictable properties is highly desirable for the optimization of the overall performance of the relevant systems.

The manufacture of engineered porous materials warrants the use of a rational and parametric design approach not only for the system enhancement but also to reduce the manufacturing cost and time to the market. However, current research and development efforts rely on trial and error approaches to engineer porous materials [26]. In addition,

the resulting porous media is currently characterized based on reverse design methods i.e., extracting the data based on the existing material with image processing techniques. The reverse engineering techniques are not only expensive but also might be destructive [4].

In addition to using porous media in raw or composite form, some applications require the porous media to be coated with an additional layer. The porous medium with a coated layer is tailored for the desired functionality and has a complex composite structure. However, adding material to the surface of the porous medium will change its properties; this is neither well understood nor controlled [13, 14].

To date, design of porous media is based on experimental and trial and error approaches. Experimental quantification of the key properties of porous material is expensive, difficult to conduct, and not appropriate for design purposes.[27-29]. Most standard experimental methods are limited to providing bulk property data, which only indicate the general characteristics of the material. Moreover, the nature of experimental methods prevents them from being used as design tools.

The motivation of this research is to develop a methodology that enables a systematic and parametric design for composite porous media, which is currently fleeting in the field. Implementing a rational design process that is integrated with modern computational tools instead of reverse engineering or trial and error approaches, the functionality of the porous medium can be enhanced. Using a computer aided design methodology the key controllable properties of the porous material can be determined and efficiently calculated before the manufacturing stage. Hence, a framework to reduce

manufacturing time and cost can be provided.

#### **1.4 Research Objectives**

The objective of this research is to develop a methodology for design of composite porous media with tailored properties, which will enable their direct manufacture with a high degree of certainty.

In the design process, it is imperative to determine the characteristics of a porous material utilizing numerical approaches. The micro scale features of a porous structure i.e., its morphological properties, and its transport and mechanical properties, are related to each other. Thus, to predict the transport and mechanical properties of a porous medium, a detailed description and characterization of its internal structure is required. To determine the morphological properties of a porous material, its microstructure has to be generated either by imaging techniques or by the geometrical modeling techniques. However, the imaging technique is not suitable for design purposes because it depends on the final products. The current geometrical modeling approaches are not able to generate the complex internal structure of the porous media. For this purpose finely detailed micro scale geometry of the porous media has to be generated, and optimal numerical characterization approaches have to be developed.

To manufacture a porous medium with tailored properties it is essential to investigate the effects of the manufacturing conditions on the final properties of the composite structure. For this purpose, the relationship between the processing parameters, the microstructural properties and the final properties of the complex composite media

are investigated in this research. In this study the virtual modeling of the slot die coating process of a porous medium is selected as a representative of manufacturing space.

### **1.5 Key Questions and Research Tasks**

To meet the objectives of this work, the following questions have to be addressed:

- (1) Can a generalized modeling technique be used to parametrically generate the internal structure of a porous media? Is the model capable of representing different fibrous porous structures (raw or composite structures) accurately and efficiently?
- (2) What are the key controllable properties of the porous material? Is there an efficient numerical approach to predict these properties such that the characterization of generated structures can be used to enhance the design and optimization before manufacture?
- (3) What are the effects of the manufacturing process on the final properties of the composite structures? Can the manufacturing process be controlled such that the properties of the porous structure created virtually are maintained?

Exploring these questions will lead to a fundamental understanding of the transport phenomena in the fibrous porous media, the effects of the geometrical characteristics and manufacturing on the transport and morphological properties of the porous material. To answer these questions and also to meet the research objectives the following five tasks must be completed:

*Task 1: Developing a virtual representation of the fibrous porous structures*

*Task 2: Determining the morphological properties of the porous structures*

*Task 3: Determining the transport properties of the porous structures*

*Task 4: Investigating the feasibility and accuracy of the suggested modeling and characterization approach, and*

*Task 5: Simulating the porous coating or resin intrusion process.*

## **1.6 Thesis Layout**

This thesis presents a framework for feasible and effective generation of complex porous media in the virtual space, which can enable direct manufacture of these materials. In Chapter 2, relevant literature on geometrical modeling of porous structures, morphological and transport property characterization techniques, coating processes (primarily emphasizing on slot die coating) and fluid penetration into a porous structure are presented.

In Chapter 3, the materials used in this thesis for the case studies to demonstrate the feasibility of the suggested methodology are introduced.

In Chapter 4, the periodic surface modeling technique used to model various types of porous structures is introduced. The periodic surface modeling approach for the fibrous porous structures is described in detail.

In Chapter 5, implementing the procedure described in Chapter 4, the generated microstructure of the carbon paper, carbon felt and woven GDLs as a representative of different types of fibrous porous media are presented.

In Chapter 6, the morphological properties of porous media and the proposed methods for calculating these properties are introduced. Also the method to couple the characterization procedure and geometrical modeling of the porous structure is described.

Chapter 7, the morphological properties of the virtually reconstructed carbon paper, carbon felt gas diffusion layers, serving as the case studies in this thesis, are determined and verified against experimentally measured data by implementing the procedure described in Chapter 6.

In Chapter 8, the mesh generation procedure, the implemented numerical methodology and the relevant boundary conditions for computing the transport properties of the virtually generated microstructures of the porous media are discussed. The transport properties of interest are permeability, tortuosity, diffusivity and tortuosity factor.

Chapter 9 presents the numerically obtained transport properties of the virtually reconstructed GDLs serving as the case studies in this thesis. These numerically computed properties are compared and verified by experimental measurements.

In Chapter 10, the numerical procedure used to analyze the complex porous media

is introduced. An in-house developed experimental setup, equipped with a slot die coating system used to coat a thin film on top of a porous medium to form layered porous structures, is described. The numerical procedure to simulate the coating process at the macro scale is also presented in this chapter. In chapter 10, the fluid penetration process into a porous medium during the slot die coating process is also discussed. The numerical simulations and the required boundary conditions for the micro scale modeling of the penetration process are also presented.

In chapter 11, the effects of the wetting and rheological properties of the coating solution on the fluid penetration into a porous medium during the slot die coating process are discussed. The effects of the operating conditions e.g., coating speed, on the final penetration depth are also investigated.

In Chapter 12, the important conclusions and findings from the present study in addition to the contributions of the current study are laid out. In Chapter 13, a discussion on how the current study can be further extended in the future is provided.

## **1.7 Summary**

The performance of systems that incorporate porous media depends on the morphological and transport properties of that media, so the ability to tailor properties of porous structures is highly desirable. However, no systematic design approach for their manufacture exists in the field to the best of author's knowledge. In this thesis, a method to virtually generate complex microstructures and determine their properties is presented.

The developed methodology provides connectivity between the design phase and manufacturing phase in a virtual space. Also, in this thesis the required framework to elucidate the relation between the morphological properties of fibrous porous media and their transport properties is presented.

This work is greatly helpful for the field of material engineering, as it gives engineers an effective tool in the virtual space for the optimal design and manufacture of porous media. In the current study, only fibrous porous media are investigated, but the framework and conclusions may be extended to the other types of porous structures.



## **2. BACKGROUND**

The initial step in the design of porous media is to geometrically represent their complex structures. By characterizing the virtually generated structures, before proceeding to the manufacturing stage, it can be determined whether the design criteria are met or not. In this chapter, an overview of the existing modeling approaches used for geometrical representation of the porous media and their limitations are presented. A review of existing literature on the geometrical modeling and characterization of GDLs, which are selected as the microstructures to study in this research, is also presented.

The characteristics of a porous structure that are the interest of this study are morphological and transport properties. In this chapter, these properties are discussed in detail. The existing methods used to determine the morphological and transport properties of the porous media, including GDLs, are also outlined and their advantages and disadvantages are discussed.

To produce functional porous material, it is often required to coat a thin layer over a porous medium. Among the existing coating technologies, the slot die coating method is selected in this study as the method of interest; because it is easily scaled and can coat thin films with higher degree of uniformity compared to the other existing coating methods. In this chapter an overview of the available manufacturing methods for coating a solid and porous medium to form a composite structure is presented. Though, the slot die coating process is discussed in more details.

## 2.1 Virtual Representation of Fibrous Porous Structures

The existing approaches for virtual representation of porous media are two folds; 1) image based reconstruction and 2) geometrical construction. Image processing methods and digital reconstruction techniques have been utilized by many industries such as radiology and biology and also material characterization field. The image based approaches consist of obtaining 2D images of the internal pore structures of the fibrous material at different cross sections, and regenerating the 3D structure from the stack of image slices. Various imaging techniques such as computed microtomography ( $\mu$ CT) and focused ion beam (FIB) tomography are utilized to capture the internal topology of the porous structures [30-39].

Tomography refers to all the imaging techniques that capture the images by using a penetrating wave. In conventional tomography, as shown in Figure 2.1, the material is exposed to an X-ray wave that is moved in the opposite direction of the film. Structures in the focal plane appear sharper, while features in other planes appear blurred. Due to the generated contrast, the internal structure of the porous medium can be revealed. Different types of signal acquisition can be used in tomographic imaging, as given in Table 2.1.

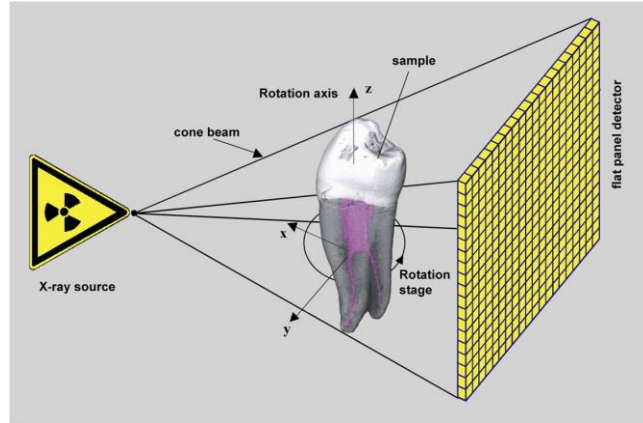


**Figure 2.1** The schematic of X-ray tomography [40].

**Table 2.1** The common types of tomography.

Physical Phenomenon	Tomography Method
X-ray	Computed tomography (CT)
Gamma rays	Single-photon emission computed tomography (SPECT)
Radio-frequency wave	Magnetic resonance imaging (MRI)
Electrons	Transmission electron microscopy (TEM)
Ions	Atom probe

The computer tools are also integrated with the tomography methods leading to development of computed tomographic (CT) scanners such as micro CTs ( $\mu$ CT).  $\mu$ CT uses X-ray to create cross-sectional images of a 3D-object that later can be used to recreate a virtual model without destroying the original sample. In  $\mu$ CT the pixel sizes of the cross-sections are in the micrometer range, which generates high resolution images. Small scales features of the porous medium can be captured with higher accuracy using

these high resolution images.

Other than the nondestructive image based approaches such as  $\mu$ CT destructive methods have also been implemented for reconstruction of the porous structures. One of the destructive approaches developed for porous media with micro and nano scales pore sizes is FIB-SEM tomography which utilizes a FIB combined with an scanning electron microscope (SEM), as shown schematically in Figure 2.2.

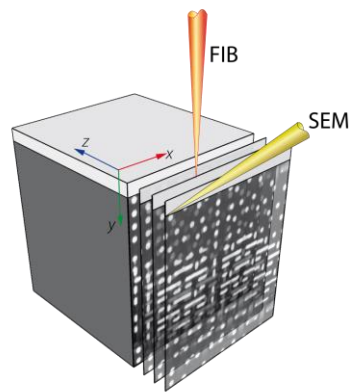


**Figure 2.2** Schematic of FIB-SEM tomography [41].

FIB-SEM tomography makes use of the imaging ability of a SEM to take high resolution images and the ability of FIB to remove certain parts of material from the surface of a sample with nanometer accuracy [25]. To reconstruct the porous medium a SEM sequentially takes cross sectional images of the sample and a FIB is used to remove the current layer to expose the material underlying. Repeating the combined operation of SEM and FIB an image stack is obtained that can be converted to the binary format or voxels.

Different approaches have been implemented to convert the stack of 2D captured images to a 3D representation of porous medium. As shown in Figure 2.3, for the porous structures where the features of the structure have predominant axes, the extracted images can be used to find the predominant axes and reconstruct the geometry from the extracted axes.

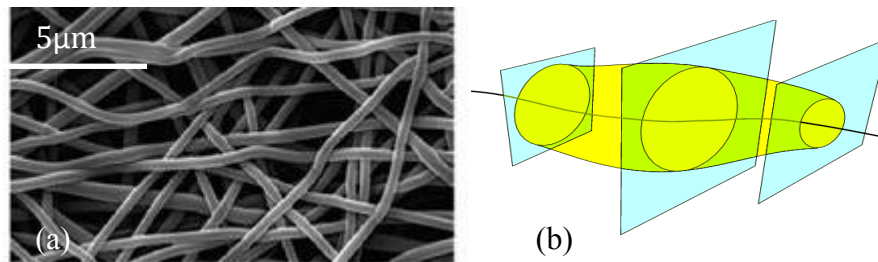


**Figure 2.3** A porous medium with predominant axes (a) SEM image of Polyacrylonitrile nano fiber used in Lithium rechargeable battery [42], (b) schematic of nano fibers with central axes found from the normal of the cross sections.

For complex geometry without predominant axes, as shown in Figure 2.4, different reconstruction algorithms have been developed. The reconstruction is accomplished by aligning, cropping and combining the 2D images and then, segmenting the data with an appropriate segmentation algorithm. The segmentation algorithms fall into one of these two categories; filtered back projection (FBP) or iterative reconstruction (IR). FBP procedures are not computationally demanding. However, they reconstruct the 3D structures with lower accuracy than IR. On the other hand, IR algorithms have fewer errors in the reconstruction with a higher computing time.

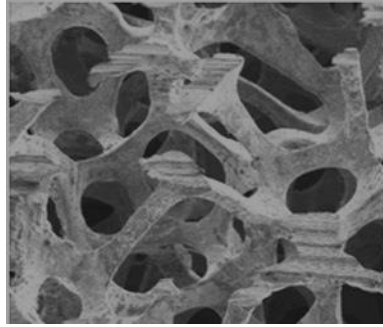


**Figure 2.4** A porous structure with complex topology.

As briefly outlined, the image based methods require advanced equipment and lengthy time to prepare the samples. The imaging techniques might accurately capture the geometry of the porous structures, but the models cannot be modified and depend on the end product. This inflexibility makes such options ill-suited for design. Also, to numerically compute the transport and mechanical properties of the reconstructed 3D structure, its volumetric mesh representation has to be generated. The volumetric mesh can be generated either from a boundary representation (B-Rep) of reconstructed porous structure or from the 3D voxel representation of the reconstructed porous structure. However, generating a volumetric mesh from the 3D virtual imaged based porous structure is not a trivial task.

As mentioned, due to the inflexibility of the image based approaches for designing porous media, various geometrical models have been implemented. Many of the presented models utilize macro scale computer aided design (CAD) tools. At the bulk scale, commonly used geometric modeling methods include boundary representation, Hermite, Bezier, B-spline, T-spline and other polynomial functions for free form surfaces, as well as convolution surface and R-function for implicit surfaces and volumes.

Often to model the complex structure of porous medium with the conventional CAD tools simplifying assumptions have been made, which inhibit the ability to model the fine-detailed internal structures of the porous medium. Simple approximated geometries such as circular arcs connected by straight-line segments, rectangular blocks, B-spline central curves and non-uniform rational B-spline (NURBS) have been used to represent the complex and inhomogeneous shape of the fibrous porous materials [43-47].

Cheah et al. used polyhedral shapes in modeling biological tissues by assuming that the tissue can be approximated as a spatially homogeneous structure [47]. Chow et al. proposed a layer-based approach with 2D Voronoi tessellation to reduce the 3D domain to a 2D one [48]. Kou et al. presented a modeling method for porous structures with graded porosities and pore distributions based on stochastic Voronoi diagram and B-Spline representation [49]. Sudarmadji et al. [50] developed a library consisting of polyhedral units that can be assembled to represent the scaffold structures.

To date, few studies exist regarding the geometrical modeling of fibrous porous structures. Fibrous porous media can be found in woven and nonwoven forms, as shown schematically in Figure 2.5. Modeling the woven fibrous media is more trivial compared with the other types of fibrous porous media, due to the arranged position of the yarns. The woven fibrous media were often constructed by simply combining B-Rep models of individual fibers, as shown in Figure 2.6. Peirce et al. modeled woven fibers with circular arcs connected by straight line segments [51]. Hewitt et al. approximated fibers in woven composite materials by discrete but connected rectangular blocks [52]. Turan et al. used B-spline to represent the central curves of the woven fibers [53]. Smith et al. used

differential equations to construct woven compressible structures without intersection among fibers [54]. Srepreateep et al. used non-uniform rational B-spline (NURBS) to generate the central curves of the fibers in yarns and similarly built the solid model of fibers by sweep operations [55]. Sun et al. used the commercial CAD software Pro/Engineer to build solid models of woven composite materials for stress and deformation analysis [56].

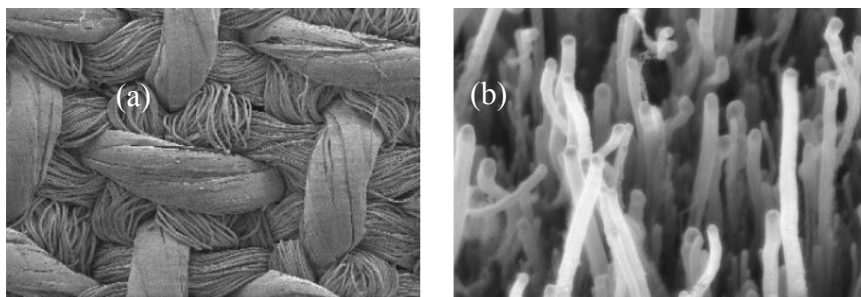


**Figure 2.5** (a) The textile used in mattress, (b) Carbon nano tube arrays [57].

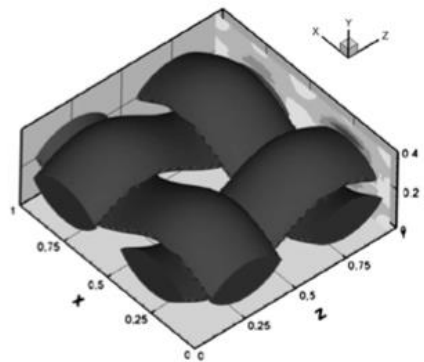


**Figure 2.6** Geometrical representation of woven carbon cloth in RVE [58].

As shown in Figure 2.7, nonwoven fibrous structures have been modeled with different spatial configurations such as, aligned, layered, or random structures. Due to the



undetermined position of the fibers in the nonwoven porous structures, the random models have been usually implemented to determine the spatial orientation of the fibers in the domain [59-62]. For the layered structure fibers are built in a layer-by-layer pattern and randomly oriented within each layer. In the random structure, the fibers are oriented randomly in all three spatial directions.

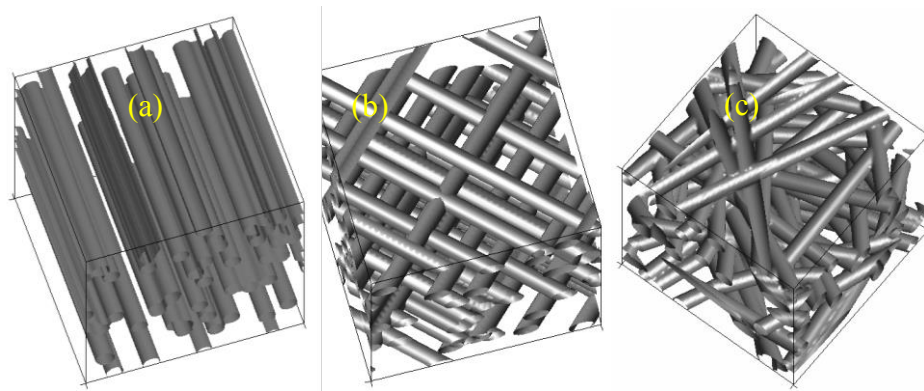


**Figure 2.7** (a) Aligned, (b) layered with the fibers with in-plane angle of  $\pi/4$ , (c) random structures.

These methods can only construct straight fibers with a simple cylindrical shape, which affects the accuracy of numerically determined transport and mechanical properties of the virtual structure. The models have limited flexibility for modifying a fibers' shape profile, such as the fiber curvature. Therefore, the oversimplified straight-fiber model confined in large representative volume elements (RVE) does not serve as an effective design scheme. As shown schematically in Figure 2.8, to model complex surfaces by the conventional CAD tools a lot of control points are required. Because of the difficulty of modeling the bulk properties of a porous medium using a large set of control points, the conventional CAD tools are inefficient for modeling complex porous

structures.

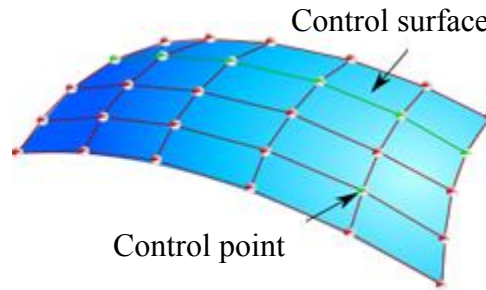


**Figure 2.8** Schematic of a surface constructed by NURBS.

In an alternative modeling approach, implicit surface modeling method has been implemented to virtually construct porous structures. Implicit surfaces are closed form mathematical functions that describe the outer surface of 3D objects. Because of the ease of controlling these functions compared to discrete voxels or control points, this method is more suitable for the material design purposes.

An example of an implicit surface is shown in Figure 2.9. Considering the implicit surface function  $D(r) - \frac{1}{r^2} = 0$ , the implicit surface is the contour of the points in space that have the same distance from a control point. If only one control point is assumed the resulting shape is a sphere and if two control points are considered the resulting surface is similar to an ellipse. As shown in Figure 2.9, different shapes can be generated by adjusting two control points and the distance from the control points.

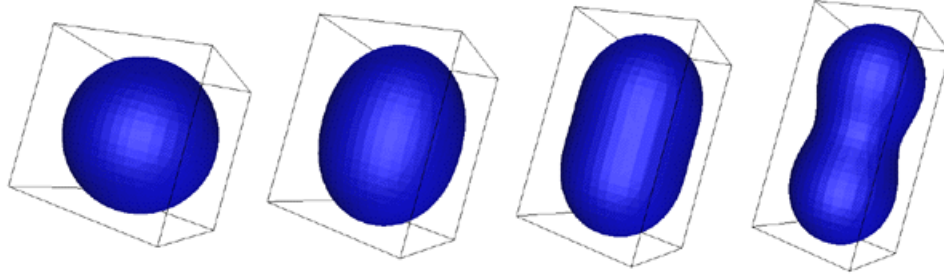


**Figure 2.9** An implicit surface model with two control points [63].

In order to support material design and analysis, it is desirable to develop a multi scale model that can generate micro/nano features of the porous structures while representing the bulk media. For this purpose periodic implicit surface modeling approaches were developed that accommodate the need of model construction at multiple levels from micro to the bulk scales. Recently, Wang proposed periodic implicit surface model (PS) for computer aided nano design that parametrically generates the geometry of nano and microstructures [64] . Due to the embedded periodicity and porosity of the suggested PS modeling technique accurate representation of the natural morphology of polymers and nanostructures was possible.

A parametric modeling technique that is proper for the design of fibrous porous media has not been proposed. Thus, in this study a modified PS model is presented that is proper for generating fibrous porous media with complex internal structures, thereby providing a framework for designing fibrous porous structures.

## **2.2 Reconstruction of GDLs' Microstructure using Imaging Techniques**

A greater understanding of the internal pore structure of GDLs is highly beneficial

for increasing the accuracy of the micro scale and macro scale numerical models developed for fuel cell design. To determine the morphology of the GDL different imaging techniques such as  $\mu$ CT, nano scale computed tomography and confocal microscopy imaging have been implemented [65]. Bazylak et al. used  $\mu$ CT visualizations, with a  $1\mu\text{m}$  resolution to capture the internal structure of Toray 060 GDL with 20 wt. % Polytetrafluoroethylene (PTFE) and reported a heterogeneous porosity for the GDL. As shown in Figure 2.10, they found that the non-uniformity of the GDL's porosity is correlated with water saturation distribution. At the locations where the porosity was locally higher the liquid water was retained.

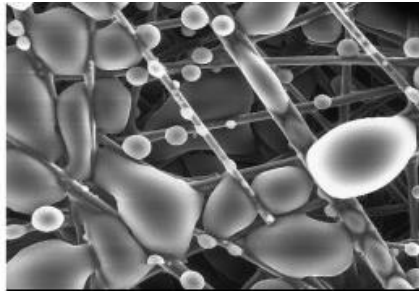


**Figure 2.10** The water distribution in GDL [66].

Fishman et al. used  $\mu$ CT imaging to determine the inhomogeneity of woven and nonwoven GDL structures as shown in Figure 2.11[38]. They found that the porosity of the GDLs at the regions close to their surface is lower than the porosity of the central regions in both woven and nonwoven GDLs. Becker et al. used  $\mu$ CT imaging to investigate the variation of GDL's microstructure under compression [39]. Sinha et al. utilized  $\mu$ CT imaging, with a spatial resolution of  $10\mu\text{m}$ , to find the liquid water saturation along the thickness of a Toray GDL [67]. Ostadi et al. employed nano scale CT imaging ( $680\text{nm}$  resolution) on a GDL and captured the internal structures of GDLs and

provided the average porosity of the GDLs [68]. Berejnov et al. used optical profilometry technique to measure the pore size distributions in the GDL and reported the existence of large pores with the approximate size of  $100\mu\text{m}$  [69]. Gao et al. used confocal microscopy to determine the pore sizes distribution in nonwoven paper GDL [70].

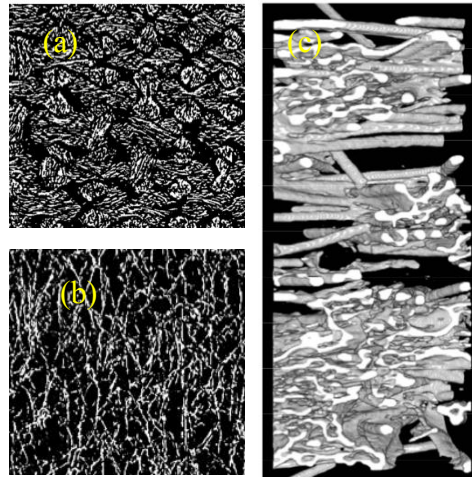


**Figure 2.11** The  $\mu\text{CT}$  image of GDL, (a) woven, (b) felt, (c) paper [38].

Mukherjee et al. used digital volume imaging (DVI) to reconstruct nonwoven GDL microstructures [71]. DVI is a block-face fluorescence imaging technique, which repeatedly sections the porous material and takes images of the appeared cross section. Serial sectioning in DVI is fully automated. In this method the porous sample needs to be embedded in a polymeric resin to allow for sectioning. The DVI technique is a destructive imaging method unlike the non-invasive X-Ray tomography method. But, it generates higher quality 3D virtual geometries that can be directly used for further numerical simulation.

Among all these methods  $\mu\text{CT}$  has been suggested as the suitable imaging

technique for capturing the internal structure of GDLs [65].  $\mu$ CT enables the direct calculation of the GDL morphology and provides great insight into the local GDL microstructure with non-destructive cross-sectional imaging. Compared to higher resolution tomography imaging  $\mu$ CT scanning is financially and computationally less expensive, enabling many more GDL materials to be compared and analyzed [38].

Implementing the imaging techniques, it has been found that GDLs have a heterogeneous structure with large variance in their pore size and porosity. Due to this heterogeneity, the local electrochemical reaction rate changes in the PEMFC and results in non-uniform water distribution through the GDL. Local accumulation of water in the GDLs is not desirable, because the water droplets cannot be removed efficiently, potentially clogging pores and reducing the overall cell performance. However, few PEMFC modeling studies account for the heterogeneity of the GDL which would provide more accurate performance predictions [72]. Based on the experimental observation, it has been found that to accurately predict PEMFC performance it is necessary to conduct the numerical simulations at the pore level. Hence, the constructed pore structure should capture the heterogeneity of the GDL.

### **2.3 Geometrical Modeling of GDLs' Microstructure**

To date, geometrical modeling of GDLs has been primarily accomplished by using statistical methods to locate the fibers that are assumed as long cylinders in a RVE [59]. The fiber skeleton of GDLs was modeled as a collection of intersecting cylinders oriented along randomly distributed axes. The directional distribution of the fibers was

determined by assuming a normal distribution or from SEM images of the GDL. Schulz et al. presented a layered 3D model of a GDL, assuming straight fibers with the cylindrical shape [62]. They assumed infinitely long fibers in the form of cylinders with a known in-plane directional distribution density. The distribution density was assumed to be a polar function of a fiber's angle.

Mukherjee et al. [73] and Inoue et al. [74] also applied a stochastic reconstruction method similar to that by Schulz et al.[62] and suggested new methods for evaluating the permeability of constructed GDL microstructures. Thiedmann et al. [75] constructed GDL microstructures by assuming a layered structure and implementing a Poisson planar line tessellations (PLT) process to represents the axes of the fibers.

Others have modeled GDLs with simplified geometries such as arrays of parallel and perpendicular cylinders or channels to determine their transport properties [76, 77]. For instance, Van Doormaal and Pharoah [78] used an extension of the Monte Carlo method developed by Hamilton [79] and proposed a simplified layered geometry for the GDL. Park et al. regenerated a GDL from scanning electron microscopic (SEM) images of the carbon paper [80].Gaiselmann et al. represented the pore space of fibrous media by random geometric graphs [81]. The parameters required for modeling were specified such that the distributions of vertex degrees and edge lengths coincide with the model based on X-ray synchrotron tomography images.

It should be noted that nonwoven GDLs have a composite microstructure. To geometrically model the inherent composite nature of GDL, having both fiber and resin

in its microstructure as shown in Figure 2.12, first the fibrous skeleton was generated using statistical methods and then its pore space was filled by arbitrarily selected fillers. Different types of filler include thin sheets and spherical elements [75, 82] were used. The pore space of the fibrous skeleton was filled by stochastic methods with predefined probability functions or morphological operations. Thiedmann et al. modeled the GDL including the binder based on the stochastic geometrical data [83]. They assumed that the GDL was a stack of thin sections and constructed them as 2D random line tessellation to obtain the structural information of the reconstructed geometry. In these studies the interplay between the morphological and transport properties of the virtual composite microstructures has been overlooked.

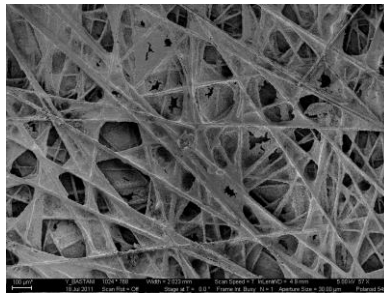


**Figure 2.12** SEM image of composite paper GDL.

## **2.4 Determining the Morphological Properties of Porous Media**

The set of morphological properties describing the internal structure of a porous medium includes its porosity, internal surface area, pore size, chord lengths and the shortest paths distributions. As shown in Figure 2.13, morphological properties can



quantify the available pore space of a porous medium. Knowing the morphological properties and the inter-relationship of physical and morphological properties of the porous media is greatly beneficial for design of porous medium.

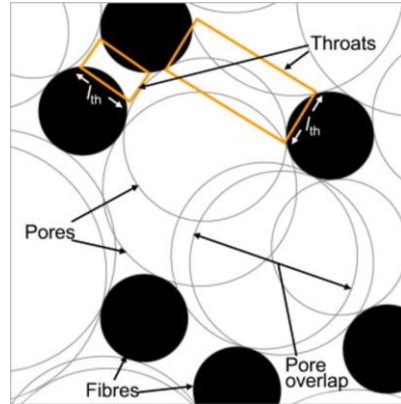


**Figure 2.13** Schematic of morphological description of the pore space.

Determining the morphological properties of porous media is greatly useful for many engineering applications and industries such as petroleum engineering, bioengineering, material engineering and energy sectors [84-86]. For example, in geosciences, waste disposal, landfill design and petroleum engineering quantitative knowledge of morphological properties of rocks and soil is a pre-requisite in the design process. The topology of rock and soil plays a vital role in determining the fluid transport, which is a crucial factor in designing the reservoir.

#### ***2.4.1 Experimental Methods for Determining Morphological Properties of Porous Media***

To determine some of the structural properties of porous materials experimental methods are used. For instance, porosimetry methods are used to find porosity, surface area, and density. In addition, porosimetry methods are used to quantitatively determine the pore size distribution of a porous medium. In this method a pressurized non-wetting liquid, e.g. mercury, is forced to intrude into the porous medium. The pore size is then found using Washburn's equation given as:

$$P_l - P_g = \frac{4 \sigma \cos \theta_c}{D_p}$$

where  $P_l$ ,  $P_g$ ,  $D_p$ ,  $\sigma$  and  $\theta_c$  are the pressure in liquid phase, pressure in gas phase, pore diameter, surface tension of liquid and contact angle of liquid on the porous structure surface, respectively. Mercury porosimetry can distinguish pores between 500  $\mu\text{m}$  and 3 nm. However, this method faces some limitations. As shown schematically in Figure 2.14, in a porous medium, pores with different shapes and connectivity might exist. Mercury porosimetry is not able to measure closed pores, since mercury cannot pass through the closed or dead end pores. The other important limitation is the fact that it measures the largest entrance of a pore not the actual internal pore size. Thus, mercury porosimetry results are different from the results attained from the images of SEM or optical micrographs. To find the connectivity of pores some numerical algorithms have been developed. However, numerous simplifying assumptions have been made such as assuming that the pores have perfect cylindrical shapes [81].

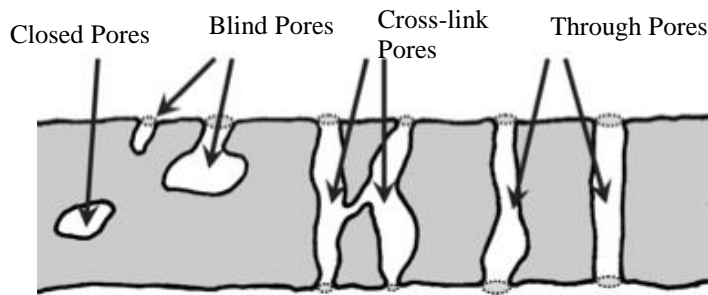


**Figure 2.14** The schematic of various types of pore in a porous medium.

Figure 2.15 shows an example of a pore size distribution in woven GDL based on mercury porosimetry. As shown in figure, by increasing the intrusion pressure smaller pores are accessible by mercury. The nano size pores are the pores that exist in the carbon fibers used in the GDL [10].

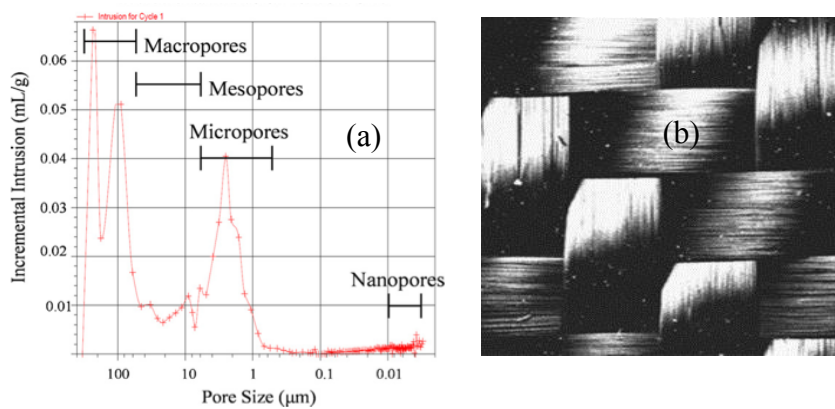


**Figure 2.15** (a) Pore size distribution for woven GDL, (b) Woven GDL [10].

If mercury is used as the non-wetting liquid in porosimetry, the total pore volume or porosity, density, and the surface area of a porous medium can also be found. The

procedure for finding the bulk density or the porosity of a medium is called pycnometry. Mercury pycnometry is a volume displacement technique that is mostly used for granules materials. Knowing the weight of the sample with and without mercury and the density of mercury, the volume of the penetrated mercury can be determined.

To find the internal porous surface area Rootare and Prenzlow [87] derived following equation

$$A = -\frac{1}{\sigma \cos \theta} \int_0^{V_m} P dV_m$$

where  $P$  and  $V_m$  are the pressure and volume of intruding mercury, respectively. This equation allows for converting the volume data into the corresponding surface area under the assumption of a reversible intrusion process. However, due to the cross-links between the pores, a direct conversion of volumetric data is not accurate. Inaccurate measurement especially in the high pressure or for medium with small pore sizes can significantly affect the calculated surface area. To increase the accuracy of the predicted internal surface area more recently nitrogen adsorption measurements techniques have been introduced [88].

Topological properties of the porous media, such as tortuosity, must also be determined. However, experimental methods alone are not capable of determining this property. In this case, the image processing techniques coupled with computational methods have to be utilized to find this morphological property of a porous medium. These methods characterize virtual 3D representations of the porous medium that has

been generated by imaging techniques. The high resolution images can be used to extract the morphological properties [29]. To find the morphological properties of a porous medium, the resulting images are post processed using commercial software such as MAVi, Avizo, and open source libraries such as DIPlib, ITK, Blob3D and Pore3D. These programs have been equipped with modified image filtering and segmentation algorithms and quantitative analysis tools to determine the morphology of porous media.

#### ***2.4.2 Numerical Methods for Determining Morphological Properties of Porous Media***

Numerical methods have been developed to determine the morphological properties of porous media. To find the pore size and its distribution various techniques have been used. As shown schematically in Figure 2.16, the most common method is to find the spherical distance of the points inside the void space to the surrounding solid boundaries [75, 83, 89]. In some studies instead of considering pores as 3D objects they are defined as 2D closed areas and the pore size is defined as the diameter of a circle with the area equal to the closed area [74, 90, 91]. Thiedmann et al. found the pore size distribution of the GDL from a 3-D graph representation of the pore space [75]. They defined the pore size as the largest spherical distance of a pore center to the solid phase. The introduced procedure only takes into account the largest pores belonging to the respective pore centers. Gaiselmann et al. found the pore size distribution of a virtual representation of carbon felt GDL [81]. To validate the accuracy of the virtual microstructure of the GDL, they compared the pore size distribution obtained from the virtual GDL to the pore size distribution found from the SEM images of the GDL. To

determine the pore size distribution they calculated the cumulative distribution function (CDF) of spherical contact distances of the pore phase.

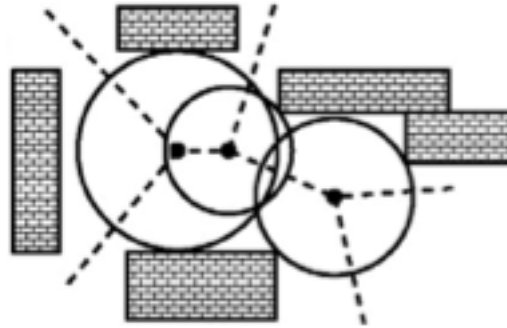


**Figure 2.16** Schematic of pore size determining procedure [75].

Knowledge of pore size distribution in the porous structures gives a quantitative understanding of the pore space in a medium, but it does not provide any information on the directionality and inhomogeneity of its available pore space. To this end, the chord lengths distribution has been introduced. As shown schematically in Figure 2.17, a chord length is defined as the distance between the internal solid boundaries in any desired direction. Chord length data can be used as an alternative metric for the pore size and its distribution represents the inhomogeneity and directionality of the pores in the microstructures. The chord lengths analysis quantifies the pore space features, which can be used for determining the dominant diffusion mode within the porous material. To find the chord length in a porous medium the desired cross section has to be determined. Cecen et al. used angularly resolved lineal path functions and found the chord length distribution in the micro porous layer of a PEMFCs [92]. Wargo et al. determined the chord lengths distribution in a GDL that has been coated with a micro porous layer to resolve the macro and micro scale interactions [28].

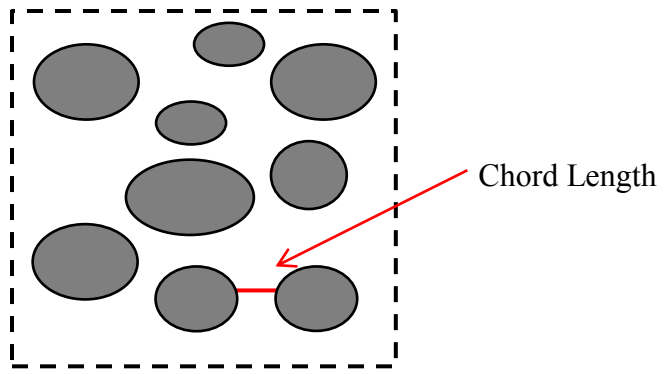


**Figure 2.17** Schematic of a chord length inside a porous medium.

Another important metric that has been recently introduced is the shortest paths length and its distribution inside the porous medium. The distribution of the shortest paths inside a porous structure is shown schematically in Figure 2.18. Rather than a single tortuosity value, representation of the tortuous paths as a distribution helps to better understand the spatial variation of a microstructure. Diffusivity of the porous substance not only depends on its available pore space (chord length) but also on its tortuous paths. Due to the inhomogeneity of the fibrous structures, finding the distribution of the shortest paths inside their void space is also necessary, in addition to the bulk tortuosity.

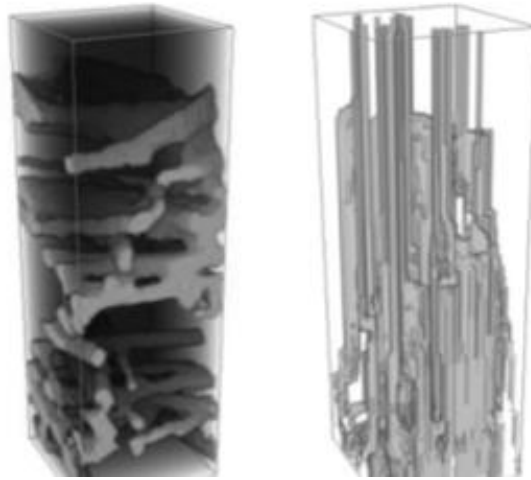


**Figure 2.18** (a) Voxel representation of fibrous porous media, (b) The shortest paths distribution in the porous domain [28].

The distribution of the shortest paths has been found for porous structure by using the Dijkstra's search algorithm [93]. To implement the search algorithm, a graph representation of porous medium is required. The graph representation can be constructed from either the 3D virtual images of a medium or from a 3D geometrical model of a medium [75, 92]. The vertex of the graph represents the solid phase in the porous structure and a link represents a physical connection between two nodes. Each link between any two pores represents the Euclidean distance between the two. The search algorithm is then implemented to find the shortest possible path from the vertices on the inlet to any of the vertices located at the designated exit.

Wargo et al. applied a Dijkstra's search algorithm to compute tortuous paths within a composite GDL. Using a FIB-SEM, they reconstructed the 3D representation of the medium and transformed the 3D voxel geometry into a 2D adjacency matrix [29]. Using a similar approach, Gaiselmann et al. found the shortest path distribution of a



virtual representation of carbon felt GDL [81] .

In porous materials, the structural and physical properties depend upon each other. Thus, for the purpose of material engineering, finding more accurate and less time demanding structural characterization methods is essential. The existing approaches to determine the morphological properties are based on the characterization of an existing porous structure. Thus, instead of a design tool they are only useful for characterization purposes. The available numerical characterization schemes offer useful platforms for evaluation of some morphological properties. However, they are computationally expensive. In the current study, these schemes are modified for higher accuracy and lower computational time. In this research, the geometry generation is automatically linked to the morphology characterization, which can be used for design purposes and as a characterization tool at the manufacturing stage.

## **2.5 Determining the Transport Properties of Porous Structures**

To numerically investigate the structure-transport interactions simulations have to be run at pore level i.e., micro scale. Recently, due to the availability of high performance computing, modeling the transport phenomena at the micro scale level has gained a lot of attention. Different approaches have been used such as pore network (PN), lattice Boltzmann models (LBM), and computational fluid dynamics.

PN modeling approaches that include percolation models, diffusion limited aggregation (DLA) models and anti-DLA models, are based on studying the transport

properties on an idealized representation of the pore structure [73, 91, 94-97]. These models are generally time efficient and can be used to predict the transport properties within an acceptable accuracy. Recent studies on PN models focus on extraction of more realistic 3D network representations of the porous media, using experimental imaging and morphology analysis [98-102]. However, the majority of the PN models are still based on the overly simplified networks of pores connected by straight throats as shown schematically in Figure 2.19. Although the PN models are time efficient, they are not ideal design tools because they require length correlations based on the properties extracted from an existing structure [91].

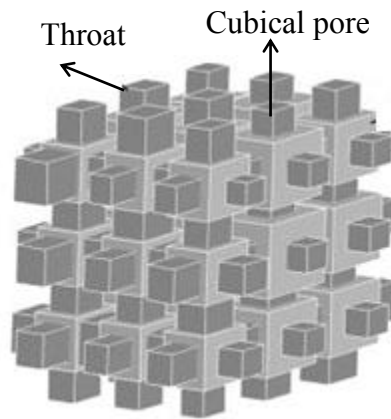


**Figure 2.19** Schematic of a porous PN model.

Another approach of micro scale modeling is solving the governing equations, such as Navier–Stokes (NS) equations in the virtual porous domain using computational fluid dynamic schemes (CFD) [103-105]. The CFD methods use standard techniques such as finite difference, finite volume or finite element to discretize the governing equations on the computational grid. These conventional approaches are mesh sensitive

with the limitation that a continuum flow field is assumed for all the flow regimes inside the pore structure, which may not be accurate [73].

More recent approaches to model the flow field inside the complex porous structures are the molecular dynamics (MD) [106, 107] and lattice Boltzmann methods (LBM) [108-115]. The molecular dynamics approach takes into account the movements and collisions of all individual molecules, constituting the fluid with a detailed description of the inter-molecular interactions. However, because of the complexity of interactions inside the porous domain and also the need to have a large number of molecules to model the fluid, the molecular dynamics models are computationally very expensive.

The LBM considers the behavior of a collection of particles comprised of a large number of molecules moving on a regular lattice, thereby reducing the degrees of freedom of the system and making the pore-scale simulation computationally less intense. Due to its numerical stability and constitutive versatility, the LBM has been considered a powerful tool for simulating complex flows. In LBM, the flow field is modeled as a collection of particles sitting on the nodes of lattice-like structures that interact with each other based on their velocity. Due to its underlying kinetic nature, the LBM has been found to be particularly useful in fluid flow applications involving interfacial dynamics and complex boundaries, e.g., multiphase or multi-component flows in porous medium. Therefore, compared to the conventional CFD methods, the LBM represents the pore morphology of the actual porous medium and the micro level description of the flow field more precisely, but they are computationally more demanding compared with the PN

models and conventional CFD simulations. Recently, LMB has been used to solve multicomponent, chemical reaction phenomena leading to the evolution of porous microstructure, the fracture propagation, and morphological change due to the coupling of applied forces and the flow field [113].

In addition to the elaborate numerical simulations at the pore scale level, various analytical models have been implemented to predict tortuosity and permeability of fibrous porous media based on fiber orientation. Wang et al. found the relation between the pressure drop and the structure of the spun bonded filter media [116]. They generated the layered 3D structure by assuming the fibers lie horizontally in the parallel planes without bending. Tomadakis and Robertson applied the electrical conduction principle to predict the permeability of viscous flow from a specific surface area and porosity, in a three-directional random fiber structures [117]. Tamayol and Bahrami presented a new analytical approach for evaluating the in-plane permeability by modeling the microstructure as a combination of equally sized, equally spaced fibers parallel and perpendicular to the flow [77].

Using the aforementioned methods, the transport properties such as tortuosity, permeability and diffusivity have been computed for the fibrous porous structures. However, in these studies the microstructures were simplified and the effect of the composite structure and the profile and curvature of the fibers were neglected.

In the current study, the flow field inside the pore structure is analyzed by CFD finite volume method using ANSYS FLUENT 14 and Geo-Dict 12.1, because of their

time efficiency, power to handle larger domain and availability. The suggested characterization approach is versatile and can be used for both design and analysis purposes. An automated method of generating the computational domains is suggested that facilitates the necessary parametric studies at the design phase. Because of the embedded parametric nature of the suggested modeling and characterization approach, it is possible to study the interplay between the morphology and transport properties of porous media.

## **2.6 Numerical Analysis of Complex Porous Media**

As mentioned earlier, fibrous porous media are often composite. In addition they may also be multilayered with a thin film coating, making them complex composite media. Coating a thin film on top of a porous medium changes its original properties, because the coating solution penetrates into the medium. However, to ensure the quality of the resulting complex composite material the relationship between processing parameters, microstructure's properties and the penetration has to be understood. In this section, the methods implemented to fabricate complex porous media are briefly discussed. Then, the numerical and experimental methods implemented to analyze the complex porous media are discussed.

### ***2.6.1 Fabrication of Complex Porous Media***

Several industry scale processes, such as roll coating [118], blade coating [119, 120], dip coating [121] and slot die coating [122-124] as shown schematically in Figure

2.20, have been used for addition of a thin film on top of porous media. These methods are all high speed coating technologies that are suited for mass production [125-127]. Ding et al. demonstrated the effectiveness of slot die coating in the manufacture of MEA of PEMFCs, which is a typical multilayer structure. In the slot die coating process the thickness of the coated layer can be controlled precisely, because it is a pre-metered process [128]. Using slot die coating multiple layers can be also coated simultaneously [129, 130]. Due to its advantages, the slot die coating process is selected as the method of interest in this study and herein the corresponding literature is presented.

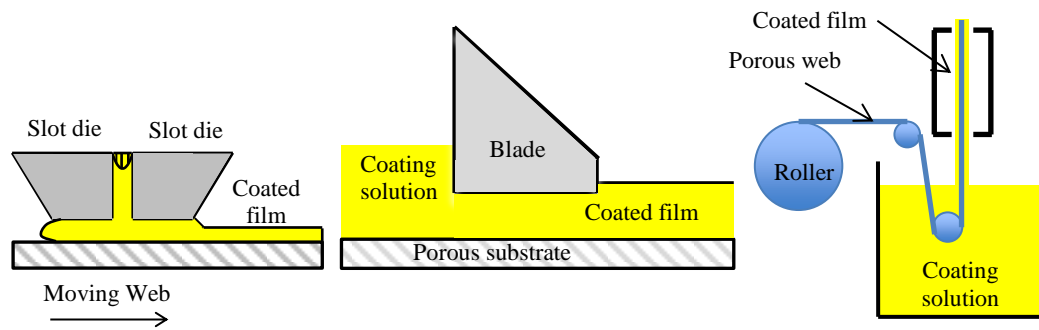


**Figure 2.20** The schematic of slot die, doctor blade and dip coating processes.

### ***2.6.2 Penetration of Coating Solution into the Porous Media***

As shown in Figure 2.21, in the slot die coating process a solution is forced through the die and is suspended onto a moving web/substrate that can be porous or nonporous, forming a thin layer on the substrate. If the web is porous, the coating solution is distributed on it and pushed into its pore space by an applied convection-driven pressure field. As shown schematically in Figure 2.21, beyond the slot die lip the pressure on the substrate is approximately atmospheric, while inside the coating bead the

pressure distribution has a peak value that is a function of the operating conditions [131, 132].

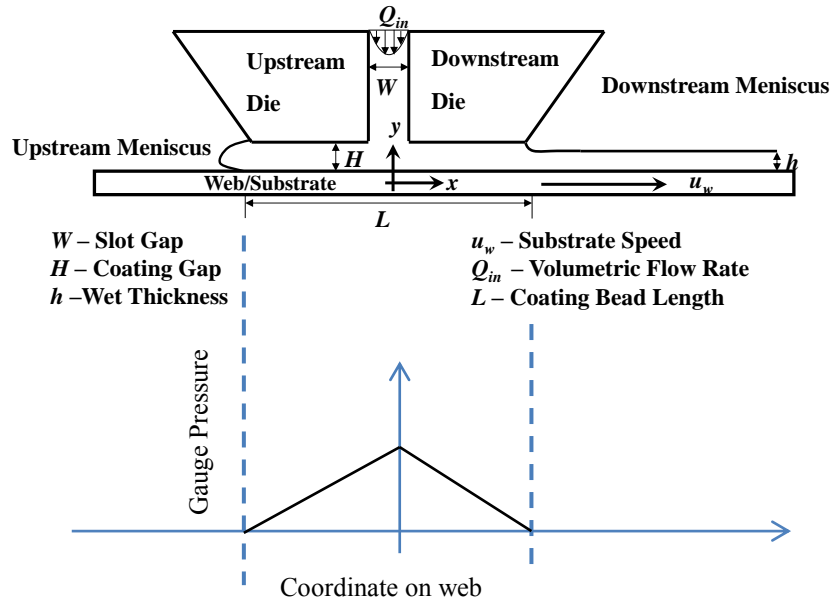


**Figure 2.21** Schematic of slot die coating process and the pressure distribution on the web.

In the coating bead region, penetration of the liquid into the porous web is driven by pressure and capillary forces, whereas in the film region is driven by capillary forces [123, 131, 133, 134]. The penetration process in the coating bead region is very complex and dynamic, with pressure pulses that are applied over very short times on the order of milliseconds, while the time scale in the film region is on the order of couple of seconds [123]. Because of both economics and functionality of the end product, controlling the penetration is critical [135].

To experimentally find the level of penetration several methods have been developed. One of the most common methods is to measure the electrical conductivity of

the coated web. The penetration level can be found by correlating the change in the electrical conductivity of the coated web to penetration depth [136]. In the paper industry, using ultrasound techniques the level of intrusion of coating liquid into the paper can be measured. To approximately determine the penetration depth gravimetric techniques are also used. In this method, the amount of coating liquid absorbed by the porous web will be determined [137]. Optical methods are also implemented to measure the penetration depth. In this approach, the penetration depth can be found based on the reflectance of the light that is omitted to the web [136].

The experimental investigation of the penetration process is a challenging task due to the complexity and diversity of fibrous structures. Thus, developing a model to predict the penetration is highly desirable, but so far only few studies exist dedicated to modeling this phenomenon [138-142]. Most of these studies used continuum models with overall representative properties that are estimated experimentally, such as effective permeability and porosity, representing the fibrous microstructure by 1D or 3D capillary lattices.

One of the contributing factors in the penetration of the liquid into the porous structure is the capillary force that is caused by the curvature of the interface between two phases. To consider the effect of the capillary forces on the penetration into the porous media the Lucas Washburn equation has been used by applying an effective capillary radius and length [143]. This equation assumes smooth, chemically homogeneous, and continuous cylindrical pores, the conditions that cannot be extended to random porous media. To modify Lucas Washburn model the capillary network model, has been



introduced [144-149]. The drawback of the suggested models is that some of the coefficients are ad-hoc parameters and adjusted to force the models' predictions to agree with the experimental data. Models that represent the porous structure as a bundle of parallel capillary tubes are not accurate enough, since the actual pore space is too complex to be presented by perfect lattice.

To determine the fluid penetration a multi scale approach is required. The overall behavior can be investigated at the macro scale through solving Darcy's law and mass and momentum conservations, where the permeability and capillary pressure must be calculated as a function of saturation level from a microscopic model. To find the microfluidic behavior some studies used pore morphology models and LBM [61, 150]. In this instance, pore morphology models determine the fluid-gas interface by approximating the porous media with spheres of different sizes and incorporating Young-Laplace equation for the capillary pressure. Further, LBM was used to simulate two phase fluid flow in a 3D reconstructed random porous domain based on the x-ray microtomography, where it was shown that the flow behavior in the domain can be well described by the Lucas Washburn equation [135].

Although these studies have been able to describe the behavior of liquid penetration into a porous medium, they tend to provide little information on microfluidics in the porous media, and the deformation of the fluid interface and complex interactions with local geometry. Size variations of pores, sharp edges or corners, and blocked or dead-end pores may affect the liquid penetration behavior. Moreover, in the existing studies the flow field in the coating bead and the porous web were assumed to be

decoupled. This assumption may lead to inaccurate prediction of the penetration depth.

In this work, the effects of processing conditions on the liquid penetration driven by capillary forces and external pressure are investigated. For this purpose, a micro scale model that consists of the cross sections of the fibrous structure constructed by PS model with the boundary condition extracted from the macro scale numerical simulation of the coating procedure is established. Coupling the macro and micro scales simulations, the dynamic equations for this two-phase microfluidic interface tracking problem is solved. Implementing the suggested modeling approach the penetration process under various operating conditions will be studied.

## **2.7 Summary**

This chapter briefly outlines the existing approaches for virtual representation of fibrous porous media. These approaches are categorized as imaged base approaches and geometrical modeling approaches. The implemented techniques, their advantage and disadvantage are discussed. Since this study focuses on development of a design methodology for the fibrous media, the geometrical modeling approaches are selected instead of image base approaches. The implicit surface modeling technique that geometrically constructs the internal structure of porous media is discussed in more details. The limitation of the existing geometrical modeling approaches and the required improvement are also outlined in this chapter.

The structural properties of a porous medium i.e., its morphological properties are

introduced. The existing numerical and experimental methods for determining these properties are outlined. The advantage and disadvantage of the methods are also discussed. The modifications of the current approaches that are required for the design procedure are outline.

In the design process to determine whether the design criteria are satisfied, it is required to characterize the virtual representation of the porous medium before the manufacturing stage. To account for this, the introduced and existing numerical approaches for finding these properties are discussed along with their limitation and capabilities.

The complex porous media that is fabricated by coating a thin layer of film on top of a porous medium is selected in this study as a representative of layered composite media. The slot die coating process of a porous medium is selected as the manufacturing method of interest in this research, due to its ability to simultaneously coat multi layers. Numerical approaches used to solve the flow in the porous web and the remaining technical issues, such as the penetration of coating fluid into the web, are discussed. The literature on determining the penetration depth is outlined and the required investigation in this regard are also discussed.

### 3. MATERIALS

The GDLs that are considered as case studies in this work are given in Table 3.1. Toray 060 carbon paper, Freudenberg H2315 and an in-house fabricated carbon cloth GDLs are selected as a representative of paper, felt and woven fibrous media, respectively. These GDLs have the same porosity and thickness. Toray 060 carbon paper has a composite structure that is used for verification of the composite modeling approach [4].

**Table 3.1** Properties of GDLs selected as the case studies in this research.

Type	Paper structure[82]	Felt structure	Woven structure
	Toray 060 carbon paper	Freudenberg H2315	In house carbon cloth
Resin	17% weight fraction of thermoset resin	NA	NA
Porosity	78%	78% [65]	78%
Thickness	200 $\mu\text{m}$	200 $\mu\text{m}$ [151]	200~400 $\mu\text{m}$
Fibers size	7 $\mu\text{m}$	9 $\mu\text{m}$	7 $\mu\text{m}$

## **4. GEOMETRICAL MODELING OF FIBROUS POROUS MEDIA, METHODOLOGY**

Computational design of fibrous porous media requires efficient geometrical modelling methods. However, an efficient approach to build and modify these structures for the design purpose lacks in the field. This section presents a modelling approach suitable for different types of fibrous porous media. A previously developed periodic surface (PS) model is modified so that fibrous structures at the micro scale can be built. Modified PS model is periodic, implicit in nature, and is able to construct the three-dimensional representative volume elements (RVE) of variety of fibrous porous media. The modified PS model can be readily integrated with morphological and computational fluid dynamics analysis procedures. The volumetric mesh representation of RVE can be exported directly to the computational fluid dynamics simulation tools.

In this chapter, a brief overview of the original PS model is presented. The modified PS models used to model straight, bent and compressed fibers which will be used to construct the aforementioned microstructures are explained in detail.

### **4.1 Periodic Surface Modeling Methodology**

The PS model previously developed by Wang [64] is able to build 3D crystal and molecular structures more efficiently than explicit methods. Due to its periodic nature, modeling self-repeating geometries is convenient. By simply increasing or decreasing the number of periods for the RVE, the size of the model will be enlarged or shrunk with

more or less elements included, which is important in modeling RVEs. The PS model has the implicit form and is defined as [64]

$$\psi(\mathbf{r}) = \sum_{l=1}^L \sum_{m=1}^M \mu_{lm} \cos(2\pi\kappa_l(\mathbf{P}_m^T \cdot \mathbf{r})) = 0 \quad (4.1)$$

where  $\kappa_l$  is the scale parameter and  $\mu_{lm}$  is the periodic moment.  $\mathbf{r} = [x, y, z, w]^T$  is the location vector with homogeneous coordinates.  $w$  is assumed to be one, if not explicitly specified. The scale of  $\psi(\mathbf{r})$ ,  $L$ , is defined as the number of unique scale parameters in  $\kappa_l$ .  $\mathbf{P}_m$  is a basis vector defined as

$$\mathbf{P}_m = [a_m, b_m, c_m, \alpha_m]^T \quad (4.2)$$

where  $a_m, b_m, c_m$  are the components of the basis vectors in the Euclidean space and  $\alpha_m$  corresponds to the phase of the basis plane defined in  $\mathbf{P}_m$ . The basis vector can be in the following form

$$\mathbf{P}_m = \left\{ \begin{bmatrix} 0 \\ 0 \\ 1 \\ 1 \end{bmatrix} \begin{bmatrix} 1 \\ 0 \\ 0 \\ 1 \end{bmatrix} \begin{bmatrix} 0 \\ 1 \\ 0 \\ 1 \end{bmatrix} \begin{bmatrix} 0 \\ 0 \\ 1 \\ 1 \end{bmatrix} \dots \right\} \quad (4.3)$$

In addition, The degree of  $\psi(\mathbf{r})$ ,  $M$ , in Equation 4.1 is defined as the number of unique vectors in the basis vector set.

Figure 4.1 lists some examples of periodic surface models. Triply periodic minimal surfaces, such as P-, D-, G-, and I-WP cubic morphologies that are frequently referred to in chemistry and polymer literature, can be adequately approximated. Othe

than the cubic phase, other mesophase structures such as spherical micelles, lamellar, rod-like hexagonal phases can be also modeled.

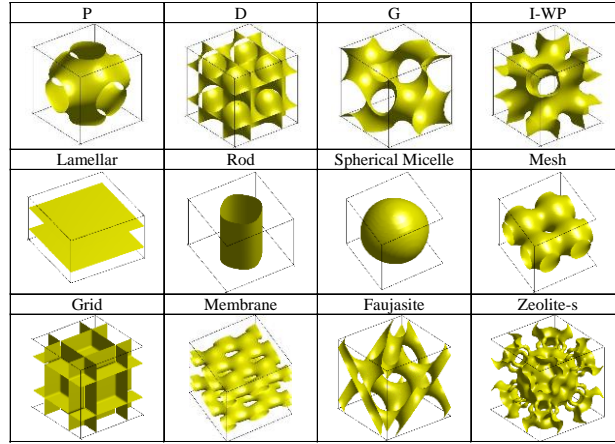


**Figure 4.1** Periodic surface models of cubic phase and mesophase structures [4].

## 4.2 Periodic Surface Modeling of Paper Porous Media

In paper fibrous porous structures, the fibers typically have circular cross-sections with minimal curvature compared to woven fibrous porous structures. Thus, their geometries can be approximately as straight cylindrical shapes. The rod surface model shown in Figure 4.1, is a good approximation of cylinders. Therefore it can be used to model the fiber geometry. The periodic surface model of a rod is [4]

$$\psi(x, y, z) = 4 \cos(2\pi x) + 4 \cos(2\pi y) + 3 = \psi_0 \quad (4.4)$$

Equation 4.4 represents a rod surface with the central axis along the z-axis direction, which is periodic in both x- and y-axis directions with the periodicity of 1. The corresponding parameters are given in Table 4.1.

**Table 4.1** The parameters for the PS model of a rod shape.

Parameters										
$L$	$M$	$\mu_{11}$	$\mu_{12}$	$\mu_{13}$	$\kappa_1$	$\kappa_2$	$\kappa_3$	$\mathbf{P}_1$	$\mathbf{P}_2$	$\mathbf{P}_3$
1	3	4	4	3	1	1	1	$[1\ 0\ 0\ 0]^T$	$[0\ 1\ 0\ 0]^T$	$[0\ 0\ 0\ 0]^T$

Basis vectors of the rod surfaces oriented along the x- and y-axes are given in Table 4.2. With these parameters, the rod surfaces can approximate the geometry of cylinders and therefore can be utilized to model straight fibers.

**Table 4.2** The basis vectors for rods in x- direction and y- direction.

Basis vector	$\mathbf{P}_1$	$\mathbf{P}_2$	$\mathbf{P}_3$
x- direction	$[0\ 1\ 0\ 0]^T$	$[0\ 0\ 1\ 0]^T$	$[0\ 0\ 0\ 0]^T$
y- direction	$[1\ 0\ 0\ 0]^T$	$[0\ 0\ 1\ 0]^T$	$[0\ 0\ 0\ 0]^T$

The fibers are modeled in a RVE or a cube that is large enough to represent the properties of fibrous porous media. The normalized size of the cube for the rod surface model is selected as  $x \in [0,1]$ ,  $y \in [0,1]$  and  $z \in [0,1]$ .

To represent cylindrical shapes with higher accuracy, more terms should be introduced into Equation 4.4. However, this leads a higher computational time. Figure 4.2 illustrates the PS model of a rod surface in the RVE and the difference between the cross section of the rod surface and a circle. As the isovalue  $\psi_0$  in Equation 4.4 changes, the diameter of the rod surface changes. As shown in Figure 4.2, the diameter of the fiber can be approximated by the distance between the positions with the maximum and minimum



y-coordinate values in the cross section of the rod as  $D = Y_{max} - Y_{min}$ .

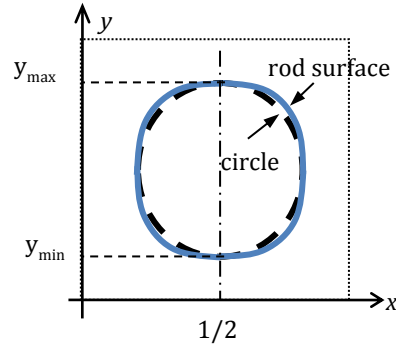


**Figure 4.2** Cylinder approximated by the rod surface [4].

If  $\psi(x, y, z) = \psi_0$ , the size of the rod can be determined. Since the period is set to 1, the cross section of the rod in the box is symmetric about  $x = 1/2$ , both  $Y_{max}$  and  $Y_{min}$  are located at  $x = 1/2$ . Therefore

$$4 \cos\left(2\pi \frac{1}{2}\right) + 4 \cos(2\pi y) + 3 = \psi_0 \quad (4.5)$$

Simplified form of Equation 4.5 is  $\cos(2\pi y) = \frac{1+\psi_0}{4}$ , which has two solutions for  $y \in [0,1]$ . These two solutions are  $Y_{max}$  and  $Y_{min}$ . Thus, the diameter can be found from Equation 4.6 as follow

$$D = Y_{max} - Y_{min} = 1 - \frac{\arccos\left(\frac{1+\psi_0}{4}\right)}{\pi} \quad (4.6)$$

For example, when  $\psi_0 = 0$ , the diameter is approximately 0.58. Conversely, given a known diameter  $D$ , the isovalue is calculated as  $\psi_0 = 4 \cos[\pi(1 - D)] - 1$ .

The fiber model in Equation 4.4 is located at the center of the RVE. Transformation operations are needed to generate models at other locations or with different orientations. It has been demonstrated that the transformation of a PS model is equivalent to the transformation of its basis vectors [64] . Therefore, the position and orientation of a fiber can be adjusted through the translation and rotation of the basis vectors  $\mathbf{P}_m$ .

In the RVE, a certain number of fibers can be generated with random values of orientations and locations.  $n$  fibers can be combined using the union operation as

$$\psi_{(\cup)}(x, y, z) = \min(\psi_1(x, y, z), \dots, \psi_n(x, y, z)) \quad (4.7)$$

where  $\psi_i(x, y, z)$  is the PS model of the  $i^{th}$  fiber.

To model the fibers that are bent or compressed, such as the ones shown in Figure 4.3, the deformation can be modeled by increasing the scales and degrees of the terms in Equation 4.1 i.e., introducing more terms in the PS model. With properly chosen parameters, this modified PS model is also able to construct rod surfaces with varied cross sections to model compressed fibers. For example, the modified PS model of fiber shown in Figure 4.3(a) is [152]:

$$\psi(x, y, z) = 4 \cos(2\pi x) + \cos(3\pi x) + 4\cos(2\pi y) + \cos\left(\frac{\pi y}{6}\right) + \frac{1}{4} \cos(3\pi(x + z)) + 2.5 = 0 \quad (4.8)$$

and the modified PS model of the compressed rod surface shown in Figure 4.3 (b) is [152] :

$$\psi(x, y, z) = 7 \cos(2\pi x) + 7 \cos(2\pi y) + 2 \cos(4\pi x) + 2 \cos(4\pi y) + 8 = 0 \quad (4.9)$$

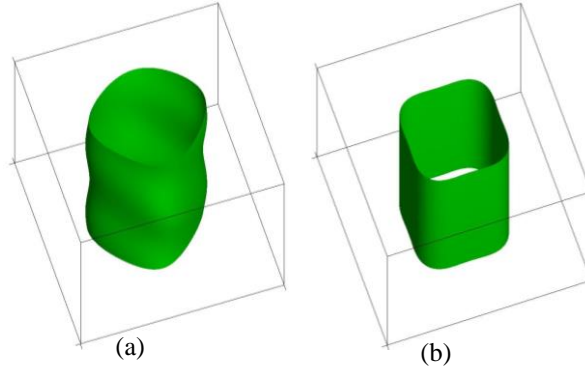


**Figure 4.3** Two compressed rod surfaces [152].

### 4.3 Periodic Surface Modeling of Felt Porous Media

The PS model discussed in Section 4.2 is based on the assumption that all fibers are straight. In order to build the bent rod model of fibers that are observed in felt materials, the cross section of the rod should shift by an amount varying along the rod axis. The shift is directly related to the phase  $\alpha_m$  in Equation 4.2. Therefore,  $\alpha_m$  has to be defined as a variable instead of a constant in the original PS model. To increase the flexibility, the PS model is modified into a new form and labeled as the generalized PS model. The generalized PS model is defined as [152]

$$\psi(\mathbf{r}) = \sum_{l=1}^L \sum_{m=1}^M \mu_{lm} \cos(2\pi \kappa_l (\mathbf{P}_m^T \cdot \mathbf{r})) + \sum_{s=1}^S \sum_{t=1}^T u_{lmst} \cos(2\pi f r_{lms} (\mathbf{q}_m^T \cdot \mathbf{r})) =$$

where  $\mathbf{P}_m = [a_m, b_m, c_m, \alpha_m]^T = [\mathbf{H}_m, \alpha_m]^T$  remains the same as Equation 4.2 and  $\mathbf{P}_m$  is now a major basis vector.  $\mathbf{q}_m = [e_{lmt}, f_{lmt}, g_{lmt}, \beta_{lmt}]^T = [\mathbf{G}_{lmt}, \beta_{lmt}]^T$  and  $\mathbf{q}_m$  is a minor basis vector of the generalized PS model.  $\mu_{lm}$  is a major moment whereas  $u_{lmt}$  is a minor moment.  $\kappa_l$  is a major scales whereas  $fr_{lms}$  is minor scales.

In the generalized PS model, the phase itself is a function with the similar form of the original PS model. The phase is represented by cosine functions. The phase in the generalized PS model is not constant but rather a periodic function. The generalized PS model exhibits higher flexibility in modeling. Using the generalized PS model, bent fibers, as shown in Figure 4.4, can be efficiently represented. To generate the fibrous structure it is required to relocate and translate the fibers in the RVE. The procedure for these two transformation operations are derived and described here.

#### 4.3.1 Rotation of the Generalized PS Model

The rotation matrix is defined as

$$\mathbf{R} = \begin{bmatrix} \xi_{11} & \xi_{12} & \xi_{13} & \xi_{14} \\ \xi_{21} & \xi_{22} & \xi_{23} & \xi_{24} \\ \xi_{31} & \xi_{32} & \xi_{33} & \xi_{34} \\ \xi_{41} & \xi_{42} & \xi_{43} & \xi_{44} \end{bmatrix}$$

The elements of rotation matrix ( $\xi_{ij}$ ) are given in Table 4.3.  $\varphi$ ,  $\theta$  and  $\omega$  are the rotation angles about the x-, y- and z-axes, respectively.

**Table 4.3** The elements of the rotation matrix.

$\xi_{ij}$	1	2	3	4
1	$\cos\theta \cos\omega$	$-\cos\theta \sin\omega$	$\sin\theta$	0
2	$\cos\varphi \sin\omega + \sin\varphi \sin\theta$ $\cos\omega$	$\cos\varphi \cos\omega - \sin\varphi \sin\theta$ $\sin\omega$	$-\sin\varphi$ $\cos\theta$	0
3	$\sin\varphi \sin\omega - \cos\varphi \sin\theta$ $\cos\omega$	$\sin\varphi \cos\omega + \cos\varphi \sin\theta$ $\sin\omega$	$\cos\varphi \cos\theta$	0
4	0	0	0	1

Under the rotation operation, the surface model  $\psi(\mathbf{r}) = 0$  becomes  $\psi(\mathbf{R}^{-1} \cdot \mathbf{r}) =$

0. That is [152]:

$$\psi(\mathbf{R}^{-1} \cdot \mathbf{r}) =$$

$$\sum_{l=1}^L \sum_{m=1}^M \mu_{lm} \cos\left(2\pi\kappa_l(\mathbf{P}_m^T \cdot \mathbf{R}^{-1} \cdot \mathbf{r}) + \sum_{s=1}^S \sum_{t=1}^T u_{lmst} \cos\left(2\pi f r_{lms}(\mathbf{q}_{lmt}^T \cdot \mathbf{R}^{-1} \cdot \mathbf{r})\right)\right) = 0$$

Since  $\mathbf{R}^{-1} = \mathbf{R}^T$ , then

$$\psi(\mathbf{R}^{-1} \cdot \mathbf{r}) =$$

$$\sum_{l=1}^L \sum_{m=1}^M \mu_{lm} \cos\left(2\pi\kappa_l((\mathbf{R} \cdot \mathbf{P}_m)^T \cdot \mathbf{r}) + \sum_{s=1}^S \sum_{t=1}^T u_{lmst} \cos\left(2\pi f r_{lms}((\mathbf{R} \cdot \mathbf{q}_{lmt})^T \cdot \mathbf{r})\right)\right) = 0 \quad (4.11)$$

Equation 4.11 shows that the rotation operation of the generalized PS model can be accomplished by the rotation of the major and minor basis vectors. The basis vectors can be considered as the sum of two vectors with phase separated as follow:

$$\mathbf{P}_m^T = [\mathbf{H}_m, \alpha_m] = \mathbf{H}_m^* + \boldsymbol{\alpha}_m^*, \text{ where } \mathbf{H}_m^* = [\mathbf{H}_m, 0] \text{ and } \boldsymbol{\alpha}_m^* = [0, \alpha_m]$$

$$\mathbf{q}_{lmt}^T = [\mathbf{G}_{lmt}, \beta_{lmt}] = \mathbf{G}_{lmt}^* + \boldsymbol{\beta}_{lmt}^* \text{ where } \mathbf{G}_{lmt}^* = [\mathbf{G}_{lmt}, 0] \text{ and } \boldsymbol{\beta}_{lmt}^* = [0, \beta_{lmt}]$$

Substituing the new form of  $\mathbf{q}_{lmt}$  and  $\mathbf{P}_m$ , the Equation 4.11 becomes:

$$\begin{aligned} \psi(\mathbf{R}^{-1} \cdot \mathbf{r}) = & \sum_{l=1}^L \sum_{m=1}^M \mu_{lm} \cos \left( 2\pi \kappa_l \left( (\mathbf{R} \cdot \mathbf{H}_m^*{}^T)^T \cdot \mathbf{r} + \boldsymbol{\alpha}_m^* \cdot \mathbf{R}^T \cdot \mathbf{r} \right) \right. \\ & \left. + \sum_{s=1}^S \sum_{t=1}^T u_{lmst} \cos \left( 2\pi f r_{lms} \left( (\mathbf{R} \cdot \mathbf{G}_{lmt}^*{}^T)^T \cdot \mathbf{r} + \boldsymbol{\beta}_{lmt}^* \cdot \mathbf{R}^T \cdot \mathbf{r} \right) \right) \right) = 0 \end{aligned}$$

Because  $\boldsymbol{\alpha}_m^* \cdot \mathbf{R}^T \cdot \mathbf{r} = \alpha_m$  and,  $\boldsymbol{\beta}_{lmt}^* \cdot \mathbf{R}^T \cdot \mathbf{r} = \beta_{lmt}$  the new form of the rotated generalized PS model is

$$\begin{aligned} \psi(\mathbf{R}^{-1} \cdot \mathbf{r}) = & \sum_{l=1}^L \sum_{m=1}^M \mu_{lm} \cos \left( 2\pi \kappa_l \left( (\mathbf{R} \cdot \mathbf{H}_m^*{}^T)^T \cdot \mathbf{r} + \alpha_m \right) + \right. \\ & \left. \sum_{s=1}^S \sum_{t=1}^T u_{lmst} \cos \left( 2\pi f r_{lms} \left( (\mathbf{R} \cdot \mathbf{G}_{lmt}^*{}^T)^T \cdot \mathbf{r} + \beta_{lmt} \right) \right) \right) = 0 \end{aligned} \quad (4.12)$$

Equation 4.12 implies that the rotation operation does not change the phase of

each cosine basis function.

### 4.3.2 Translation of the Generalized PS model

The translation operation can be derived similarly. When the translation matrix  $\mathbf{T}$  defined as  $\mathbf{T} = \begin{bmatrix} \mathbf{I}_{3 \times 3} & t \\ \mathbf{0} & 1 \end{bmatrix}$  is applied, translated generalized PS model is [152]

$$\psi(\mathbf{T}^{-1} \cdot \mathbf{r}) = \sum_{l=1}^L \sum_{m=1}^M \mu_{lm} \cos\left(2\pi\kappa_l(\mathbf{P}_m^T \cdot \mathbf{T}^{-1} \cdot \mathbf{r}) + \sum_{s=1}^S \sum_{t=1}^T u_{lmst} \cos\left(2\pi f r_{lms}(\mathbf{q}_{lmt}^T \cdot \mathbf{T}^{-1} \cdot \mathbf{r})\right)\right) = 0$$

Defining  $\mathbf{T}_t = (\mathbf{T}^{-1})^T = \begin{bmatrix} \mathbf{I}_{3 \times 3} & \mathbf{0} \\ -t^T & 1 \end{bmatrix}$  then gives:

$$\psi(\mathbf{T}^{-1} \cdot \mathbf{r}) = \sum_{l=1}^L \sum_{m=1}^M \mu_{lm} \cos\left(2\pi\kappa_l((\mathbf{T}_t \cdot \mathbf{P}_m)^T \cdot \mathbf{r}) + \sum_{s=1}^S \sum_{t=1}^T u_{lmst} \cos\left(2\pi f r_{lms}((\mathbf{T}_t \cdot \mathbf{q}_{lmt})^T \cdot \mathbf{r})\right)\right) = 0$$

With basis vectors decomposed,

$$\psi(\mathbf{T}^{-1} \cdot \mathbf{r}) = \sum_{l=1}^L \sum_{m=1}^M \mu_{lm} \cos\left(2\pi\kappa_l(\mathbf{H}_m^* \cdot \mathbf{T}^{-1} \cdot \mathbf{r} + \boldsymbol{\alpha}_m^* \cdot \mathbf{T}^{-1} \cdot \mathbf{r}) + \sum_{s=1}^S \sum_{t=1}^T u_{lmst} \cos\left(2\pi f r_{lms}((\mathbf{T}_t \cdot \mathbf{q}_{lmt})^T \cdot \mathbf{r})\right)\right) = 0$$

$$\sum_{s=1}^S \sum_{t=1}^T u_{lmst} \cos\left(2\pi f r_{lms} (\mathbf{G}^*_{lmt} \cdot \mathbf{T}^{-1} \cdot \mathbf{r} + \boldsymbol{\beta}^*_{lmt} \cdot \mathbf{T}^{-1} \cdot \mathbf{r})\right) = 0$$

Because  $\boldsymbol{\alpha}^*_m \cdot \mathbf{T}^{-1} \cdot \mathbf{r} = \alpha_m$  and,  $\boldsymbol{\beta}^*_{lmt} \cdot \mathbf{T}^{-1} \cdot \mathbf{r} = \beta_{lmt}$  the translated generalized PS model is

$$\begin{aligned} \psi(\mathbf{T}^{-1} \cdot \mathbf{r}) = \\ \sum_{l=1}^L \sum_{m=1}^M \mu_{lm} \cos(2\pi \kappa_l ((\mathbf{T}_t \cdot \mathbf{H}^*_m)^T \cdot \mathbf{r} + \alpha_m) + \sum_{s=1}^S \sum_{t=1}^T u_{lmst} \cos(2\pi f r_{lms} ((\mathbf{T}_t \cdot \mathbf{G}^*_{lmt})^T \cdot \mathbf{r} + \beta_{lmt}))) = 0 \end{aligned} \quad (4.13)$$

The shape of the cross section of the rod surface is largely determined by the parameters  $\mu_{lm}$ ,  $\kappa_l$  and  $\mathbf{P}_m$  whereas the extension of bending is determined by the parameters  $u_{lmst}$ ,  $f r_{lms}$  and  $\mathbf{q}_m$  in Equation 4.10. Since the cross section of the simple rod surface is a good approximation of a circle, the parameters of  $\mu_{lm}$ ,  $\kappa_l$  and  $\mathbf{P}_m$  can remain the same as those used for straight fibers. The relationship between the diameter of a bent rod and the isovalue can still be represented by Equation 4.6. Implementing the generalized PS model fibers that are bent or (curved) can be modeled. An example is illustrated in Figure 4.4. The fiber is constructed assuming one term for the minor phase.

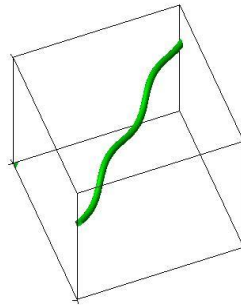


**Figure 4.4** A bent rod surface model with a sinusoidal shape [152].



When the cross section of a straight rod shifts  $u \cos(2\pi fr(\mathbf{q}_m^T \cdot \mathbf{r}))$  to form a bent fiber, the resultant cross section changes consequently. As illustrated in Figure 4.5, when the cross section  $CS_2$  shifts a distance of  $v$ , the cross section of the rod surface changes to a new shape, and the narrowest diameter changes from  $D$  to  $D' = D \cos \alpha$ . Then, the difference between  $D$  and  $D'$  is  $D_{diff} = D' - D = D(1 - \cos \alpha)$ . When the bent shape is  $\cos(2\pi fr(\mathbf{q}_m^T \cdot \mathbf{r}))$ , the maximum value of  $\alpha$  is  $\alpha_{max} = \arctan v$ , and the maximum difference is

$$D_{diff-max} = D' - D = D(1 - \cos \alpha_{max}) = D(1 - \cos(\arctan v))$$

For slight bending the amplitude is small, therefore  $D_{diff-max}$  can be negligible.

For instance, when  $v$  is 0.1,  $D_{diff-max} = 0.00496D$ .

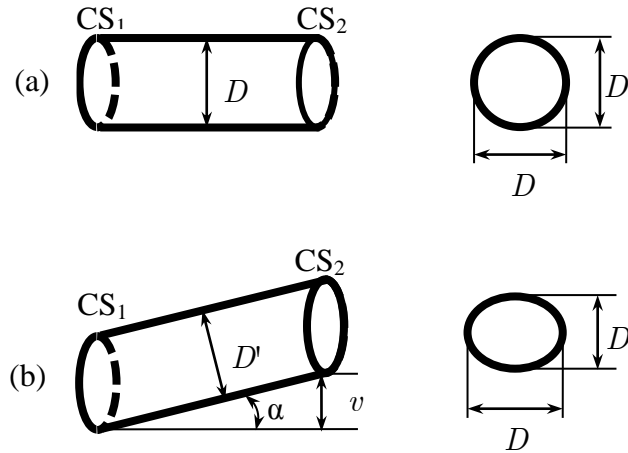


**Figure 4.5** Illustration of the cross section change due to the shift (a) geometry and cross section before shift (b) geometry and cross section after shift [152].

#### 4.4 Periodic Surface Model for Woven Porous Media

To model the woven yarns of a fibrous porous media, the generalized PS model can be used. In Equation 4.10, if  $S = 1$  and  $T = 1$ , the phase function is simplified to  $u \cos(2\pi fr(\mathbf{q}_m^T \cdot \mathbf{r}))$  and the bent rod can be written as[152]

$$\psi(x, y, z) = 4 \cos(2\pi x + u \cos(2\pi fr z)) + 4\cos(2\pi y) + 3 = \psi_0 \quad (4.14)$$

The rod surface described by Equation 4.14 has the medial axis in the x-z plane with the specified parameters of  $u$  and  $fr$ . The resulting model has a sinusoidal shape similar to that shown in Figure 4.4. For the central curves of a bent rod surfaces oriented in the x-y and y-z planes, the respective major and minor basis vectors are given in Table 4.4. For the central curves of bent rod surfaces oriented in other planes, the basis vectors can be obtained through the rotation operation introduced in the previous section. It should be noticed that as more cosine basis functions are added for the phase, the shape of the fiber will be more flexible at the cost of computation.

**Table 4.4**The basis vectors for bent rods in x- direction and y- direction.

Basis vector	$\mathbf{P}_1$	$\mathbf{P}_2$	$\mathbf{P}_3$	$\mathbf{q}_{111}$
x- direction	$[0 \ 1 \ 0 \ 0]^T$	$[0 \ 0 \ 1 \ 0]^T$	$[0 \ 0 \ 0 \ 0]^T$	$[1 \ 0 \ 0 \ 0]^T$
y- direction	$[1 \ 0 \ 0 \ 0]^T$	$[0 \ 0 \ 1 \ 0]^T$	$[0 \ 0 \ 0 \ 0]^T$	$[0 \ 1 \ 0 \ 0]^T$

As shown, the curvature of the fibers can be modeled by PS model, however due to the external forces exerted to the yarn for fabricating the woven materials, the fibers are compressed. Thus, to model a woven porous media the generalized PS model is

modified to model the compressed bent fibers. Figure 4.6(a) shows a bent fiber with compressed cross-sections at certain contact positions with other fibers in the domain. To model the compressed fiber the cross section of a straight fiber is changed periodically along the  $z$  direction while the isovalue is modified. Therefore, the model becomes

$$\psi(x, y, z) = 4 \cos(2\pi x) + \cos(2\pi y) (\cos(2\pi z) + 3) + 0.95 \cos(2\pi z) + 6.55 = 0$$

The above rod surface equation can be rewritten as

$$\begin{aligned} \psi(x, y, z) = & 4 \cos(2\pi x) + 3 \cos(2\pi y) + 0.95 \cos(2\pi z) + 0.5 \cos(2\pi(y + z)) + \\ & 0.5 \cos(2\pi(y - z)) + 6.55 = 0 \end{aligned} \quad (4.15)$$

The period and phase of the bent rod surface model in Equation 4.15 are adjusted so that the contact and bending positions are overlapped. The resulted PS model is

$$\begin{aligned} \psi(x, y, z) = & 4 \cos\left(2\pi x + 0.3 \cos\left(\pi z - \frac{\pi}{2}\right)\right) + 3 \cos(2\pi y) + 0.95 \cos(2\pi z) + \\ & 0.5 \cos(2\pi(y + z)) + 0.5 \cos(2\pi(y - z)) + 6.55 = 0 \end{aligned} \quad (4.16)$$

Equation 4.16 can be used to model the bent and compressed fibers by adjusting the major scale parameters.

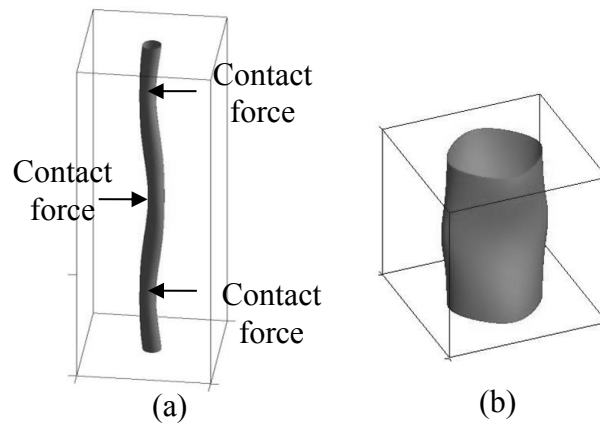


**Figure 4.6** Illustration of a bent compressed fiber PS model (a) contact points (b) the cross section change [152].

#### 4.5 Summary

The proposed modeling approach enables simulation-based design of fibrous porous media. In this chapter, a generalized PS model is presented which is a new method to represent the geometry of microscopic fibrous porous media. The fibers in the models, either straight or bent, are efficiently constructed. The shape, position, and orientation of fibers are controllable to serve the purpose of design. Compared to existing modeling methods for fibrous porous media, the generalized PS model has several advantages. The implicit nature of the model enables it to build 3D porous and complex structures more efficiently than explicit modeling approaches.

## **5. GEOMETRICAL MODELING OF FIBROUS POROUS MEDIA,**

### **RESULTS**

In this chapter the techniques used to generate microstructures of carbon paper, felt, composite carbon paper, and woven gas diffusion layers are explained. The optimization algorithms utilized to generate a realistic representation of paper and felt GDLs are explained. The virtually generated GDLs by the generalized PS model and SEM images of the actual GDLs are also compared.

#### **5.1 Periodic Surface Modeling of Carbon Paper Gas Diffusion Layers**

To demonstrate the feasibility of the proposed geometrical method, the microstructure of a carbon paper GDL is generated using PS model. The carbon fibers in the paper GDL are approximated as straight cylinders with negligible deformation. The carbon fibers are much longer than the micro scale RVE. Thus, they are assumed to be infinitely long. With these assumptions, a rod shape iso-surface given by Equation 4.1, can be used to represent the outer surface of the fibers.

To model the GDL, fibers are located in a RVE or a cube that resembles one period of the whole GDL. The range of the cube with normalized sizes is  $x \in [0, 1]$ ,  $y \in [0,1]$ , and  $z \in [0,1]$ . Due to the existing inhomogeneity in the porous structures, the RVEs are designed to represent both macro scale (bulk) and micro scale properties of the entire GDL. The proper size of RVE for fibrous structures is determined in the Chapter 8. However, the outlined procedures for geometrical modeling of the GDLs are independent

of the final size of RVE. Knowing the proper size for the RVE, the generated microstructures can be easily scaled to the desired size.

To model the fibrous bundle in the GDL it is assumed that the position and orientation of the fibers in the RVE are randomly distributed. Other than the spatial distribution of the fibers in the RVE, the solid volume fraction of the GDL and the diameter of the fibers have to be known. Then, the fiber skeleton of the GDL can be generated in the RVE using the union operation over the implicit functions of all the individual fibers in the domain.

$$\psi_U(r) = \min(\psi_1(r), \psi_2(r), \dots, \psi_n(r)) \quad (5.1)$$

As shown schematically in Figure 5.1, to locate an infinitely long and straight fiber of specific diameter in the space, two angles are needed. One is the in-plane angle ( $\varphi$ ) in the x-y plane and the other is the side angle ( $\theta$ ) in the z-x plane. The range for these parameters is determined by measuring the angle of the fibers from the SEM images.

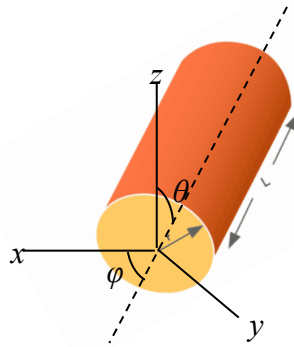


**Figure 5.1** Schematic representation of a fiber in the RVE.

Several samples of Toray carbon paper GDL are prepared and the cross sectional and top views SEM images of the GDL samples are taken. Using the image processing software provided by the SEM the side and in-plane angles of the fibers are found, as shown in Figure 5.2. A uniform distribution for the in-plane angle ( $\varphi$ ) and side angle ( $\theta$ ) is found. The range in which  $\varphi$  changes is set to be  $[0, \pi]$  based on the extracted measurements, similar to that shown in Figure 5.2. The range for the side angle ( $\theta$ ) is assumed to be  $[-\pi/36, \pi/36]$  so that the obtained model has a semi layer-by-layer structure.

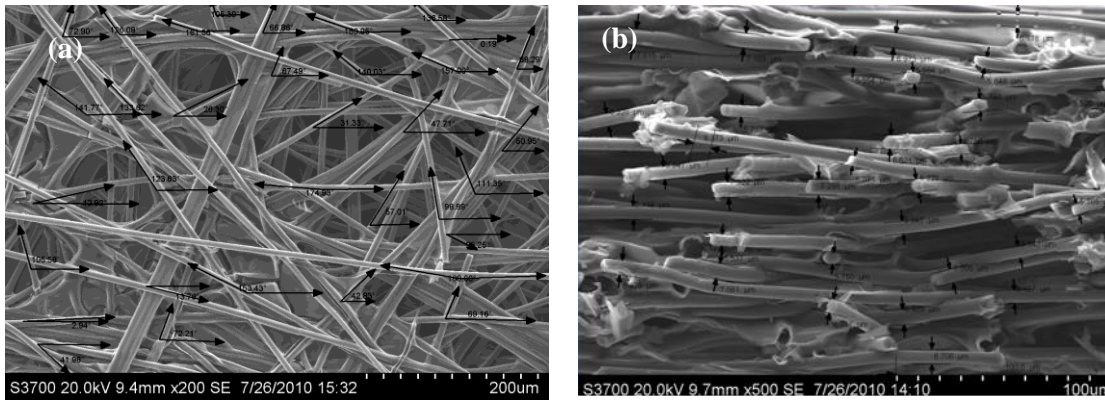


**Figure 5.2** SEM images of a GDL used to extract the distribution of the side and in-plane angles, (a) top view (b) cross sectional view.

As a result, the randomly generated fibers in the PS model may intersect with each other. Therefore, for accurate representation of the GDLs' structure and also to reduce the complexity of the domain in CFD, it is necessary to minimize the volume of intersections, based on fibers positions and orientations.

The RVE is converted to a sign function by the implicit surface model of each fiber. The points in the RVE that are located in the boundaries of the implicit surface have a negative iso-surface value, when their coordinates are inserted into the implicit

surface equation. The points outside the implicit surface boundaries have a positive iso-value. As shown schematically in Figure 5.3, the intersection portion can be obtained by

$$\psi_{(\cap)}(x, y, z) = \min_{1 \leq i \leq j \leq n} \left[ \max \left( \psi_i(x, y, z), \psi_j(x, y, z) \right) \right] \quad (5.2)$$

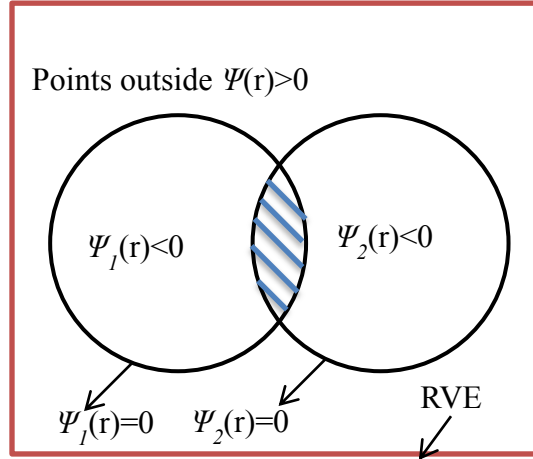


**Figure 5.3** Schematic of RVE with two fibers, illustrating the implicit surface boundaries.

To minimize the volume of intersections a nonlinear problem needs to be solved. This single-objective unconstrained nonlinear minimization problem can be solved with different optimization techniques. Since the fibers are densely packed, the assembly of the fibers cannot be easily divided into independent sets. If the intersection between two fibers is reduced sequentially by individual rotation and translation adjustment, as in a local optimization process, the intersection with other fibers most likely will be increased. Therefore, a global optimization algorithm is needed to solve this problem. In this study, the genetic algorithm (GA) is used for global optimization, which is an effective method of reducing the volume of intersections [104].



Fibers are all initially oriented along the x axis and located in the center of the RVE, then rotated around the y axis by an angle of  $\theta$  and z axis by the angle of  $\varphi$  followed by translation along the x, y, z axis by a distance of  $l_x$ ,  $l_y$  and  $l_z$ . The values of  $\theta$  and  $\varphi$  are randomly selected in the defined ranges. The range in which  $l_x$ ,  $l_y$  and  $l_z$  change is  $[1/2, -1/2]$ . In the optimization, the objective function is the volume of intersection portion  $\Omega$ , and the transformation parameters  $\theta$ ,  $\varphi$ ,  $l_x$ ,  $l_y$  and  $l_z$  are variables. The volume of intersection is found by estimating the number of voxels inside the iso-surface of  $\Omega$ . Then, the optimization problem is formulated as

$$\min \Omega (\theta, \varphi, l_x, l_y, l_z) \quad (5.3)$$

The optimization procedure is shown in Table 5.1. Both PS modeling and optimization procedures are implemented in MATLAB. The inputs for the minimization procedure include a number of factors;

- Objective function,
- Upper and lower bounds of the adjustment for all transformation parameters,
- Maximum number of generations,
- Population size,
- Initial values of parameters,
- Iso-value of the PS model used to define the diameter of the fibers,
- Discrete grid mesh of the domain,  $X_{\text{mesh}}$ ,  $Y_{\text{mesh}}$ , and  $Z_{\text{mesh}}$ , which determine the resolution of the model.

The maximum number of generations is set to be 300. The population size is 40. The transformation parameters  $\theta$ ,  $\varphi$ ,  $l_x$ ,  $l_y$  and  $l_z$  are stored in a single array  $T_{in}$ , during optimization. Their initial values are randomly generated. The adjustment ranges of  $\theta$ ,  $\varphi$ ,  $l_x$ ,  $l_y$  and  $l_z$  are set to be  $[-\pi/18, \pi/18]$ ,  $[-\pi/180, \pi/180]$ ,  $[-0.1, 0.1]$ ,  $[-0.1, 0.1]$  and  $[-0.1, 0.1]$ , respectively. The output of the optimized transformation parameters  $T_{out}$  is the optimized adjustment  $T_a$ .

In Figure 5.4 the orientation of 20 fibers in the RVE are optimized by GA to reduce the intersection volume. As shown in the figure, after optimization the intersection of the fibers are lower and the fibers are more uniformly distributed in the RVE.

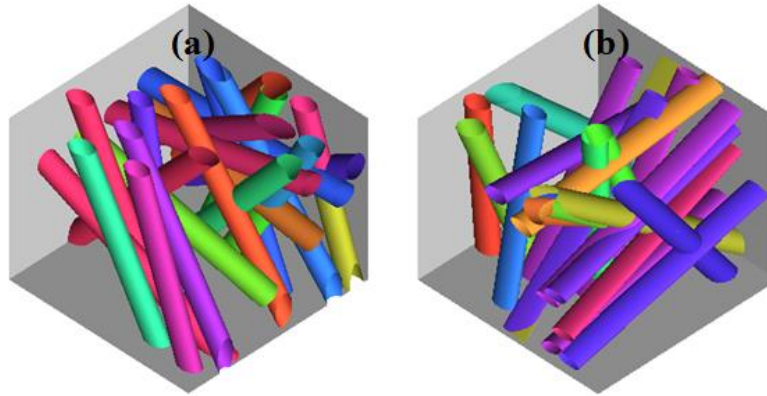


**Figure 5.4** Orientation of 20 fibers in RVE (a): with GA, (b): without GA [104].

The procedure of constructing a fibrous bundle in a GDL is shown in Figure 5.5. Assuming a porosity of 0.78 and fiber diameter of  $7\mu\text{m}$ , the GDL is modeled as shown in Figure 5.6. As illustrated, the constructed GDL resembles the actual GDL having a semi-layer structure in the through plane and randomly distributed fibers in the in plane

directions. However, the impregnated resin in the GDL structure is ignored. The procedure to model the resin will be explained in section 5.4.

**Table 5.1** The genetic algorithm optimization procedure for minimizing the volume of intersection [4].

<p><b>INPUT:</b> <math>T_{in}</math> – the array of initial values of transformation parameters <math>\theta, \varphi, l_x, l_y, l_z</math>;  <math>U</math>– the array of the upper bounds for all transformation parameters;  <math>L</math>– the array of the lower bounds for all transformation parameter  <math>X_{mesh}, Y_{mesh}, Z_{mesh}</math>– the <math>l_x \times l_y \times l_z</math> 3D grid mesh of the domain;  <math>N_{gen}</math> – the maximum number of generations;  <math>N_{pop}</math> – population size;  <math>isoV</math>– the iso-value of the PS model;  <math>N_{fiber}</math>– the number of fibers;</p> <p><b>OUTPUT:</b> <math>T_{out}</math> – the array of the optimized transformation parameters;</p> <p><b>Function</b>  Initialize <math>l_x \times l_y \times l_z</math> 3D array <math>V</math> with very large values;  Initialize <math>l_x \times l_y \times l_z</math> 3D array <math>W</math> with very large values;  <b>FOR</b> <math>i = 1</math> to <math>N_{Fiber}</math>  <math>V_{new} = \Psi_i(X_{mesh}, Y_{mesh}, Z_{mesh});</math>  <math>W_{new} = \max (V, V_{new}); V = \min (V, V_{new});</math>  <math>W = \min (W, W_{new});</math>  <b>END</b>  <math>Mv =</math> the number of voxels in <math>W</math> with isovalue <math>\leq isoV</math>;  <math>Mv = Mv / (l_x \times l_y \times l_z);</math>  <math>T_a = GA(Mv, N_{Pop}, N_{Gen}, N_{Fib}, L, U);</math>  <math>T_{out} = T_{in} + T_a;</math></p>
---

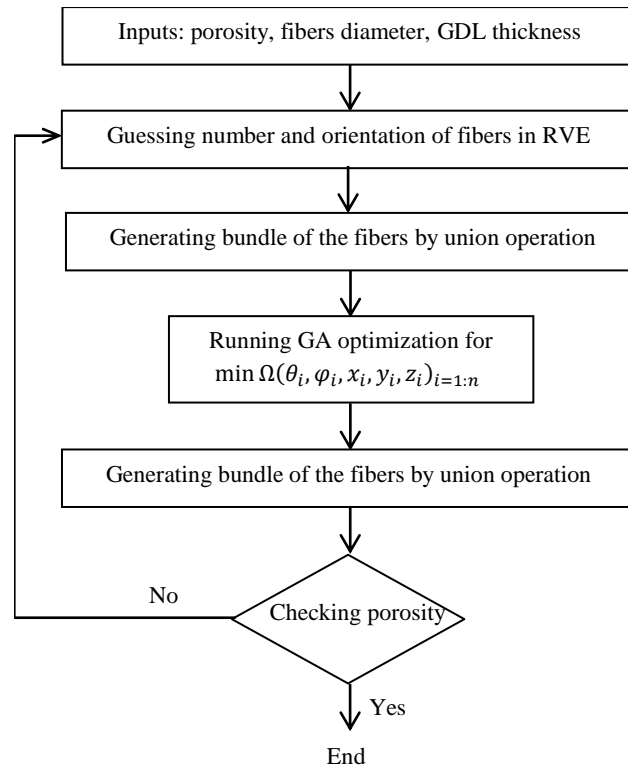


**Figure 5.5** Block diagram of generating the fibers skeleton.

To investigate the effectiveness of the optimization procedure on the reduction of the intersection volume, GDL microstructures are generated with and without applying the genetic algorithm optimization for two fiber sizes and two porosities. The intersection portion in each microstructure is calculated and shown in Figure 5.7. Due to the randomness of the fibers distribution in the RVE, the PS model is run seven times for each configuration; thus, 28 structures are generated. For accurate comparison, the porosity of the GDL is kept constant. The decrease in fiber intersections is calculated based on the percent change of the intersection portion in the optimized structure relative to the medium intersection portion of the unoptimized structures. As illustrated in Figure 5.7, the intersections decreased as the porosity and diameter increase. Because of the sparse structures at higher porosity, fibers can be reoriented freely, resulting in fewer

intersections.

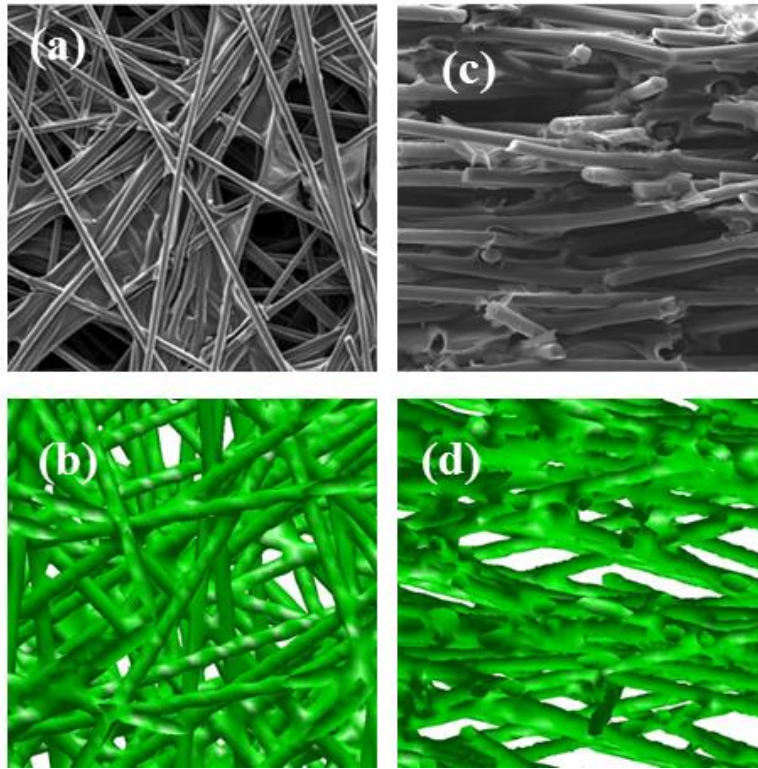


**Figure 5.6** Fibers bundle top view from (a): SEM image, (b) PS model, cross sectional view from (c) SEM image, (d) PS model.

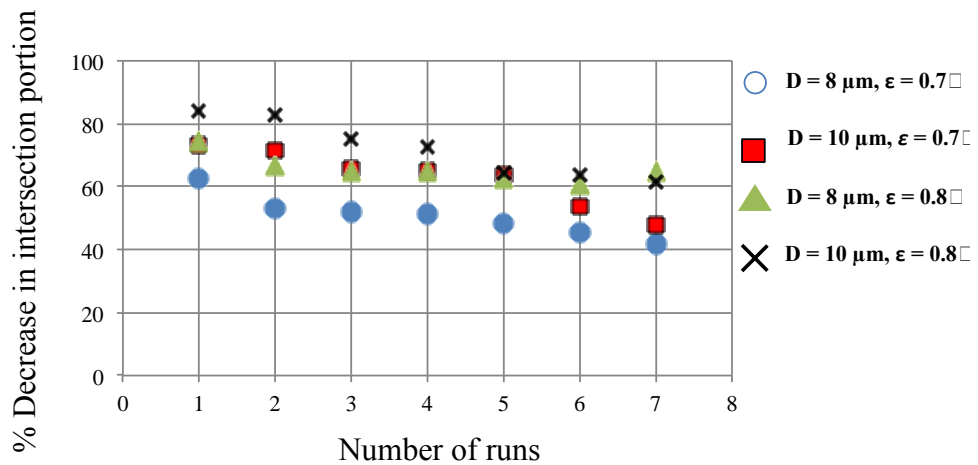


**Figure 5.7** Decrease in fibers intersection due to the genetic algorithm optimization [4].

## 5.2 Periodic Surface Modeling of Felt Gas Diffusion Layers

As shown in Figure 5.8, the deformation of the fibers in the felt porous media cannot be ignored. As described in Chapter 4, the deformation of the fibers is modeled by superposition of several cosine terms within the generalized PS model. To construct the whole felt structures two approaches are suggested. The first approach is to use the generalized PS model combined with an optimization to reduce the intersection of fibers similar to that of paper structure. However, here the frequency and amplitude of each of the cosine terms and the number of the superposed cosine terms are extra optimization variables. Thus, curvature and deformation of each fiber can be reinforced by the optimization procedure. This approach is a purely geometrical approach that does not consider the forces that fibers exert to one another.

The second approach called herein as, Energy Coupled Modeling approach, takes into account the effect of the forces exerted by the fibers on to one another. It is assumed that due to these forces the fibers are bent and the stored strain energy of the whole felt structure changes accordingly. However, the final fiber configuration in a felt structure of a known porosity belongs to a configuration that has the minimum volume of intersection and stored strain energy. To find this configuration a double objective minimization function is solved to determine the orientation and curvature of the fibers in the GDL structure. The final spatial orientation and deformation of the fibers are found by implementing this double objective minimization procedure.

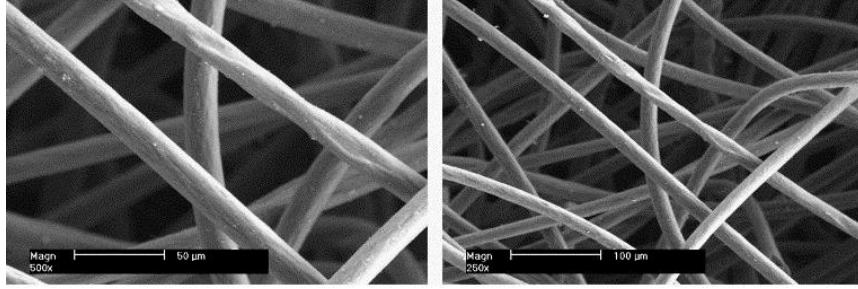


**Figure 5.8** The SEM images of carbon felt GDL [153].

Both procedures are used to construct the microstructure of a Freudenberg H2315 carbon felt GDL. To determine the advantages and disadvantages of each of the methods further characterization of the virtual microstructures is needed that will be discussed in Chapters 7 and 9.

### ***5.2.1 Geometrical Modeling of Felt Gas Diffusion Layers using Generalized PS Model***

To construct Freudenberg H2315 carbon felt GDL it is assumed that all the fibers are initially straight and are located in the RVE with the predefined random distribution for the orientations and positions. Then, using the generalized PS model the curvature of the fibers is modeled by addition of the cosine minor phases, which allows the fibers to bend. As shown in Figure 5.9, the curvature of the fibers depends not only on the amplitude and frequency of the cosine wave but also on the number of waves that are superimposed. Thus, to model the curved fibers numbers of cosine terms, orientation of these waves and the amplitude and frequency of each wave have to be found.

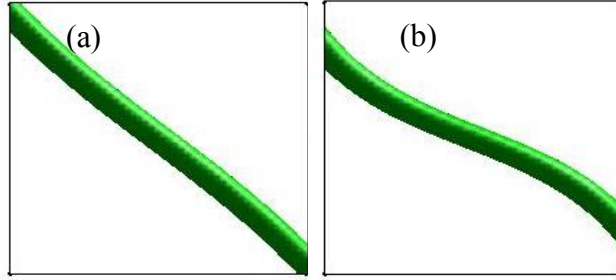


**Figure 5.9** Bent fiber in a RVE, (a) one cosine term, (b) superposition of two cosine terms.

To find the set of fibers that minimizes the intersection volume in the RVE the genetic algorithm optimization embedded in MATALAB is coupled with the generalized PS model. The optimization function is defined as

$$\min \Omega(\theta_i, \varphi_i, x_i, y_i, z_i, u_{ij}, fr_{ij}, m)_{i=1:n \ \& \ j=1:m} \quad (5.4)$$

where  $n$  is the number of the fibers,  $\theta_i, \varphi_i, x_i, y_i, z_i, u_{ij}, fr_{ij}$  and  $m$  are the orientation and position, amplitude and frequency and the number of terms of the minor phase for each fiber and are serving as the optimization parameters. The optimization procedure is described schematically in Figure 5.10.



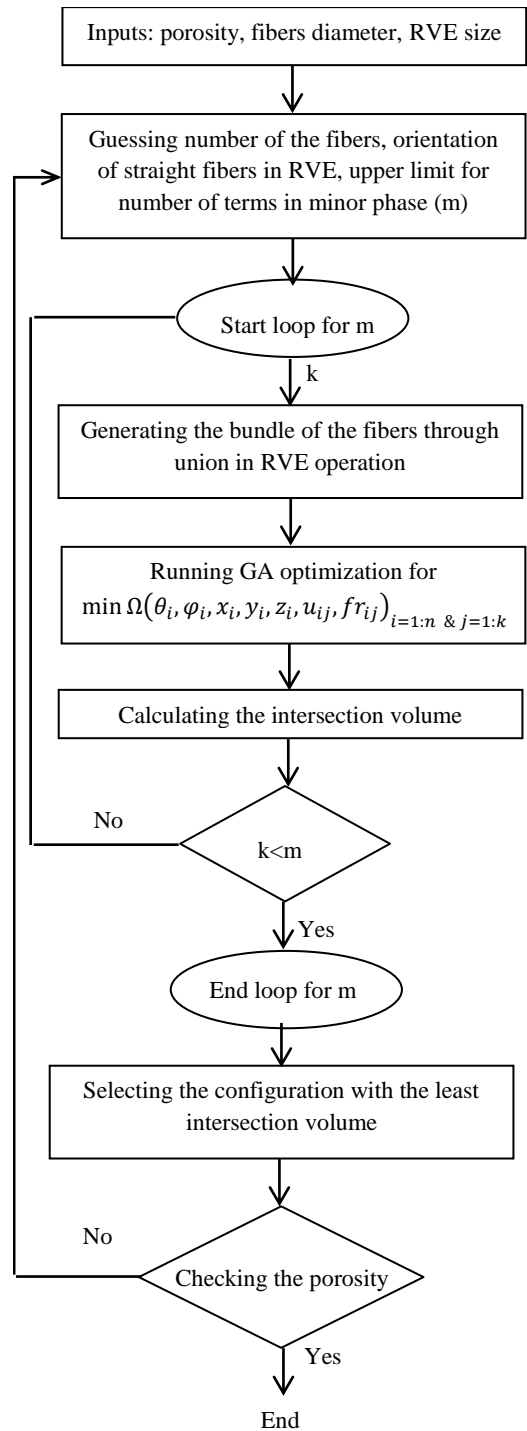


**Figure 5.10** The geometrical PS model procedure.

The ranges in which  $\theta$ ,  $\varphi$ ,  $u$  and  $fr$  can change are set to be  $[0, \pi]$  and  $[-\pi/18, \pi/18]$ ,  $[0, 0.1]$  and  $[0, 2]$  based on the measurements extracted from SEM images. Using the

proposed procedure the structure of Freudenberg carbon felt is generated as shown in Figure 5.11. As depicted in the figure, the constructed GDL resembles the actual GDL very well. The curvature of the fibers can be observed both in through plane and in plane directions.

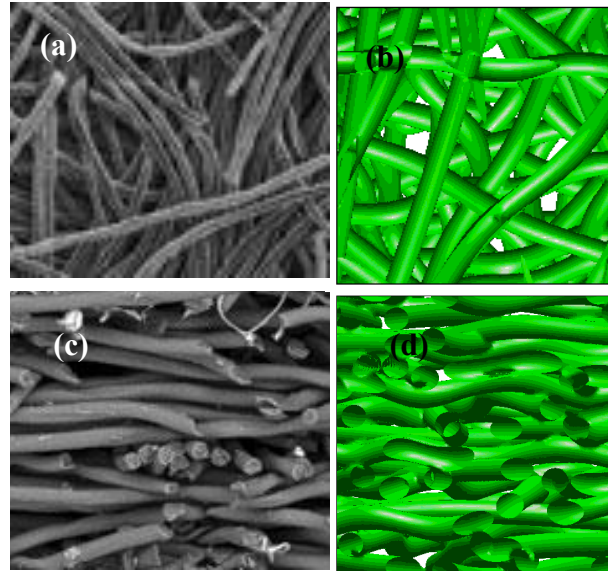


**Figure 5.11** Freudenberg H2315 carbon felt GDL (a) and (b) top views (c) and (d) cross sectional views, from geometrical modeling approach and SEM images.

### ***5.2.2 Energy Coupled Modeling of Felt Gas Diffusion Layers using Generalized PS Model***

Implementing the energy coupled modeling approach the microstructure of Freudenberg H2315 carbon felt GDLs is generated. In this approach the stored strain energy of the fibers in the RVE has to be determined. To find the stored strain energy carbon fibers are assumed as deflected beams and the stored energy is calculated by the conventional beam theories. In general, the strain energy is given by

$$U = \frac{1}{2} \int_V \epsilon^T C_\epsilon dV \quad (5.5)$$

where  $U$  is the strain energy of a beam element,  $\epsilon$  the column matrix of strains,  $C_\epsilon$  material constitutive matrix and  $dV$  is the differential volume element.

If the deformation of a beam is such that its cross sections remain in a plane and normal to the locus of the centroids, the beam's deflection can be assumed as an Euler-Bernoulli beam. In this case, defining the central axis (or locus of centroids) completely defines the shape of the beam, as illustrated in Figure 5.12. The profile of the beam can be defined by a discrete set of nodes along the beam. For Euler-Bernoulli beam the strain energy can be simplified to

$$U = \frac{1}{2} \int_0^S EI \left( \frac{d^2 w_c}{dx^2} \right)^2 dx \quad (5.6)$$

where  $I$  is the second moment of area of the beam cross-section,  $E$  is modulus of elasticity and  $w_c$  is the displacement of the centroid as shown in Figure 5.12. In Equation 5.6,  $\frac{d^2 w_c}{dx^2}$  can be approximated by the curvature of the central axis of the beam as follow

$$U = \frac{1}{2} \int_0^S EI \kappa^2 ds \quad (5.7)$$

where  $\kappa$  is the curvature of the deformed locus of centroids and  $S$  is the arc length along the locus of centroids.

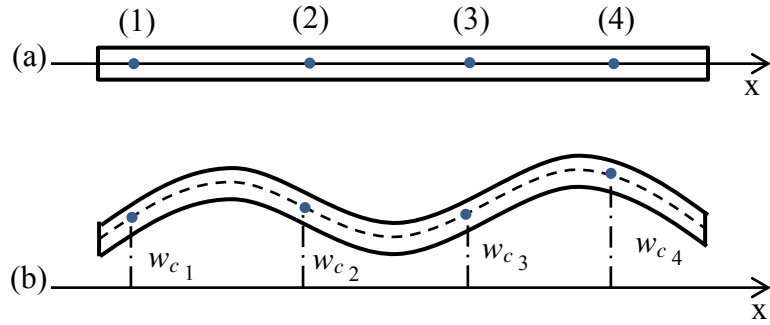


**Figure 5.12** (a) Original beam, (b) deformation of Euler-Bernoulli beam.

The felt GDL is modeled as a bundle of bent fibers in the RVE. Each fiber is combination of superposed cosine waves where the final orientation of the fiber is determined by rotation and translation of fiber's central axis. The translation and rotation of fibers in the RVE do not affect the stored strain energy, because the energy required for transformation is in the form of kinetic energy. On the other hand, the amplitude, frequency and number of superposed cosine terms directly affect the stored strain energy.

If the minor phase of a fiber is  $\sum_{i=1}^m u_i \cos(2\pi f r_i x)$ , where  $m$  is the number of the cosine term,  $u_i$  and  $f r_i$  are the amplitude and frequency of each term, the stored strain energy due to the deflection of the fiber is given as,

$$U = \frac{EI}{2} \sum_{i=1}^m \int_0^S \kappa_i^2 ds \quad (5.8)$$

by substitution of the curvature of each fiber, the stored strain energy is

$$U = \frac{EI}{2} \sum_i^m \int_0^S (u_i (2\pi fr_i)^2 \cos(2\pi fr_i x))^2 dx \quad (5.9)$$

By summation over all the fibers in the RVE, the stored energy of felt GDL can be calculated as follow

$$U = \frac{EI}{2} \sum_j^n \sum_i^{m_j} \int_0^S \left( u_{ji} (2\pi fr_{ji})^2 \cos(2\pi fr_{ji} x) \right)^2 dx \quad (5.10)$$

where  $n$  is the number of the fibers in the RVE. Finding the stored strain energy, now the double objectives minimization problem can be defined as follow:

$$\min \left[ \Omega_1(\theta_i, \varphi_i, x_i, y_i, z_i, u_{ij}, fr_{ij}, m)_{i=1:n \& j=1:m} \text{ and } \Omega_2(u_{ij}, fr_{ij}, m)_{i=1:n \& j=1:m} \right] \quad (5.11)$$

The optimization procedure is the same as the procedure described schematically in Figure 5.9, with the exception that instead of a single objective function, the double objective function defined by Equation 5.11 is used. Utilizing the same range for  $\theta$ ,  $\varphi$ ,  $u$  and  $fr$  as the previous approach, the Freudenberg H2315 carbon felt GDL is reconstructed. As shown in Figure 5.13, the microstructure resembles the SEM image of the GDL. However, the fibers have lower curvature comparing to the curvature of fibers in virtually generated felt structure by the geometrical modeling.

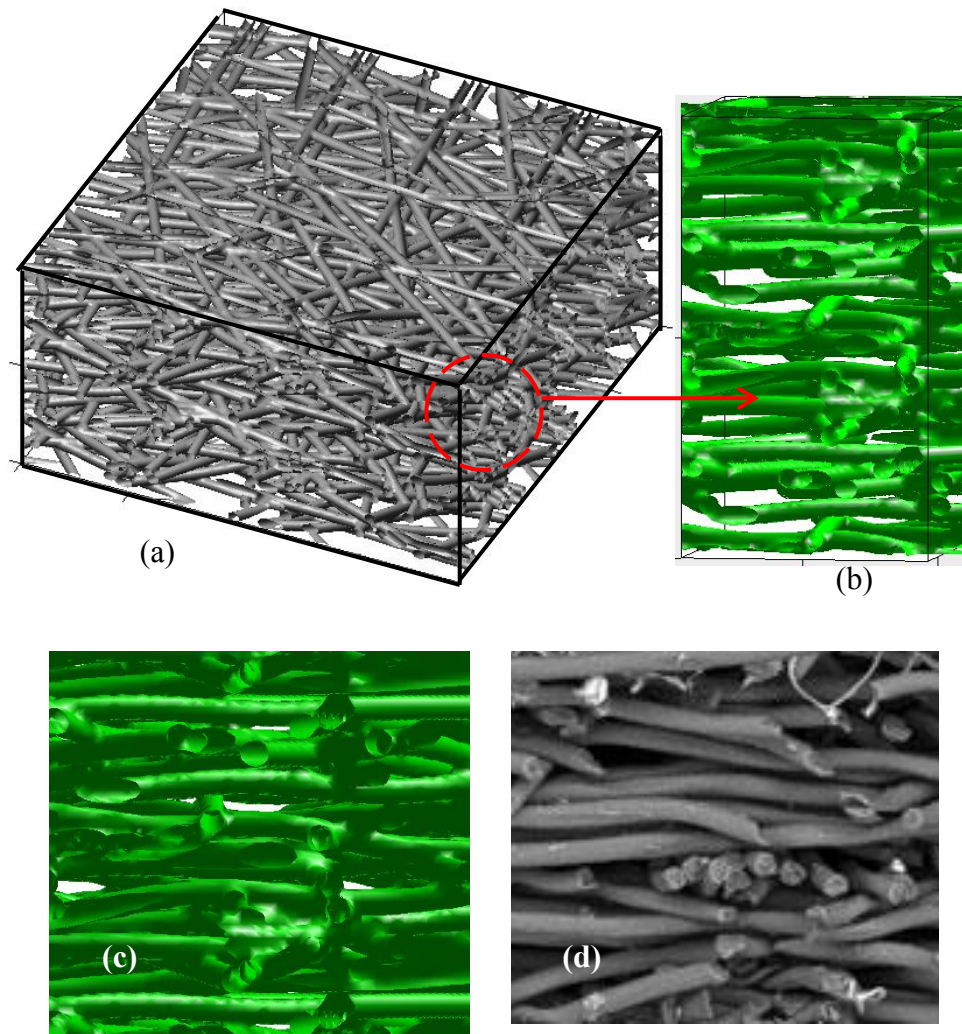


**Figure 5.13** Freudenberg H2315 carbon felt GDL reconstructed by energy coupled modeling approach (a) isometric view, (b) and (c) the zoom in view, (d) SEM image.

### 5.2.3 Effect of Optimization on the Characteristics of Virtual Felt GDL

The intersection volume of Felt GDLs generated by energy coupled modeling approach for two porosities is shown in Figure 5.14. As depicted in the figure, for lower porosities the intersection volume is larger due to the denser structure. The stored strain

energy of the generated microstructures is shown in Figure 5.15. As shown, when the number of the minor phase is low ( $m = 1$  and  $m = 2$ ) the stored strain energy of felt structures is lower. However, the intersection volume is higher. The intersection volume of GDL generated by geometrical modeling approach is given in Table 5.2. Implementing both geometrical modeling and energy coupled modeling approaches resulted to approximately lower intersection volume. However, as shown in Table 5.3 the stored strain energy of the microstructures generated by the geometrical modeling approach is larger compared to those generated by energy coupled modeling approach. Although both approaches have a minimum intersection volume the amplitude and frequency and number of cosine terms for each fiber are different from one modeling technique to another, because stored strain energy in the energy coupled modeling approach is constrained to a minimum value. This constraint acts as a limiting force to prevent extensive bending.

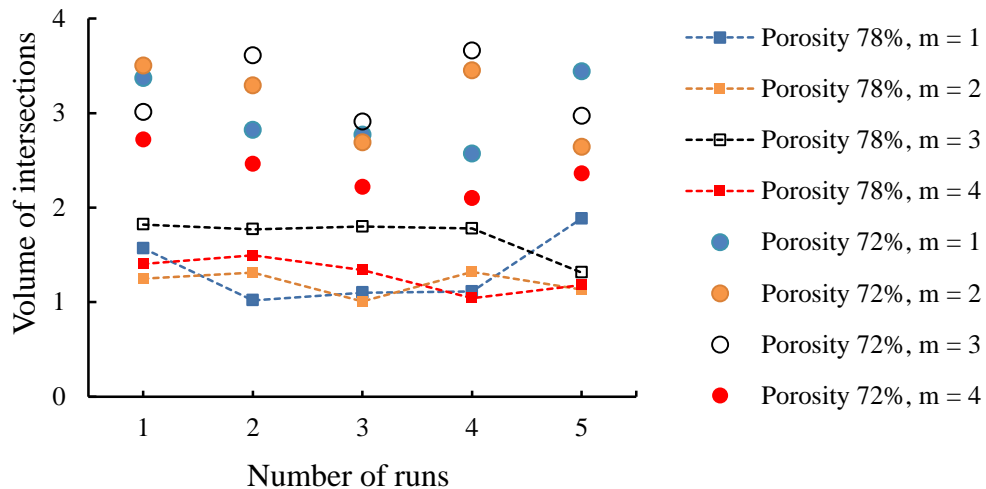


**Figure 5.14** The change in the intersection volume of felt GDL due to the energy coupled modeling approach.

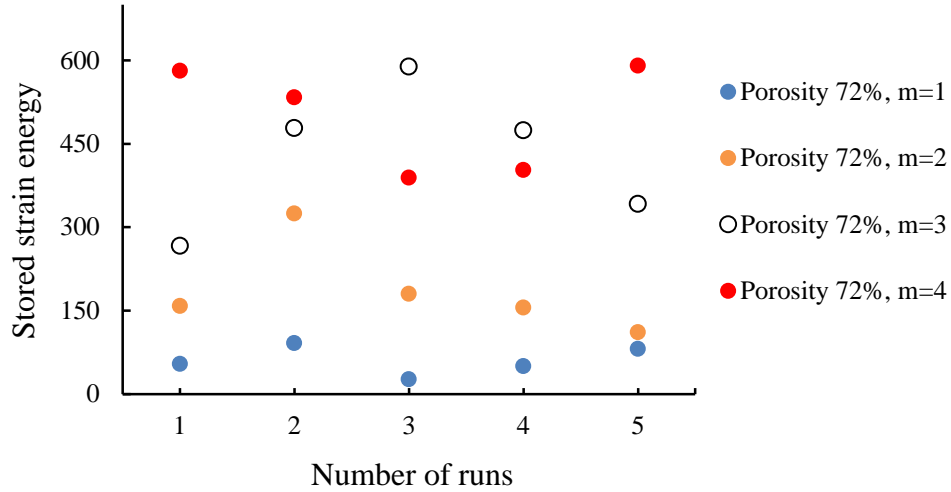


**Figure 5.15** The stored strain energy of the felt microstructures with porosity of 0.72 generated by to the energy coupled modeling approach.

**Table 5.2** The intersection volume in geometrical modeling approach, porosity 0.78.

Runs	$m = 1$	$m = 2$	$m = 3$	$m = 4$
Run1	2.20	0.63	0.88	0.89
Run2	2.73	0.79	0.77	0.89
Run3	3.05	0.77	1.14	0.88
Run4	2.53	0.93	0.80	0.85
Run5	2.60	0.96	0.72	1.14
Run6	2.93	1.27	0.81	0.84
Run7	3.15	1.10	0.95	1.11
Run8	2.60	0.96	0.72	1.14
Run9	2.93	1.27	0.81	0.84
Run10	2.60	0.96	0.72	1.14
Average	2.73	0.96	0.83	0.97



**Table 5.3** The stored strain energy in geometrical modeling approach, porosity 0.78.

Runs	$m = 1$	$m = 2$	$m = 3$	$m = 4$
Run1	236.017	$4.98 \times 10^3$	$6.36 \times 10^3$	$6.60 \times 10^3$
Run2	145.23	$6.34 \times 10^3$	$8.36 \times 10^3$	$1.07 \times 10^4$
Run3	234.73	$4.76 \times 10^3$	$6.10 \times 10^3$	$1.11 \times 10^4$
Run4	133.78	$2.95 \times 10^3$	$4.92 \times 10^3$	$8.36 \times 10^3$
Run5	170.06	$4.77 \times 10^3$	$5.62 \times 10^3$	$9.30 \times 10^3$
Run6	114.5	$4.54 \times 10^3$	$8.80 \times 10^3$	$8.12 \times 10^3$
Run7	227.75	$4.48 \times 10^3$	$7.45 \times 10^3$	$1.02 \times 10^4$
Run8	170.6	$4.77 \times 10^3$	$5.62 \times 10^3$	$9.30 \times 10^3$
Run9	114.45	$4.53 \times 10^3$	$8.80 \times 10^3$	$8.12 \times 10^3$
Run10	170.6	$4.77 \times 10^3$	$5.61 \times 10^3$	$9.27 \times 10^3$
Average	171.77	$4.69 \times 10^3$	$6.76 \times 10^3$	$9.11 \times 10^3$

### 5.3 Periodic Surface Modeling of Cloth Gas Diffusion Layers

Using the modified generalized PS model for compressed bent fibers, introduced in Chapter 4, woven fibers are generated. The major scale parameters in Equation 4.16 are adjusted to have the contact and bending positions overlapped. To model woven fibers of different curvature, the major scale parameters can be changed. The modified PS model is given by [152]

$$\begin{aligned} \psi(x, y, z) = & 4 \cos\left(2\pi x + 0.41 \cos\left(3\pi z - \frac{\pi}{2}\right)\right) + 3 \cos(2\pi y) + 0.95 \cos(6\pi z) + \\ & 0.5 \cos(2\pi(y + 3z)) + 0.5 \cos(2\pi(y - 3z)) + 6.55 = 0 \end{aligned} \quad (5.12)$$

The example of a woven structure is shown in Figure 5.16. The structure has six fibers within the domain of  $x \in [0, 1]$   $y \in [0, 1]$  and  $z \in [0, 1]$  that are generated by translation and rotation of the fiber given by Equation 5.12. It can be observed that at the contact locations, fibers are compressed and deformed accordingly. For each fiber, the locations where it is compressed are modeled by controlling the major scale parameters whereas the bending is controlled separately by the minor scale parameters. The orientation and translation of fibers are calculated so that fibers are properly crossed or parallel. The rotations are 90 degrees. The corresponding translation vectors of the six fibers are listed in Table 5.4. The deformed shape is an approximation of the woven fibers geometry rather than the result of physics-based modeling.

**Table 5.4** Translation vectors of the six woven fibers [152].

Fiber number	Translation vector coordinates		
	x	y	z
1	0.41	-0.318	0
2	0.72	0	0
3	0.41	-0.318	0
4	0.38	0.204	0
5	0.33	-0.433	0
6	0.28	0.204	0

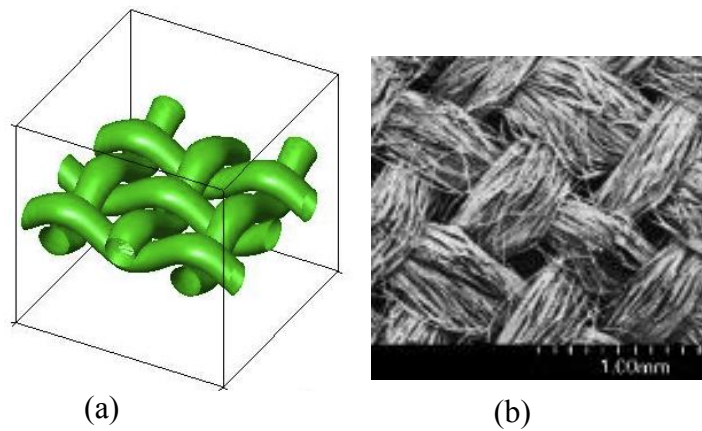


**Figure 5.16** (a) An isometric view from modified generalized PS model of woven fibers [152] (b) top view from SEM image [154].

#### **5.4 Periodic Surface Modeling of Carbon Paper Gas Diffusion Layers Including the Binder**

The composite structure of a GDL is constructed at two steps, first the fibrous structure is generated and then the binder is integrated with the fibers skeleton. Knowing the weight fraction of fibrous skeleton in the composite and the fibers' diameter ( $D$ ), the fiber skeleton of the GDL is generated implementing the modeling approach described in Section 5.1.

Because of the material properties of the resin and the rapid impregnation process, only the final composite structure is modeled in this work. The resin-fiber bond that forms the composite nature of a GDL is modeled in two steps. A block diagram depicting the process is shown in Figure 5.17. To model the resin, first a Minkowski summation of

fibers matrix (here set  $A$ ) with a structure element (SE) that represents the resin, is performed. As shown in Figures 5.18 (a) and (b), Minkowski summation of  $A$  and SE defined as  $B = A \oplus SE = \{a + se | a \in A, se \in SE\}$ , results in thickening of the fibers bundle. In the second step, an erosion operation is conducted on set  $B$ , the outcome of the first step. The erosion defined as  $B \cdot SE = B \ominus (-SE)$  is the Minkowski subtraction (shown by  $(\ominus)$ ) of  $B$  with the reflected set of SE. The erosion process leads to the shrinking of set  $B$  as illustrated in Figure 5.18 (c) [155]. By implementing this two-step procedure all the pores that are smaller than SE are filled [156]. Various shapes of SE can be used for modeling the resin-fiber bond. The effect of the shape of SE on the properties of the generated composite structure will be discussed in Chapter 7. To start the resin-fiber bond modeling, SE with the smallest size i.e., the mesh size is selected. The weight fraction of the binder in the generated composite structure is then calculated. If the target weight fraction is not met the filling procedure is conducted with a larger SE.

To develop a concentrated geometry generation and characterization toolbox both the PS model and binder impregnation model are developed in MATLAB software. The virtual fibrous bundle generated by PS model is converted into a 3D binary matrix that serves as an input for the binder impregnation model. Extraction of binary matrix from PS model is explained in Section 6.1. The Minkowski summation and erosion procedures are implemented using MATLAB image processing toolbox. Using the suggested procedure and assuming a disk shape SE the microstructure of Toray 060 carbon paper is generated as shown in Figure 5.19. As depicted in the figure the structure has a semi-layer-by-layer configuration that resembles an actual GDL.

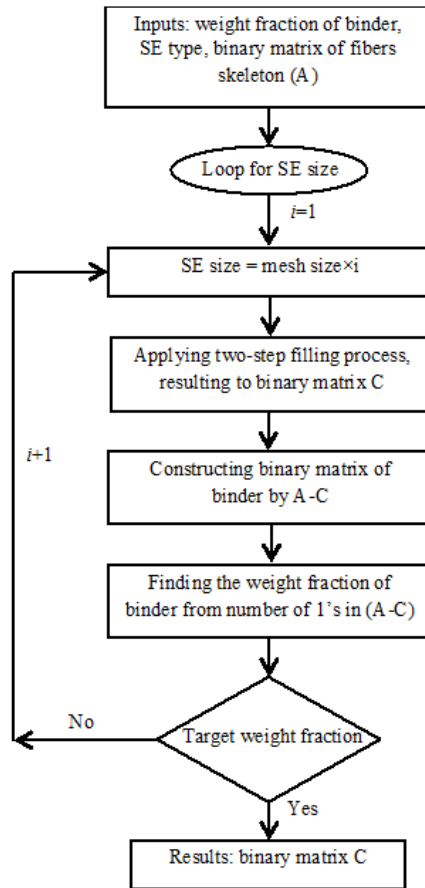


**Figure 5.17** Block diagram for generating a composite fibrous porous structure [156].

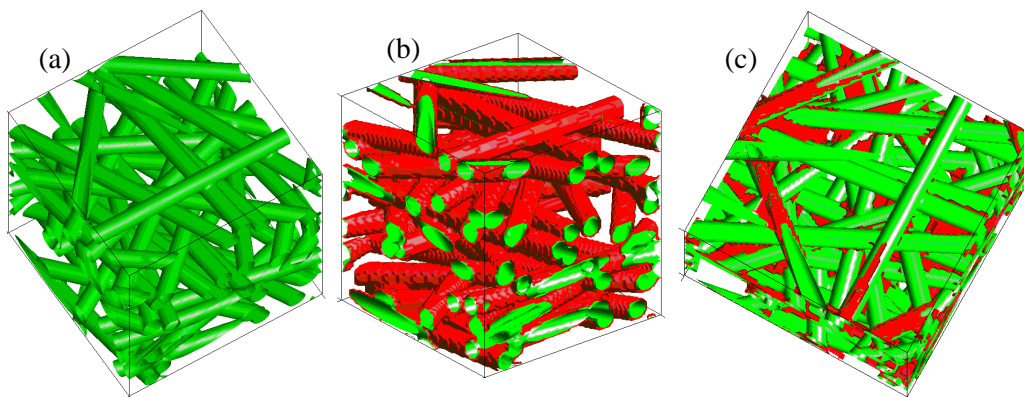


**Figure 5.18** (a) Fibrous matrix, (b) Minkowski summation with structure element, (c) Minkowski erosion with the same structure element [156].

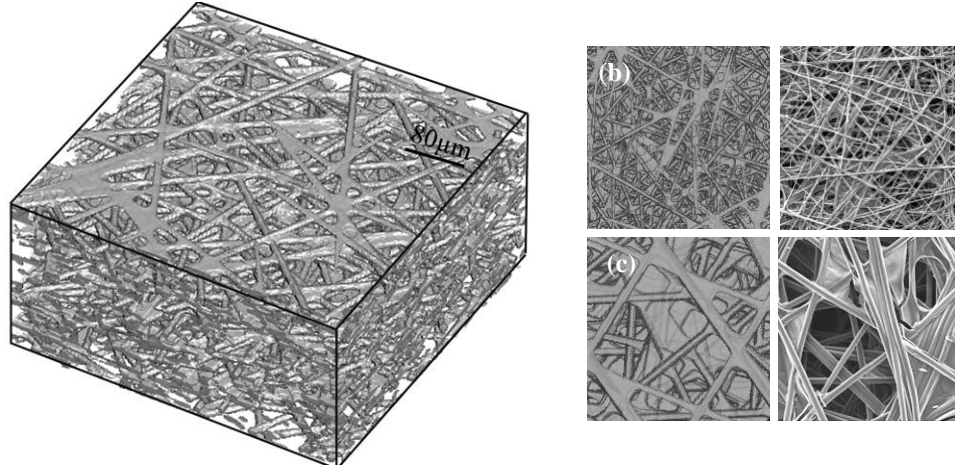


**Figure 5.19** (a) Isometric view of virtually constructed Toray 060 GDL, (b) and (c) cross sectional views, virtual GDL (left side) and SEM images (right side) [156].

## 5.5 Summary

In this chapter, the details of the modeling approach developed to generate various types of porous media such as carbon paper GDL, carbon felt GDL, carbon cloth GDL and composite carbon paper including the binder are presented. The generated structures are also shown and compared with SEM images of actual GDLs.

The implemented GA optimization technique for reducing the intersection of fibers in the RVE for both paper and felt GDLs is discussed in details. The effectiveness of the GA optimization is also discussed for different porosities.

An alternative modeling approach is introduced for felt media that takes into account the interaction of the forces exerted by the bent fibers to one another in the form of stored strain energy. Carbon felt GDL is reconstructed using this alternative approach.

The volume of intersections and the stored strain energy of the virtual felt GDL are computed and compared with the results from the virtual felt GDL generated using a geometrical modeling approach.

The Minkowski summation and erosion procedures are coupled with the PS model to generate composite porous media. The microstructure of Toray 060 carbon paper that has 27% weight fraction of binder is reconstructed by the proposed modeling method. The virtually constructed Toray 060 GDL is compared with its high resolution SEM images.

It is shown that fine detail geometrical representation of various types of fibrous porous media is feasible by implementing the proposed modeling technique. It is also shown that the generalized PS modeling technique can represent porous media with various structural properties such as different fibers profile, size, porosity, composite volume fractions, and thickness.

## **6. MORPHOLOGICAL CHARACTERIZATION OF FIBROUS POROUS MEDIA; METHODOLOGY**

To quantitatively characterize the shape of a porous structure and to optimally predict its bulk material properties, a set of morphological properties has to be determined. This set includes porosity, pore size, chord lengths and the shortest paths distributions, and the connectivity of the pores and the fraction of closed and open pores. Other than these properties, skeletonization of a porous structure has crucial importance. Using skeleton representation of a porous medium results in smaller volume of data and lower computational time for performing desired morphological operations. In this chapter, the numerical approaches taken to extract morphological properties of virtually generated porous structures are explained.

### **6.1 Extracting Binary Representation of Porous Media**

To couple the geometry generation procedure to the morphology and transport characterization procedures, the binary representation of a porous media is used. As shown schematically in Figure 6.1, the PS model divides the RVE into positive and negative regions. To find the binary matrix representation of a porous medium a grid is generated on the RVE. Then, the nodes of the grid that are located in the pore space are assigned a value of zero and the nodes in the solid phase to one. This reduces the RVE to a grid with nodes of one or zero. As shown schematically in Figure 6.2, the binary matrix is the matrix representation of this grid. To determine whether a node is in the solid phase or the pore space the procedure described in Figure 6.3 is implemented.



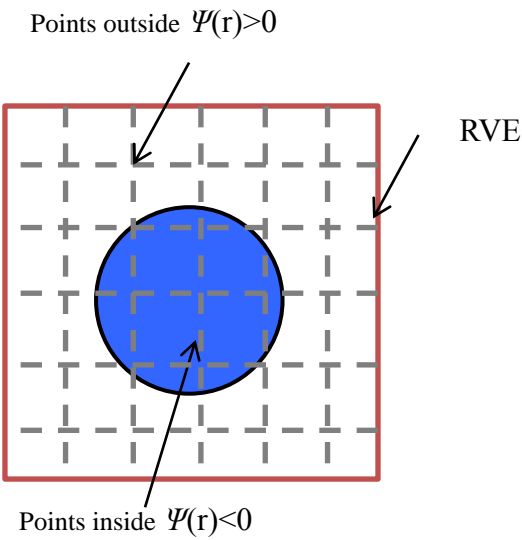


**Figure 6.1** Schematic of PS model and divided RVE.

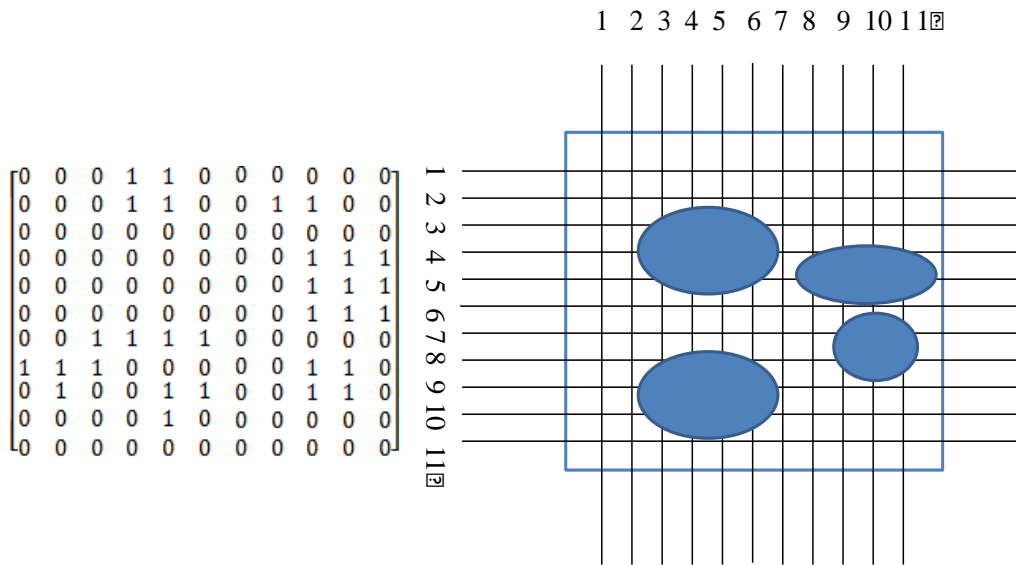


**Figure 6.2** Schematic of a porous medium and its binary representation.

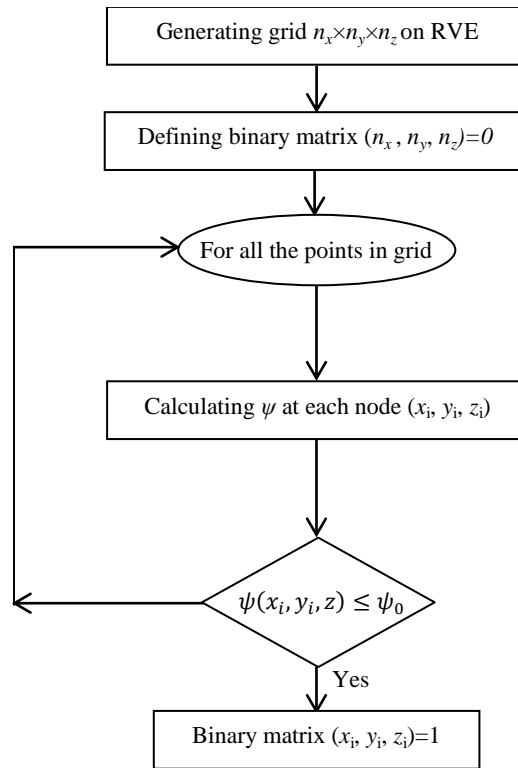


**Figure 6.3** Block diagram of generating the binary matrix.

## 6.2 Determining Porosity of Porous Media

Porosity is the ratio of the volume of pore space of a porous medium to its total volume. Using the binary matrix representative of a porous structure, its porosity is the ratio of the number of the zero elements of the binary representative matrix to the matrix size.

In a composite porous structure, three separate binary matrices are needed, for finding porosity of the whole structure, solid volume fraction of the fibrous skeleton and the binder. To find the solid volume fraction of each phase of the composite structure i.e., binder and fibers, the number of the elements of the corresponding binary matrix that are

equal to one are counted and then divided by the matrix size.

### **6.3 Determining Pore Size Distribution of Porous Media**

To determine the pore size distribution of a porous medium its binary representative matrix is used. It is assumed that all the elements of the binary matrix located in the pore space (set as zero) are the potential pore centers. Thus, for each of these elements the largest fitting sphere centered at the element is found. Then, the smaller spheres i.e., with centers located inside a larger sphere, are deleted. The outcome is a set of mutually overlapped spheres or pores, where none of their centers are located inside another pores, as shown schematically in Figure 6.4. A sphere is considered to fit if it has at least three points of contact that are not in the same direction with the surrounding solid surface. To determine if the sphere is touching the solid surface depending on its radius, a search algorithm is conducted on the neighboring elements.

To find a numerically computed pore size distribution that is closer to the pore size distribution found experimentally, the closed and dead end pores are discarded and not counted. Clearly in MIP method, closed pores do not contribute to the pore size distribution, because liquid cannot penetrate into the closed pores. Assuming that the liquid front is progressing in the through-plane direction, the pores that are counted in the pore size distribution are the pores that are accessible in the through-plane direction. The connectivity of the pores is found by searching the elements of the cross sections of the binary matrix that belongs to the neighboring of the pores. Thus, as shown in Figure 6.5 in the final count of pores, the dead end pores are discarded.

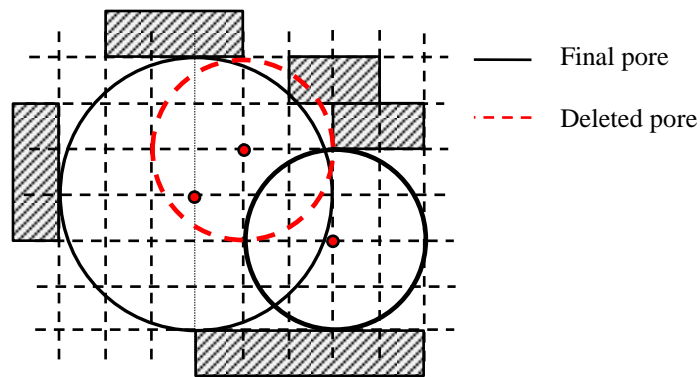


**Figure 6.4** The schematic of pore size fitting procedure, deleting the smaller pore located inside the bigger pore [156].

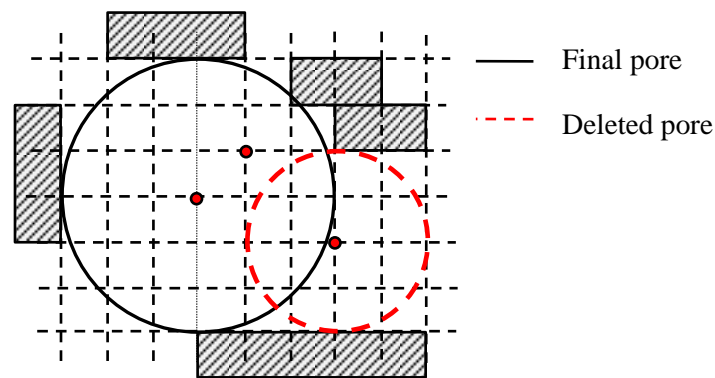


**Figure 6.5** The schematic of pore size fitting procedure, deleting the dead end pore [156].

#### 6.4 Determining Chord Length Distribution of Porous Media

Chord length ( $L_{ch}$ ) is defined as the distance between the internal solid boundaries in the pore and is a measure of the available free space in which the particles can move inside a porous structure. To find the chord lengths distribution, the cross sectional 2D binary matrices of the porous medium are extracted from the 3D binary matrix. The

chord length is the number of the consecutive 0's in a principal direction multiplied by the mesh size.

## **6.5 Determining the Shortest Paths Distribution of Porous Media**

The set of the shortest paths of a porous medium is a set of paths inside the porous medium, which have the shortest distances for traveling from on side of the medium to the other side.

Flow can travel from one side of the porous medium to the other side through different paths, as shown schematically in Figure 6.6. However, as the length of the path increases the probability of encountering an obstacle will increase. Thus, knowing the distribution of the shortest paths can be greatly helpful for a deeper understanding of the transport phenomena in a porous medium.

To find the distribution of the shortest paths inside the porous structure Dijkstra's algorithm is modified for higher accuracy and is used in this study [93]. The suggested algorithm is capable of calculating the shortest paths starting from each pore and finding the number of that shortest path for each pore. Knowing the distribution and amount of the shortest paths, the average geometrical tortuosity can be defined as a weighted function based on the number of paths from each specific vertex (or source).

To implement Dijkstra's algorithm a graph representation of the porous domain is extracted from the binary matrix, as shown schematically in Figure 6.6. To construct the

graph representation of a porous medium, first it is assumed that there is no solid phase (fibers, or fiber plus binder) in the RVE, and a grid of  $n_x \times n_y \times n_z$  called  $G$  is generated for RVE.  $G$  is considered as a graph that shows the connectivity of nodes inside the RVE. Any points of  $G$  at position  $(i,j,k)$  where  $0 \leq i \leq n_x$ ,  $0 \leq j \leq n_y$ , and  $0 \leq k \leq n_z$  is a vertex of  $G$ . To construct edges of  $G$ , the connectivity of the vertices are determined. Two vertices  $(i,j,k)$  and  $(a,b,c)$  are assumed to be connected if and only if  $|i-a|+|j-b|+|k-c|=1$ .

Graph  $G$  is then modified to account for the effect of the solid phase in the RVE. The solid phase acts as an edge eliminator or vertex eliminator (or both). Using 3D binary matrix, it is determined whether a vertex belongs to the void space, or the solid phase, and then the vertex or the corresponding edges in  $G$  are deleted. Graph  $G$  is in fact a weighted graph where weight of each edge is exactly 1. It is assumed that all the vertices in the inlet and outlet are in the pore space and that the sides of the RVE are in the solid space. For each vertex at the inlet, the modified version of Dijkstra's algorithm is run and the length of the shortest path and the number of the shortest path from that vertex to every other vertex in outlet are found.

To reduce the required computational time of finding the shortest paths distribution, the same structure as graph  $G$  is constructed in the computer memory and processes are carried on that structure. This results in a faster algorithm compared to the typical ways of representing a graph with adjacency matrix. The program is written in C++ MEX format to develop a concentrated morphological characterization procedure.

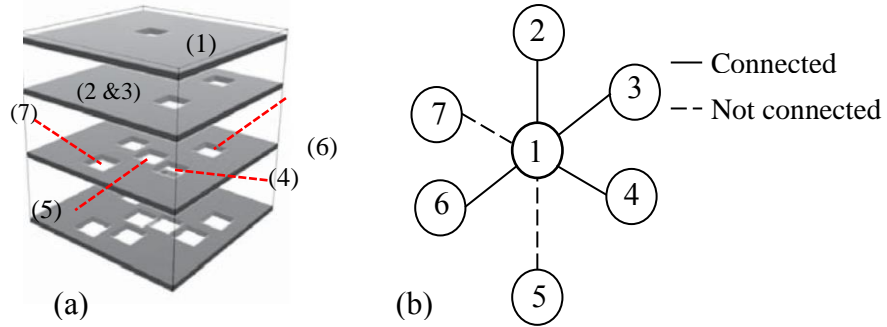


**Figure 6.6** (a) Hypothetical structure, (b) the graph representation of the porous domain to find the shortest paths from the bottom surface to the top surface [92].

## 6.6 Skeletonization of porous medium

One of the main advantages of finding the skeleton of a porous media is the reduction of the data for post processing. As shown schematically in Figure 6.7, in a skeleton representation of a porous medium only the edges or the centerlines of the porous space remain in the domain.

In this study the edges of the porous structure are detected using the binary matrix, simply by detecting the consecutive zeros in the 2D binary stacks of the porous media. By sweeping the 2D matrix, the corresponding location of the first 1 that is encountered is saved to form an edge that has only one voxel (or mesh) thickness. Finding all the edges, the centerlines are then found by determining the location of the points that have the same distance from the edges.

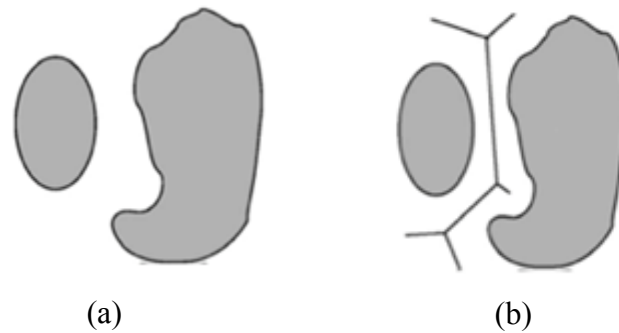


**Figure 6.7** A 2D schematic of Skeletonization of porous media, (a) top view of a porous medium, (b) skeletonized pore space [75] .

## 6.7 Summary

The existing numerical schemes for finding the morphological properties of porous media offer useful platforms and tools for evaluation of some morphological properties, but are computationally expensive. In the current study, these schemes are modified for higher accuracy and lower computational time. In addition, the geometry generation is automatically linked to the morphology characterization, which can be used for design purposes and also as a characterization tool.

The developed numerical methods for calculating the morphological properties of the porous media i.e., porosity, pore size distribution, chord lengths and the shortest paths distributions, are explained and the skeletonization of a porous medium using its binary matrix is described.



## **7. MORPHOLOGICAL CHARACTERIZATION OF FIBROUS POROUS MEDIA, RESULTS**

### **7.1 Determining Morphological Properties of Carbon Paper GDL**

After generating the microstructure of Toray 060 carbon paper, its pore size, chord lengths and shortest paths distribution are found using the procedures described in Chapter 6. The resulting pore size distribution is shown in Figure 7.1. The average pore sizes for the virtual Toray 060 GDL is found to be 19  $\mu\text{m}$ , that is close to the average pore size of 18  $\mu\text{m}$  measured by Fluckiger et al. [27] . They measured the average pore size of Toray 060 GDL using MIP as shown in Figure 7.2. As illustrated in Figure 7.1, excluding the dead end pores and considering the connected pores in the through-plane direction results into a pore size distribution that resembles the pore size distribution found by MIP.

The chord lengths distributions for through-plane and in-plane directions of Toray 060 GDL are shown in Figures 7.3 and 7.4. As depicted in the figures, in the in-plane direction the chord lengths are distributed in a wider range. In the through-plane direction the chord lengths are smaller due to the semi-layered structure of the GDL.

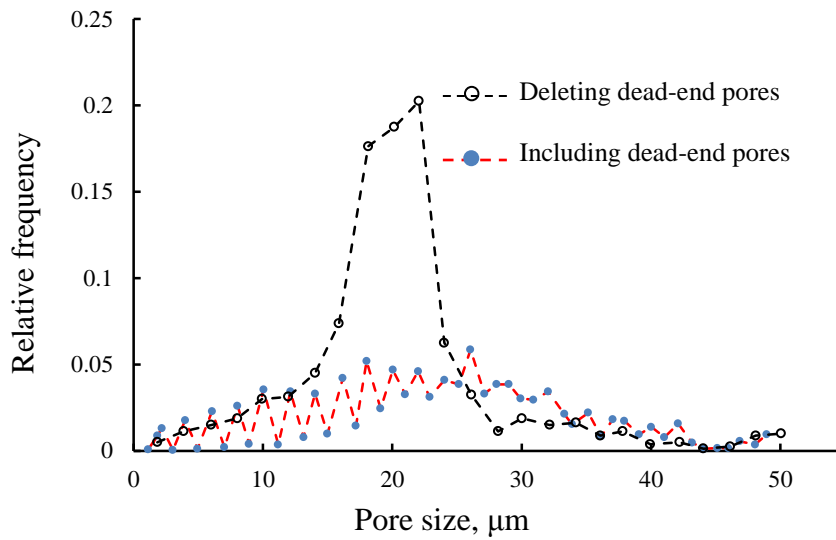


**Figure 7.1** Numerical pore size distribution of virtual Toray 060 GDL [156].

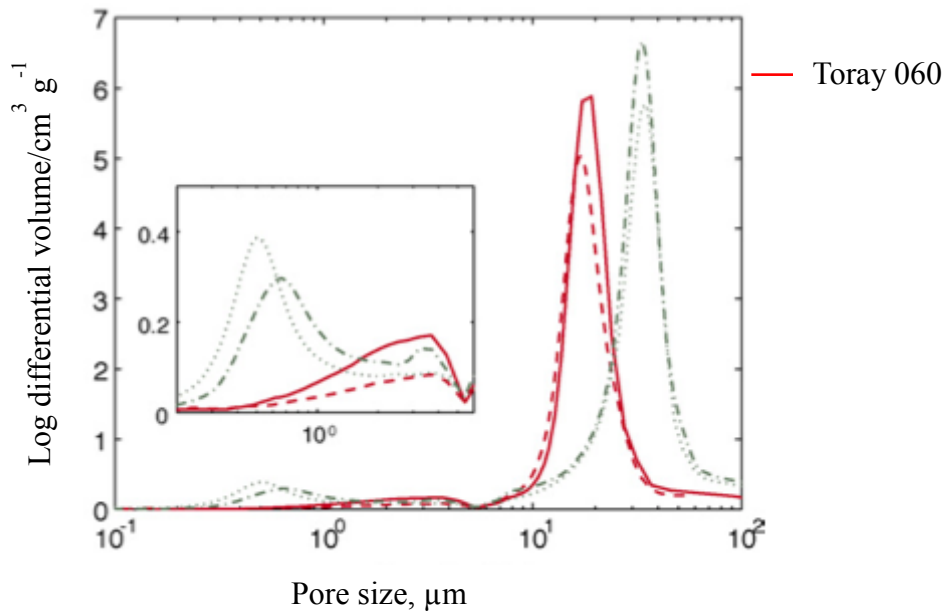


**Figure 7.2** MIP pore size distribution of Toray 060 GDL [27].

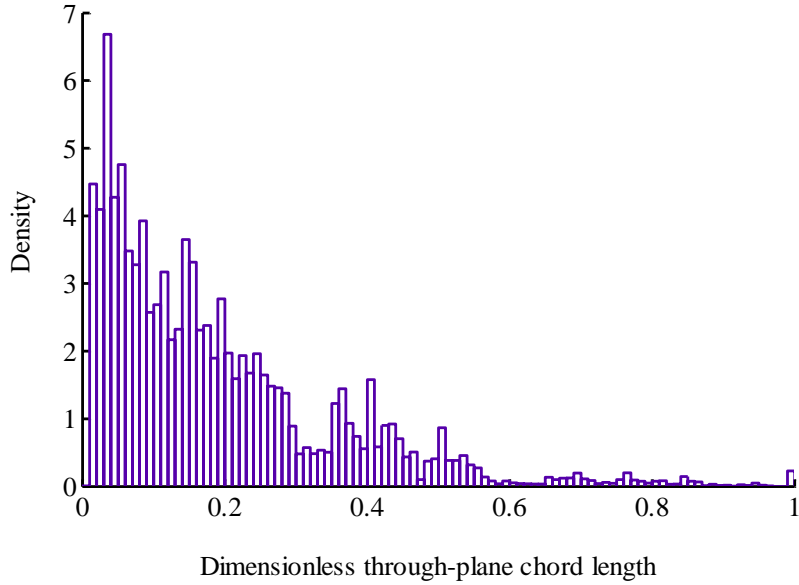


**Figure 7.3** Through-plane chord lengths distribution for virtual Toray 060 GDL [156].

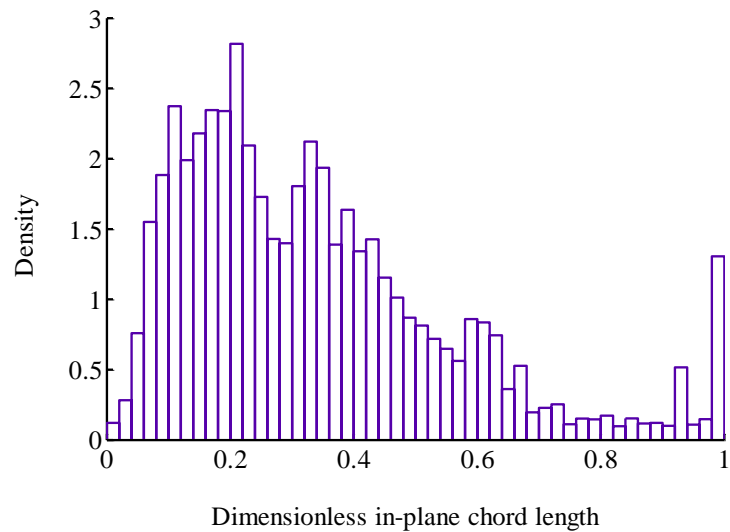


**Figure 7.4** In-plane chord lengths distribution for virtual Toray 060 GDL [156].

The distributions of shortest paths inside Toray 060 GDL for the through-plane and in-plane directions are shown in Figure 7.5. The distribution of the shortest paths in the through-plane and in-plane directions agrees well with experimentally determined

values [75]. As expected, due the semi-layer structure of the GDL, the shortest paths are longer in the through-plane direction.

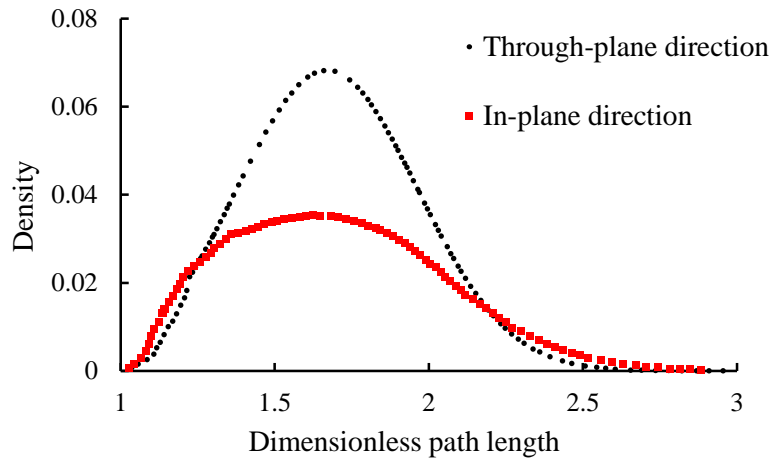


**Figure 7.5** Distribution of the shortest paths inside the pore space of Toray 060 GDL

[156].

## 7.2 Effect of Binder Modeling on the Characteristics of a Composite GDL

As mentioned in Chapter 5.4, the impregnated binder in the composite structures is modeled by implementing Minkowski summation and erosion of the fibrous skeleton by a filler SE. SE is a binary matrix with an arbitrary shape and size. Thus, two-dimensional (flat) SE with disk or octagonal shapes, or three-dimensional (non-flat) SEs with spherical or cubical shapes can be used for virtual construction of binder. To determine the SE that can accurately represent the composite fibrous structure, a disk shape SE (2D) and a cubical SE (3D) are used to construct the microstructure of Toray 060 GDL and the morphological and transport properties of both microstructures are found.

As shown in Figure 7.6, the pore size cumulative probability distributions for both structures are almost the same. However, as illustrated in Figure 7.7, the pore size distribution for the two microstructures are different and the distribution corresponding to a 2D SE shows higher resemblance to the pore size distribution found from experimental tests, which is shown in Figure 7.2.

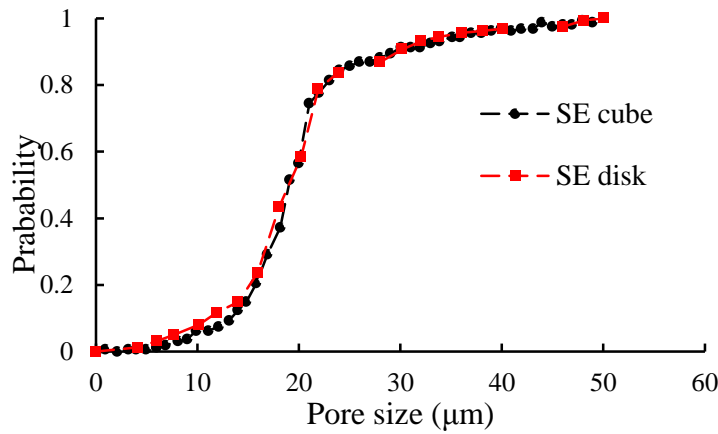


**Figure 7.6** Pore size cumulative probability distribution for Toray 060 GDL modeled with different structure elements [156].

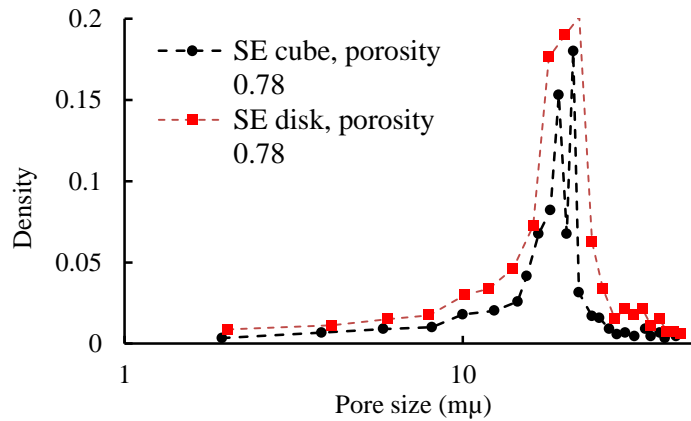


**Figure 7.7** Pore size distribution for Toray 060 GDL modeled with different structure elements [156].

Distribution of the shortest paths in the through-plane and in-plane directions are

found and presented in Figure 7.8. As illustrated, the GDL generated using the disk SE has inhomogeneous topology as expected for GDLs due to their semi-layered structure. But, the distribution of the paths in the through-plane and in-plane directions of the microstructure generated using a cubical 3D SE, is approximately the same. Thiedmann et al. [75] found the through-plane shortest paths distribution of Toray GDL as shown in Figure 7.9, from a virtual representation of the GDL generated by the imaging techniques. As shown in Figure 7.8, the through-plane shortest paths distribution found from the virtual Toray 060 GDL generated by a disk SE is close to the results based on the image of the actual Toray GDL.

The average chord lengths of the structure using a 2D SE and a 3D SE in the in-plane and through-plane directions are 46, 20, 40 and 26  $\mu\text{m}$ , respectively. Using a 3D SE results in uniform distribution of binder in the through-plane and in-plane directions. Thus, generating a composite media that might not have a semi-layered structure, which is an inherent property of carbon paper GDLs. As such using a 3D SE is not considered feasible. Due to the semi-layered structure of carbon paper GDL, the 2D disk SE is selected as the best filler for virtual representation of impregnated binder in the GDL.

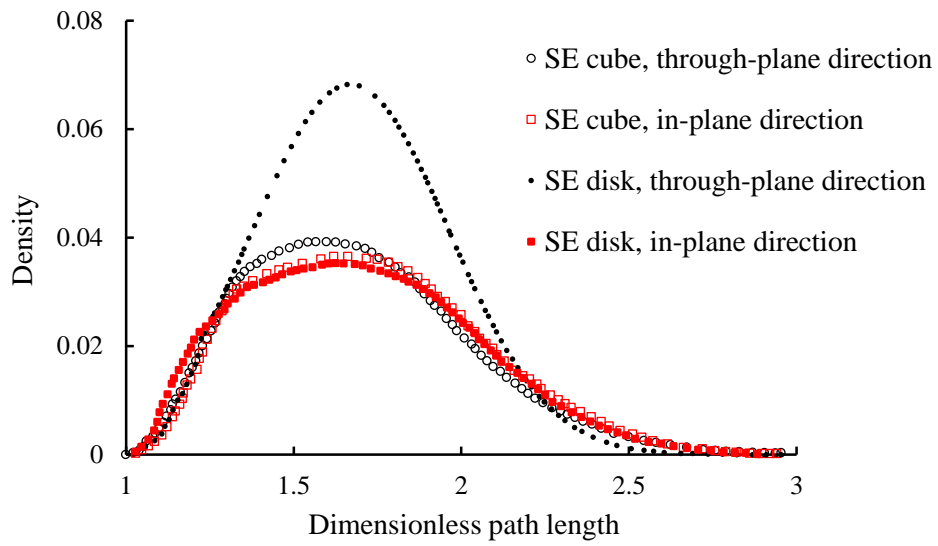


**Figure 7.8** The shortest paths distribution for Toray 060 GDL modeled with different SEs [156].

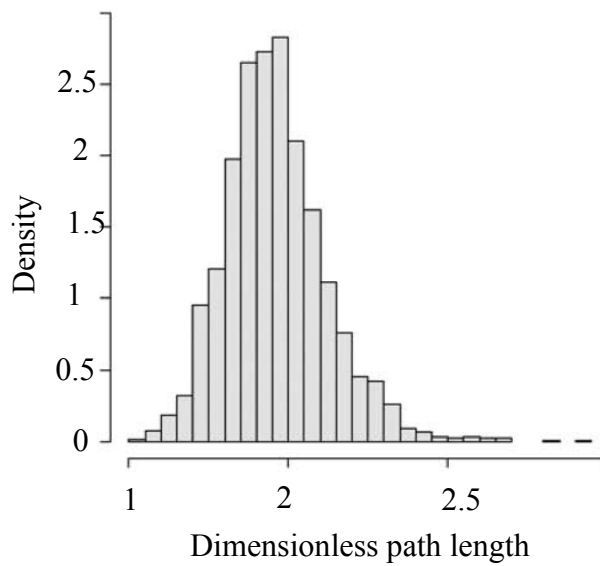


**Figure 7.9** The through-plane shortest paths distribution for Toray GDL [75].

### 7.3. Effect of Binder Volume Fraction on the Morphological Properties of the GDL

To study the effects of binder quantity on the morphological and transport properties of the composite media, the volume fraction of binder in the GDL is changed from 10% to 65% while keeping the solid volume fraction of the fibrous bundle constant and equal to 16%.

As shown in Figure 7.10, utilizing higher amount of binder in the structure results in smaller pores. To study the inhomogeneity of the composite structures under various binder loadings, the chord lengths distributions for the three principal directions are found and the change in the average value of chord lengths is plotted in Figure 7.11. As shown, the average chord length in the in-plane direction slightly increases with increasing binder, while the through-plane direction chord lengths sharply decrease. Although the reduction of the free space in the porous structure with increase of binder volume fraction can be determined from the pore size distribution, the directionality of the variation in the porous structure cannot. Thus, the pore size distribution data provides little knowledge regarding the complex and inhomogeneous structure of the GDL. The presented results indicate the importance of conducting directional morphological analysis for a complex composite fibrous microstructure.

The cumulative probability distributions of the shortest paths for through-plane and in-plane directions under different binder loading are found and shown in Figures 7.12 and 7.13. As illustrated in the figures, utilizing a higher amount of binder in the structure results in longer paths, although the change in the through-plane direction is larger compared to the in-plane direction. As shown in Figure 7.11, the average through-plane chord length decreases as the binder volume fraction increases, resulting to the



higher blockage of the available paths inside the porous structure, thus longer paths.

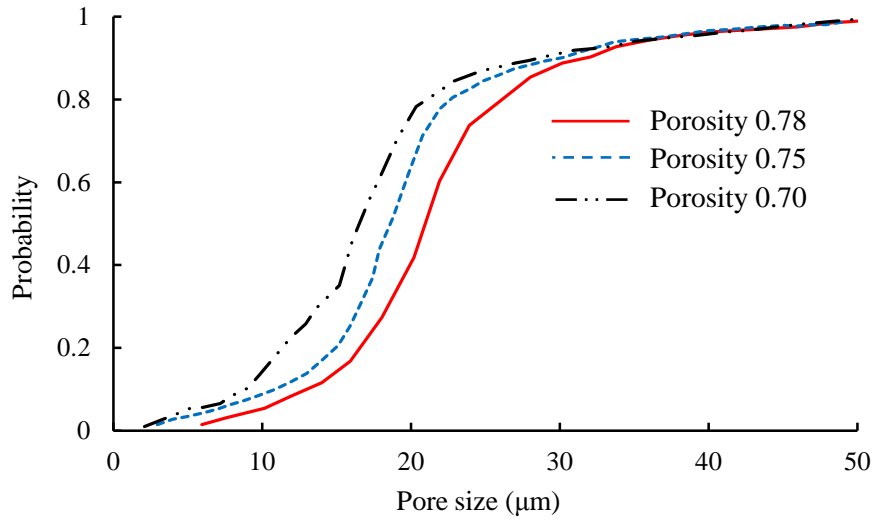


**Figure 7.10** Effect of volume fraction of binder in GDL's structure on the pore size cumulative probability distribution [156].

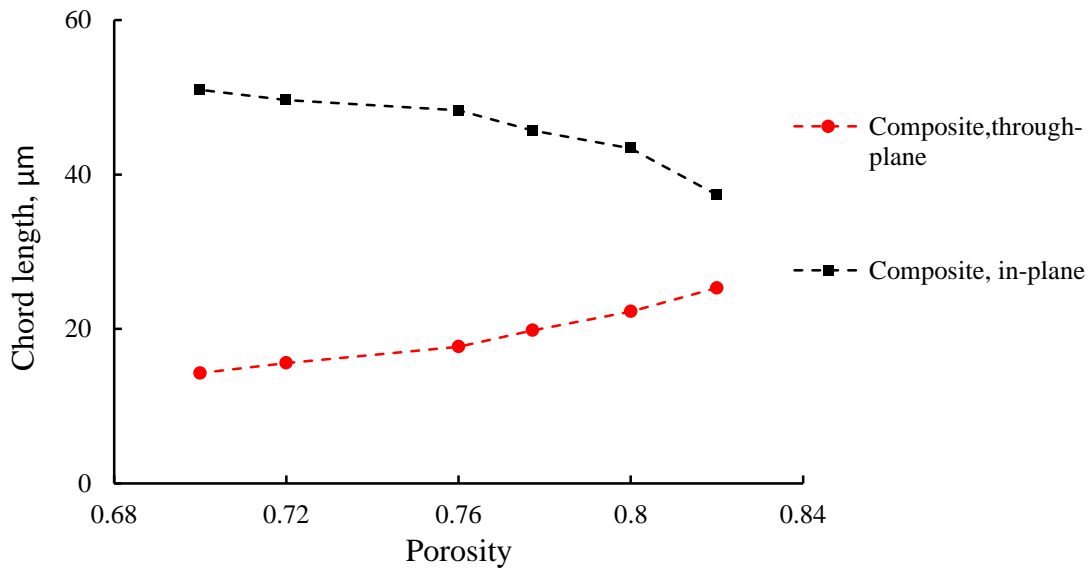


**Figure 7.11** Effect of volume fraction of binder in the GDL's structure on the average chord length [156].

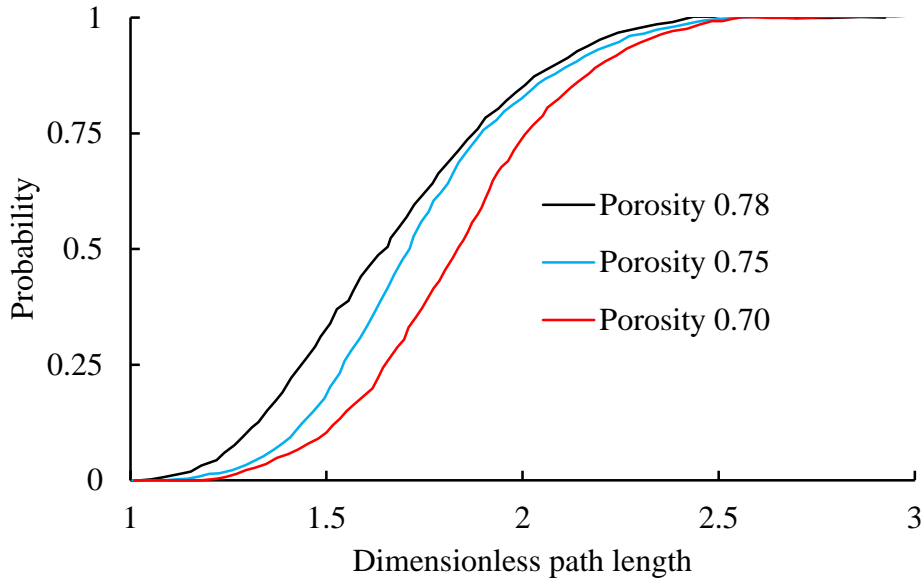


**Figure 7.12** Effect of volume fraction of binder on the through-plane cumulative probability distribution of the shortest paths.

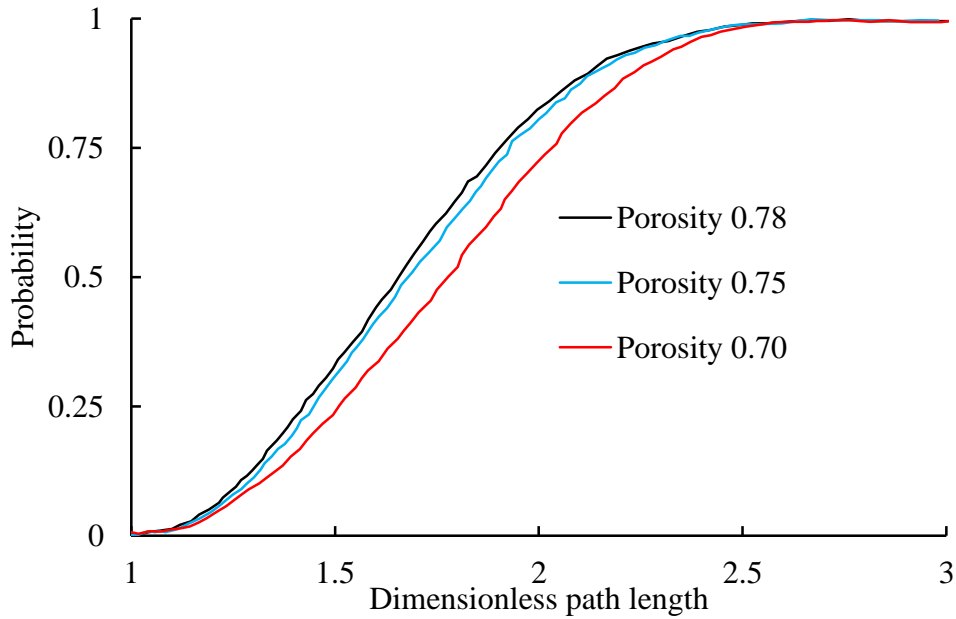


**Figure 7.13** Effect of volume fraction of binder on the in-plane cumulative probability distribution of the shortest paths.

#### **7.4 Determining Morphological Properties of Felt GDL**

Using the geometrical modeling and the energy coupled modeling approaches the microstructure of Freudenberg H2315 felt GDL is constructed. The average chord lengths for the through-plane and in-plane directions of these two structures are given in Table 7.1. As presented in the table, the average chord lengths of the microstructure generated by the energy coupled modeling approach are larger than the average chord lengths of the microstructure generated by the geometrical modeling approach. This is due to the large curvature of fibers in the microstructure generated by the geometrical modeling approach.

The shortest paths distribution in the through-plane and in-plane directions of the microstructures generated by the geometrical modeling and the energy coupled modeling approaches is found and negligible difference between their shortest paths distribution was observed. The distribution of the shortest paths of virtually constructed Freudenberg H2315 felt GDL is shown in Figure 7.14. Gaiselmann et al.[81] found the through-plane shortest paths distribution of felt GDL, as shown in Figure 7.15, from a virtual representation of the GDL generated by the imaging techniques. As shown in Figure 7.15, the through-plane shortest paths distribution found from the virtual felt GDL generated by the generalized PS model is close to the results based on the image of an actual felt GDL.

The pore size distribution of the felt microstructure generated by the energy coupled modeling approach is shown in Figure 7.16. The average pore sizes for the felt

structure is 19  $\mu\text{m}$ , which is close to the experimentally found data of 17 $\mu\text{m}$  [37, 81]. The average pore size of felt and paper GDLs are close to each other, but as shown in Figure 7.17, the pores of felt structure are slightly smaller.

**Table 7.1** The average chord lengths of felt GDL generated by the geometrical and energy coupled modeling approaches.

Modeling approach	$L_{ch, xx}$ ( $\mu\text{m}$ )	$L_{ch, yy}$ ( $\mu\text{m}$ )	$L_{ch, zz}$ ( $\mu\text{m}$ )
Energy coupled modeling	29	30	23
Geometrical modeling	25	26	21

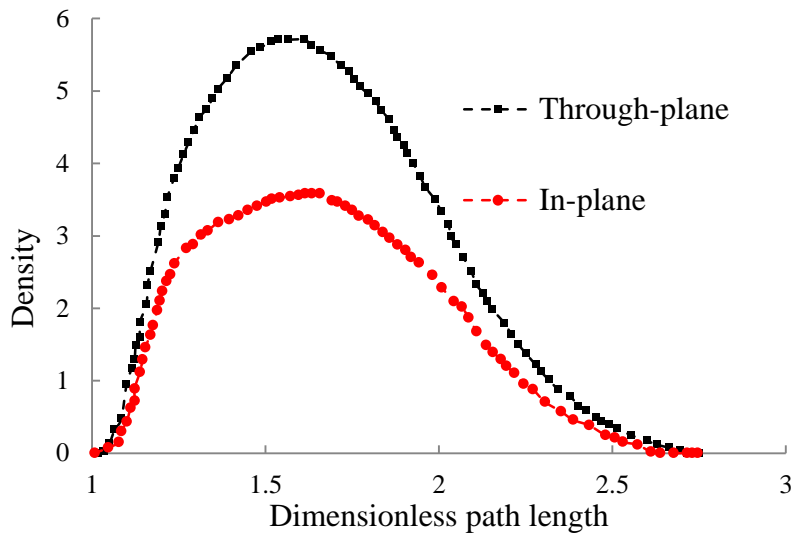


**Figure 7.14** Distribution of the shortest paths of virtually constructed Freudenberg H2315 felt GDL.

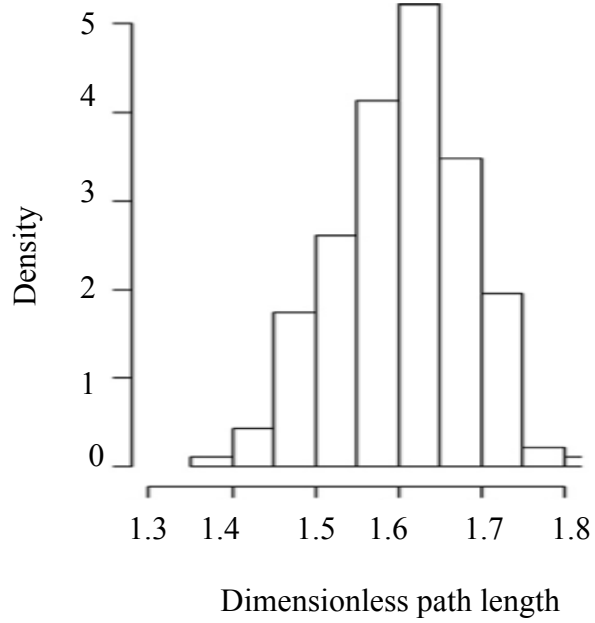


**Figure 7.15** The through-plane shortest paths distribution of felt GDL [81].

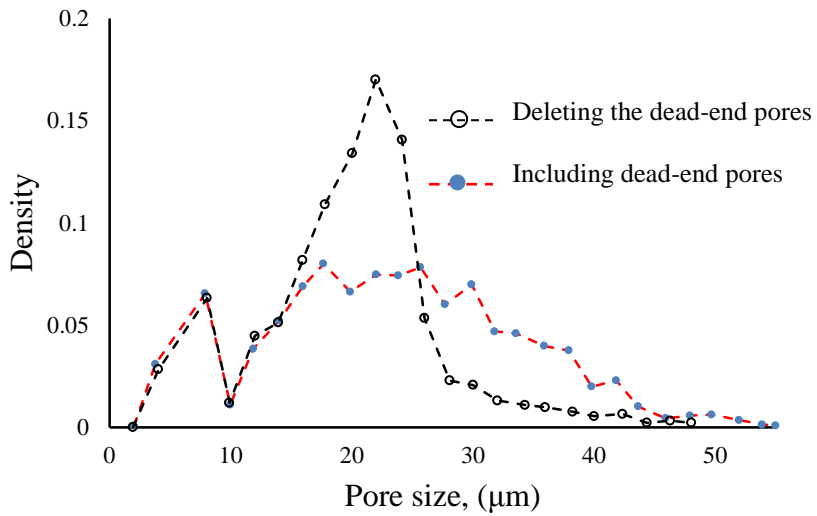


**Figure 7.16** Pore size distribution of virtually constructed Freudenberg H2315 felt GDL.

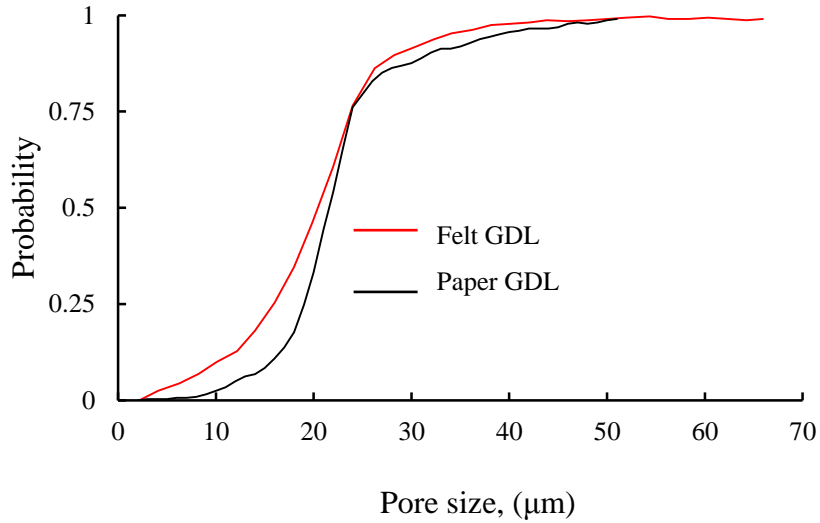


**Figure 7.17** Effect of a GDL structure on the pore size cumulative probability distribution.

To study the effect of porosity of the felt media on their structural properties, the average chord lengths of the felt microstructures for through-plane and in-plane directions are found and shown in Figure 7.18. As illustrated in the figure, the average chord length decreases as the porosity decreases for both in-plane and through-plane directions regardless of the method implemented for generating the felt microstructures. However, microstructures that are generated by the geometrical modeling approach have smaller chord lengths than the microstructures generated by the energy coupled modeling approach.

The cumulative probability distributions of the shortest paths for through-plane and in-plane directions for porosity of 0.70 and 0.78 are found and shown in Figures 7.19 and 7.20. As illustrated in the figures, decreasing the porosity results in longer paths for both through-plane and in-plane directions. As shown in Figure 7.18, the average chord length decreases as porosity decreases, resulting to a higher blockage of the available

paths inside the porous structure. However, in felt structures the shortest paths are not as sensitive to the porosity compared to composite structures. As illustrated in Figures 7.19 and 7.20, in felt structures the shortest paths in the through-plane and in-plane directions show the same degree of sensitivity to the change of porosity, while in the composite media higher sensitivity was observed in the through-plane direction.

Implementing the geometrical modeling and the energy coupled modeling approaches do not have significant effect on the shortest paths distribution of the generated felt structure, but as shown in Figure 7.18, the chord lengths of the structures are different. The effect of the implemented modeling approach on the transported properties of the felt media will be discussed in Chapter 9. Then, the proper modeling approach will be selected.

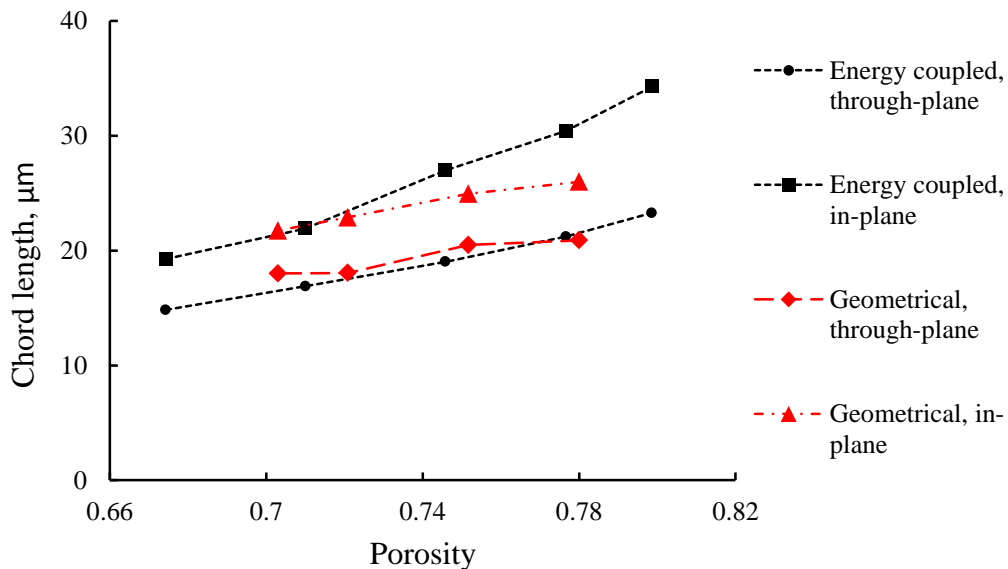


**Figure 7.18** Effect of porosity of felt GDL on the average chord lengths.

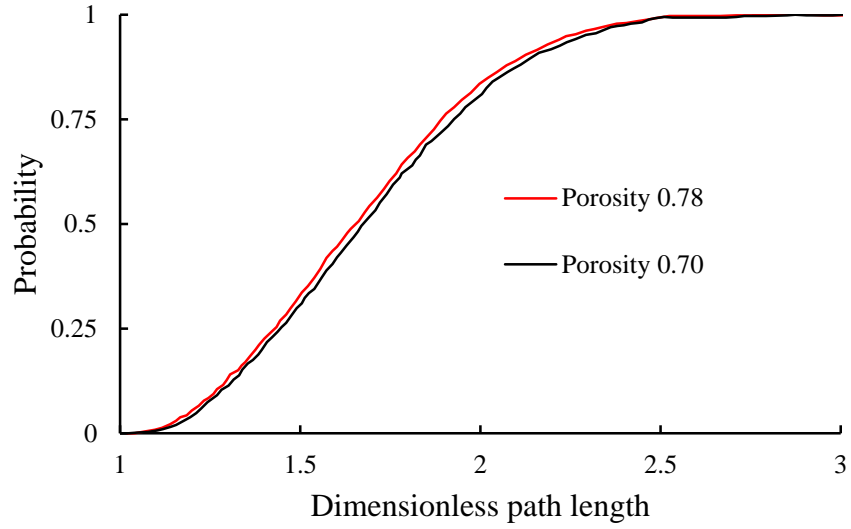


**Figure 7.19** Effect of porosity of felt GDL on the through-plane cumulative probability distribution of the shortest paths.

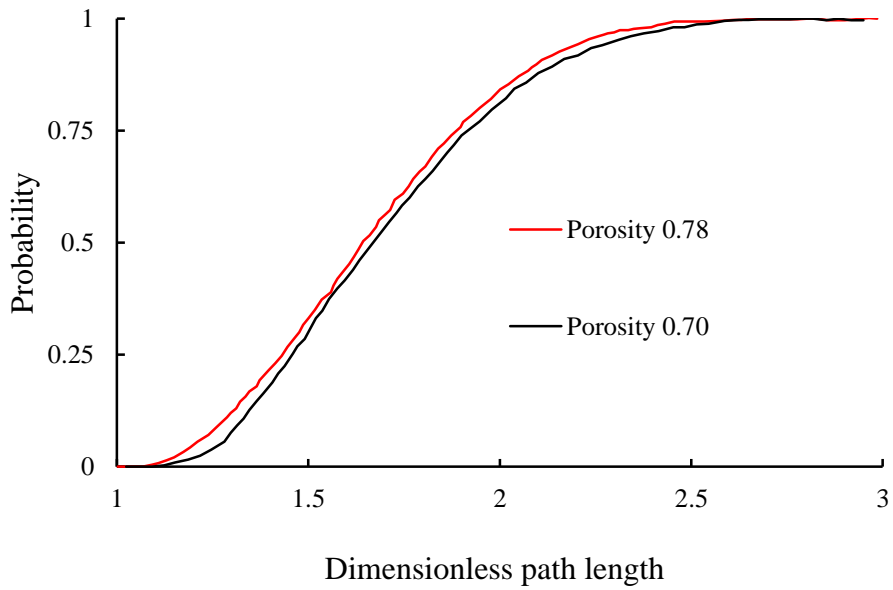


**Figure 7.20** Effect of porosity of felt GDL on the in-plane cumulative probability distribution of the shortest paths.

### 7.5 Summary

In this chapter, the morphological properties of Toray carbon paper GDL and



H2315 felt GDL are found. The pore size distributions of both GDLs are verified against the experimentally measured data. The importance of fine-detailed geometrical modeling is illustrated by showing the effect of the implemented modeling technique for representing the impregnated binder in the composite microstructures on the predicted morphological properties. It is shown that to model composite porous media with layered structures using a 3D structure element results in a porous structure that does not have a layer-by-layer topology. Thus, for an accurate representation of the impregnated binder in the composite porous structures a 2D structure element is suggested.

The effects of binder volume fraction on the morphological properties of composite paper media are studied. It is found that increasing the binder volume fraction reduces the pore size of the composite porous media. The average chord length of the composite structures under different loading of binder is computed for 3 principal directions. It is found that the pore space of composite media shows different dependency upon the volume fraction of the binder in the through-plane and in-plane directions. The chord length in the in-plane direction is not sensitive to binder loading, while in the through-plane direction the chord length reduces largely by increasing the volume fraction of the binder. The directionality of the pore space of composite porous media shows the necessity of conducting the chord length analysis for a better understanding of their topology.

The morphological properties of felt structures generated by both geometrical modeling and energy coupled modeling approaches are determined. It is found that the chord lengths distribution of the structures is sensitive to the implemented modeling

approach. However, it is found that the shortest paths distribution of the generated microstructures by the energy coupled modeling and the geometrical modeling approaches are similar. Assuming that transport and morphological properties are related, for selecting the proper modeling approach the transport properties of the virtual structures need to be determined. In Chapter 9, the transport properties of the virtual microstructures will be determined and the accuracy of the implemented modeling approaches will be discussed.

## **8. TRANSPORT PROPERTIES OF FIBROUS POROUS MEDIA, METHODOLOGY**

In this chapter the transport properties of a porous medium i.e., permeability, tortuosity and diffusivity are introduced and the utilized methods for computing these properties are described. To be suitable for the design purposes the transport property characterization procedure is dynamically linked to the PS modeling program. The coupling is accomplished by implementing an automated mesh generation procedure. Although the transport properties of porous media have been computed from their geometrical representations, the generated microstructures were simplified and the effect of the composite structure, the fibers' profile and curvature, have been neglected. Thus, in this chapter the methods to calculate the transport properties of the structures with complex structure such as composite media are introduced.

### **8.1 Mesh Generation for Computational Fluid Dynamic Simulations**

For the geometries that are constructed by conventional CAD tools e.g., straight-line segments, B-spline and non-uniform rational B-spline (NURBS), the available mesh generation software packages, such as GAMBIT and ICM CFD can be used for generating the volumetric mesh. However, for complex porous structures, conventional CAD software packages are not efficient.

In this study three methods for constructing the volumetric mesh representation of the computational domain are suggested. The first method corresponds to geometries

where a pre-dominant axis can describe their topology, such as fibrous bundle of a carbon paper. The pre-dominant axis of the constructed geometries is extracted from PS model and then the whole structure is regenerated using CAD software. Using GAMBIT, software the volumetric mesh of the microstructure is generated. For the complex porous structures two procedures are suggested, one is using the surface mesh and the other approach is using voxel representation of the porous medium to generate a volumetric mesh of the computational domain. The procedures to generate the mesh, and their advantages and disadvantages are discussed in this chapter.

### ***8.1.1 Generating Volumetric Mesh for Geometries with Pre-Dominant Axes***

For the geometries where a predominant axis represents the elements in the structure e.g., fibrous matrix of carbon paper, the volumetric mesh representation of the computational domain is generated in GAMBIT. A MATLAB script is developed to links the PS model to GAMBIT by defining the script commands of GAMBIT software as MATLAB's scripts. Because GAMBIT is fully scriptable in journal format this method is a very efficient automated procedure for generating the microstructures with different characteristics such as porosity, fiber's size and orientation, which is very suitable for the design purpose. The developed code automatically build the structure in GAMBIT, then the unstructured volumetric mesh is generated [4]. To generate the volumetric mesh for the GDLs that are composed of straight fibers, the microstructure is reconstructed GAMBIT by using the information of its dominant axis. To locate a fiber in 3D space a point on its axis and the axis' vector needs to be known. A center point on the cross

section of each fiber and the components of its axis vector are calculated and stored. This data collection serves as inputs for the script.

In Figures 8.1 and 8.2, a typical example of a reconstructed fibrous GDL and the unstructured volumetric mesh of the domain, which are generated by implementing the described procedure are shown. For other types of porous structures such as felt media when the curvature of bending is not too large this method can be applicable. In Figure 8.3 the reconstructed microstructure of a typical felt media and its unstructured volumetric mesh are presented. However, this procedure is limited to porous structures that have bent fibers; where the fiber curvature cannot be excessive. Although the suggested method is easy to implement and versatile to model various fibrous GDLs efficiently, is it limited to the porous media with a dominant axes. This limitation warrants the need to develop alternative approaches that can generate volumetric mesh representation of porous media with higher accuracy.

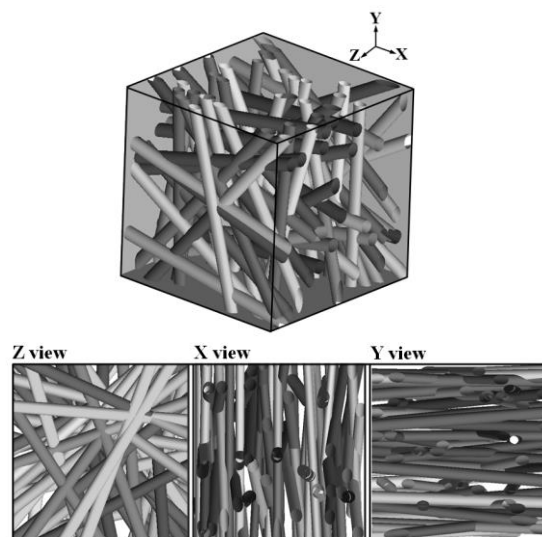


**Figure 8.1** 3D reconstructed of the GDL and 2D views from z, x and y directions [4].

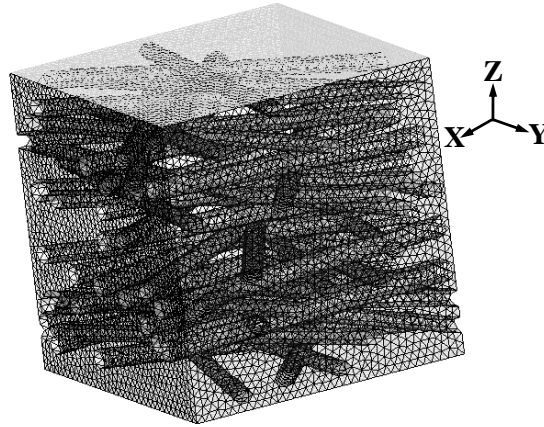


**Figure 8.2** Illustration of the tetrahedral mesh for straight fibers bundle in paper GDL [152].

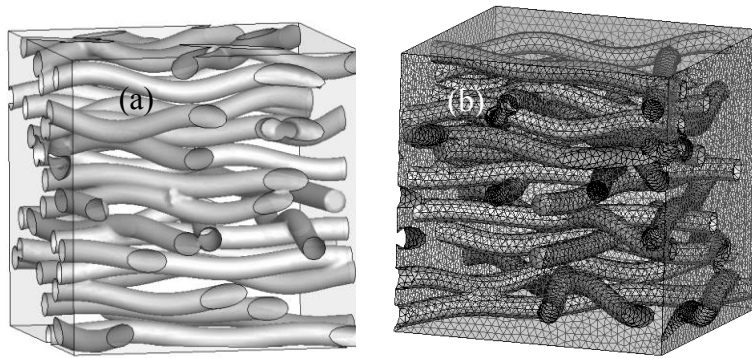


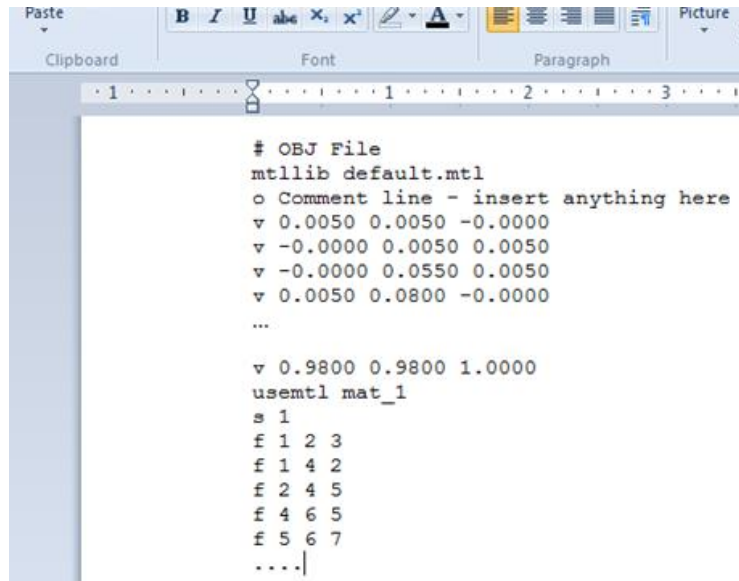
**Figure 8.3** Felt structure with one cosine term (a) geometric model, (b) unstructured volumetric mesh [152].

### ***8.1.2 Generating Surface Mesh for Complex Geometries***

For complex geometries i.e., the composite structures, the volumetric mesh can be generated from the surface mesh. In addition to generating a volumetric mesh for CFD analysis, extracting a surface mesh can be used for other purposes, such as representing constructed geometries or extracting a Voronoi diagram of a porous structure.

To extract the surface mesh from the PS model, MATLAB computational geometry package is used, which generates the triangular surface mesh based on the Delaunay mesh generation algorithm. The coordinates of the triangular nodes and their connectivity are found by MATLAB software.

Having the triangular surface mesh of the domain, an object file in text format as shown in Figure 8.4, is created by MATLAB script. Then, the text file is converted to an object format by saving it as a .obj file. The object file is imported into open source software called Wings3D software, which converts the .obj format to .stl. This conversion is necessary because, the generated .stl file is recognized by conventional mesh generation softwares such as ICEM CFD.



```
# OBJ File
mtllib default.mtl
o Comment line - insert anything here
v 0.0050 0.0050 -0.0000
v -0.0000 0.0050 0.0050
v -0.0000 0.0550 0.0050
v 0.0050 0.0800 -0.0000
...
v 0.9800 0.9800 1.0000
usemtl mat_1
s 1
f 1 2 3
f 1 4 2
f 2 4 5
f 4 6 5
f 5 6 7
...|
```

**Figure 8.4** The object file of triangular surface mesh of the RVE.

In ICEM CFD, the stl will be converted to the volumetric mesh and then the boundary conditions for the CFD simulations are applied. The final volumetric mesh representative of a paper GDL is shown in Figure 8.5.

Although this method is capable of generating the volumetric mesh for the porous media with highly complex structures, the quality of the volumetric mesh depends on the quality of the extracted surface mesh. In some cases, the refinement of a surface meshes is time consuming.

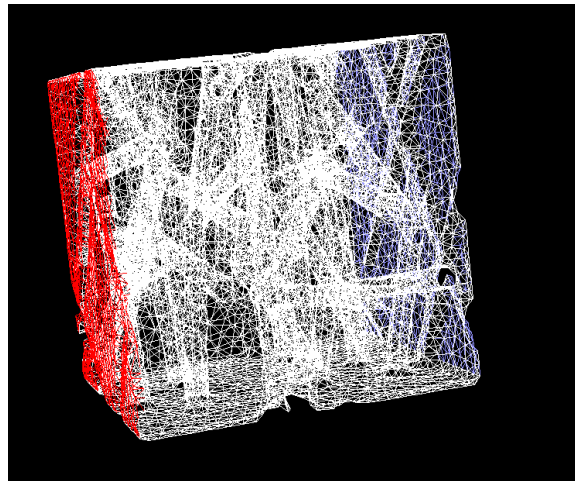


**Figure 8.5** Volumetric mesh generated for a paper GDL from the surface mesh.

### ***8.1.3 Generating Volumetric Mesh for Complex Geometries***

For complex geometries i.e., a composite structure, the volumetric mesh is generated based on the voxel representation of the domain by linking the Geo-Dict voxel mesh generation software to the MATLAB image processing toolbox.



The volumetric mesh is generated in the voxel format from the 3D binary matrix. The cross sectional images of the porous structure are generated based on 2D arrays extracted from the 3D binary matrix using the image processing MATLAB toolbox. These images are saved as a sequence of images and are inserted into Geo-Dict to generate the volumetric voxel mesh.

The whole procedure of mesh generation that includes reading the 3D binary matrix, creating the 2D cross sectional images and importing them into the Geo-Dict software is fully automated using in-house developed MATLAB scripts. By implementing this method an efficient and flexible approach to automatically generate the voxel mesh representation of the domain, as required for design purposes, is presented.

Implementing the presented methods, the volumetric mesh for both composite and woven structures is generated as shown in Figures 8.6 and 8.7. Although this method is capable of mesh generation for all types of porous structures, the size of the generated mesh is large due to the fine voxel size that needs to be implemented. The accuracy of the final mesh also depends upon the image processing software that converts the voxel format to a recognizable mesh format for CFD software packages.

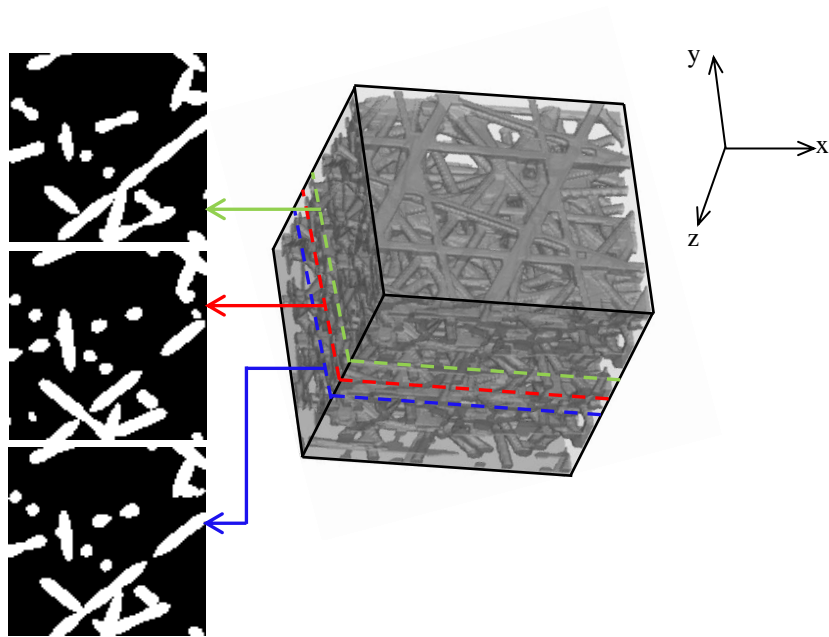


**Figure 8.6** Schematic illustrating generation of volumetric mesh for nonwoven structure [156].

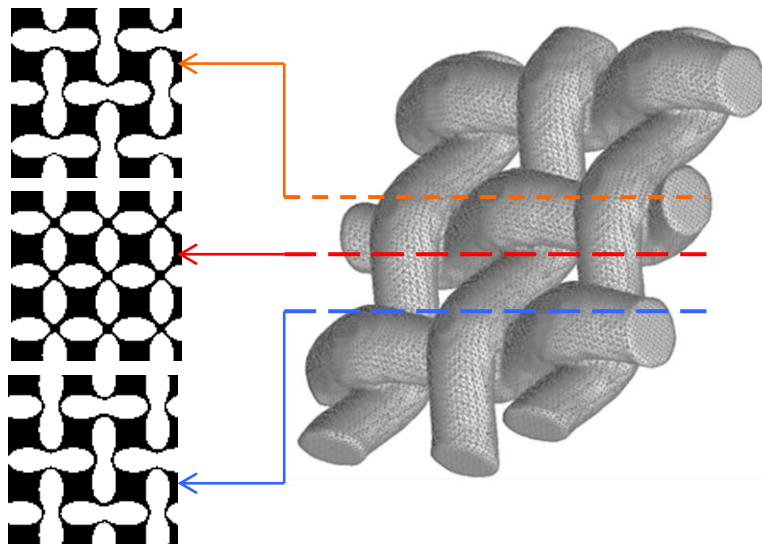


**Figure 8.7** Schematic of generation of volumetric mesh for woven structure.

## 8.2 Determining Permeability Tensor of Porous Media

The permeability of GDLs is a determining factor in predicting the flow field and the performance of the PEMFCs. Permeability,  $K$ , of a porous media can be defined by Darcy's law:

$$V = -\frac{K}{\mu} \nabla P \quad (8.1)$$

where  $V$  is the superficial velocity (i.e., volumetric flow rate per unit cross sectional area),  $\mu$  is fluid viscosity and  $\nabla P$  is the pressure drop per unit length through the porous material. Darcy's law can be extended to use for 3D flow fields. In this case  $V$  is in the vector form and  $K$  is a second order symmetric tensor given as:

$$K = \begin{bmatrix} K_{xx} & K_{xy} & K_{xz} \\ K_{yx} & K_{yy} & K_{yz} \\ K_{zx} & K_{zy} & K_{zz} \end{bmatrix} \quad (8.2)$$

When the principal axes and the coordinate axes are parallel with each other, the permeability tensor changes to a diagonal tensor with three elements of  $K_{xx}$ ,  $K_{yy}$  and  $K_{zz}$ . Darcy's law is valid for Newtonian incompressible flow under viscous conditions at low Reynolds number. The permeability of porous materials strongly depends on the microstructure of those specific porous media.

### 8.2.1 Governing Equation

The momentum and mass conservation equations under steady state and isothermal condition that govern the flow behavior through the porous media are, respectively,

$$\nabla \cdot \mathbf{u} = 0 \quad (8.3)$$

$$\rho \mathbf{u} \cdot \nabla \mathbf{u} = -\nabla P + \nabla \cdot \hat{\boldsymbol{\tau}} \quad (8.4)$$

where  $\mathbf{u}$  is the velocity,  $\rho$  is density,  $P$  is the pressure field, and  $\hat{\boldsymbol{\tau}}$  is the stress tensor.

### 8.2.2 Computational Domain and Boundary Conditions

An isometric view of the  $200\mu\text{m} \times 200\mu\text{m} \times 200\mu\text{m}$  computational domain is shown in Figure 8.8. To determine the permeability in a desired direction, the inlet and outlet boundary conditions are set to that specific flow direction. At the inlet, a constant velocity normal to the boundary is defined, while at the outlet an outflow condition is imposed. The boundary conditions for calculating the through-plane permeability ( $K_{zz}$ ) are also depicted in Figure 8.8. No slip boundary condition is applied to the internal solid-fluid interface, which are the outer surfaces of the fibers. To minimize the end effects on the flow field, identical auxiliary zones at the inlet and outlet of the two opposite faces in the direction of interest are added to the main porous domain.

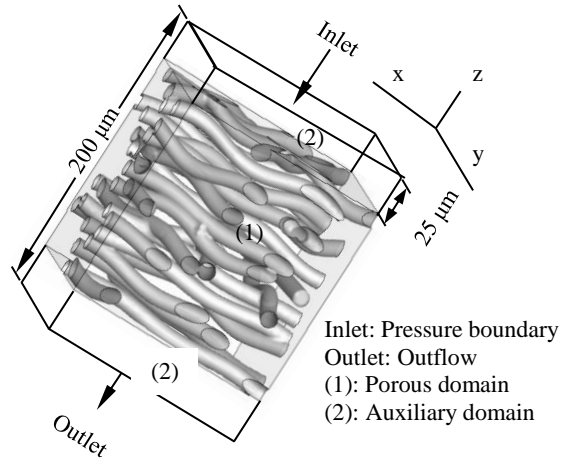


**Figure 8.8** Computational domain and boundary conditions to calculate  $K_{zz}$  [152].

### 8.2.3 Numerical Discretization

The numerical simulations are conducted using commercial ANSYS/FLUENT 12.1.4 software. The momentum equation is discretized by the second order upwind scheme with the SIMPLE algorithm for the pressure-velocity coupling [157]. The under relaxation factors of 0.25 and 0.55 for pressure and momentum are used, respectively. The convergence criteria of  $1e^{-6}$  are considered for the numerical simulations.

After the convergence of the results, the area-averaged pressure at the inlet and outlet is calculated. Therefore, given the GDL thickness, the pressure gradient in the GDL can be found. The superficial velocity is calculated by volume averaging of the velocity fields in the GDL. Hence, having the superficial velocity and the pressure gradient the permeability is computed from Equation 8.1.

#### **8.2.4 Mesh Study**

To choose the appropriate mesh size, a grid study has to be conducted for the virtually generated GDLs. In this section, the mesh study conducted on a virtual GDL with porosity of 0.8 is discussed. A uniform triangular surface mesh is generated for all the surfaces and an unstructured mesh grid of tetrahedral cells is generated for the volume. To have viscous flow, an inlet velocity of 0.01 m/s is applied in the z-direction and the pressure drop is calculated for different mesh sizes. As shown in Figure 8.9, the predicted value of the pressure drop inside the porous zone is not a function of the applied mesh size if the mesh number exceeds 350,000, which corresponds to the mesh size of 2.35  $\mu\text{m}$ .

Figure 8.10 illustrates the relationship between the applied inlet velocity and the generated pressure gradient inside the porous GDL for three different values of porosity, 0.75, 0.8 and 0.85, which are the most common values for the GDLs porosity. As shown in the figure, the relationship between the pressure gradient and velocity is linear for all of three porosity values. Given the same inlet velocity, the pressure gradient is larger for the lower values of porosity, which corresponds to the denser material. The linearity between the pressure gradient and the inlet velocity indicates the validity of the Darcy's law inside the GDL. However, by further increase of the inlet velocity, the flow behavior diverges from Darcy's law because of the effect of momentum losses.

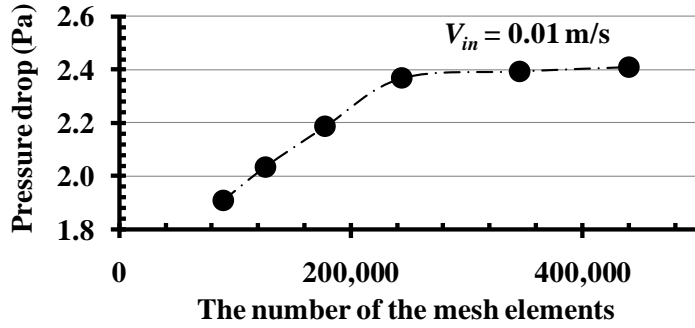


**Figure 8.9** Effect of the mesh size on the pressure drop,  $V = 0.01$  m/s,  $\varepsilon = 0.8$  [4].

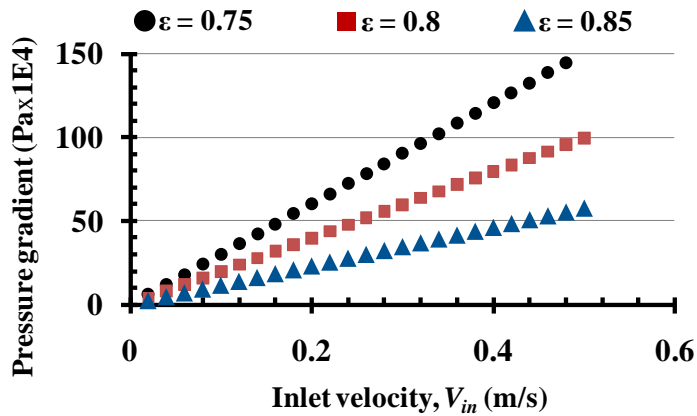


**Figure 8.10** Pressure gradient inside the GDL as a function of inlet velocity and porosity [4].

### 8.2.5 Determining Size of RVE

In order to find the proper computational domain size, first the Brinkman screening length criteria ( $L_c$ ) is used.  $L_c$  is a function of the permeability of the medium and equal to  $K^{0.5}$  [158] where  $K$  is the permeability of the porous media. It has been shown that a computational domain with length 14 times greater than  $L_c$  is large enough

to smooth out the inhomogeneity [159]. Given the range of permeability for GDLs, to determine the RVE size for the computational runs a sensitivity study is conducted on RVEs size of  $100 \times 100 \times 100 \mu\text{m}$ . The permeability of the reconstructed GDLs, with the fibers diameter of  $7 \mu\text{m}$  and porosity ( $\epsilon$ ) of 0.82 are found. As given in Table 8.1, the randomness of the structure alters the predicted permeability. Thus, the Brinkman screening length criteria is not valid for determining the RVE size of fibrous porous media.

To find the best RVE size, the sensitivity study is conducted on the RVEs size of  $200 \times 200 \times 200 \mu\text{m}$ . The paper GDL with porosity of 0.82 and the composite GDL with binder and porosity of 0.78 are constructed for this RVE size. The through-plane and in-plane permeability of both structures are computed and given in Tables 8.2 to 8.5. As given in the tables, the effect of randomness on the predicted permeability values is negligible. The microstructures of these GDLs are also constructed for RVE of  $400 \times 400 \times 200 \mu\text{m}$ . The predicted values of the through-plane and in-plane permeability are given in Table 8.6. As presented in the table, the results for RVE of size  $200 \times 200 \times 200 \mu\text{m}$  and  $400 \times 400 \times 200 \mu\text{m}$  are very close. Thus, in this study the RVE size of  $200 \times 200 \times 200 \mu\text{m}$  is selected for computing the transport properties of interest.



**Table 8.1** Through-plane permeability of paper GDL porosity of 0.82 and computational domain size of  $100 \times 100 \times 100 \mu\text{m}$  according to the Brinkman screening length criteria.

Runs	Permeability ( $\text{m}^2$ )
Run1	$9.01 \times 10^{-12}$
Run2	$1.3 \times 10^{-11}$
Run3	$8.81 \times 10^{-12}$
Run4	$7.78 \times 10^{-12}$
Run5	$1.02 \times 10^{-11}$
Run6	$6.45 \times 10^{-12}$
Average	$9.1 \times 10^{-12} (\pm 30\%)$

**Table 8.2** Through-plane permeability of paper GDL porosity of 0.82 and computational domain size of  $200 \times 200 \times 200 \mu\text{m}$ .

Runs	Permeability ( $\text{m}^2$ )
Run1	$9.85 \times 10^{-12}$
Run2	$1.03 \times 10^{-11}$
Run3	$9.78 \times 10^{-12}$
Run4	$9.62 \times 10^{-12}$
Run5	$1.03 \times 10^{-11}$
Run6	$9.13 \times 10^{-12}$
Average	$9.83 \times 10^{-12} (\pm 7\%)$

**Table 8.3** Through-plane permeability of paper GDL with binder, porosity of 0.78 computational domain size of  $200 \times 200 \times 200 \mu\text{m}$ .

Runs	Permeability ( $\text{m}^2$ )
Run1	$7.20 \times 10^{-12}$
Run2	$6.89 \times 10^{-12}$
Run3	$7.00 \times 10^{-12}$
Run4	$7.16 \times 10^{-12}$
Run5	$6.20 \times 10^{-12}$
Run6	$7.01 \times 10^{-12}$
Average	$6.89 \times 10^{-12} (\pm 9\%)$

**Table 8.4** In-plane permeability of paper GDL porosity of 0.82 and computational domain size of  $200 \times 200 \times 200 \mu\text{m}$ .

Runs	Permeability ( $\text{m}^2$ )
Run1	$1.36 \times 10^{-11}$
Run2	$1.19 \times 10^{-11}$
Run3	$1.32 \times 10^{-11}$
Run4	$1.37 \times 10^{-11}$
Run5	$1.42 \times 10^{-11}$
Run6	$1.33 \times 10^{-11}$
Average	$1.19 \times 10^{-11} (\pm 10\%)$

**Table 8.5** In-plane permeability of paper GDL with binder, porosity of 0.78 computational domain size of  $200 \times 200 \times 200 \mu\text{m}$ .

Runs	Permeability ( $\text{m}^2$ )
Run1	$1.06 \times 10^{-11}$
Run2	$1.16 \times 10^{-11}$
Run3	$1.21 \times 10^{-11}$
Run4	$1.18 \times 10^{-11}$
Run5	$9.97 \times 10^{-12}$
Run6	$1.18 \times 10^{-11}$
Average	$1.13 \times 10^{-11} (\pm 11\%)$

**Table 8.6** In-plane and through-plane permeability of paper GDL with and without binder, computational domain size of  $200 \times 200 \times 200 \mu\text{m}$  and  $400 \times 400 \times 400 \mu\text{m}$ .

Structure	$K_{zz}$ ( $\text{m}^2$ )	$K_{xx}$ ( $\text{m}^2$ )	$K_{yy}$ ( $\text{m}^2$ )
Domain $200 \times 200 \times 200 \mu\text{m}$			
Fibers only, $\varepsilon = 0.82$	$9.48 \times 10^{-12}$	$1.35 \times 10^{-11}$	$1.32 \times 10^{-11}$
With Binder, $\varepsilon = 0.78$	$6.11 \times 10^{-12}$	$1.21 \times 10^{-11}$	$1.18 \times 10^{-11}$
Domain $400 \times 400 \times 200 \mu\text{m}$			
Fibers only, $\varepsilon = 0.82$	$9.07 \times 10^{-12}$	$1.32 \times 10^{-11}$	$1.31 \times 10^{-11}$
With Binder, $\varepsilon = 0.78$	$6.01 \times 10^{-12}$	$1.19 \times 10^{-11}$	$1.18 \times 10^{-11}$

### 8.3 Determining Tortuosity of Porous Media

The other important transport property of porous media is tortuosity ( $\tau_p$ ), which represents the complexity of the microscopic flow paths in the porous substance.

Tortuosity is defined as the ratio of average length of the flow path to the characteristic length of the porous medium.

The thickness of porous medium in the flow direction is usually assumed as the characteristic length. For inhomogeneous porous structures, depending on the direction of the flow (in-plane or through-plane), flow tortuosity can be different. To calculate the tortuosity in the desired direction, the average fluid path length is computed from the following equation

$$\tau_p = \frac{\frac{1}{N} \sum_{i=1}^N l(r_i)}{L_t} \quad (8.5)$$

where  $N$  is the number of the particles which are tracked,  $l(r_i)$  is the length of the path line that belongs to the  $i^{th}$  particle located at  $r_i$ , and  $L_t$  is the GDL thickness. After convergence of the numerical simulation, for 2500 particles, the path line length is computed and tortuosity of the GDL for the through-plane and in-plane directions is calculated.

#### 8.4 Determining Diffusivity of Porous Media

Diffusivity in porous media ( $D_{bulk}$ ) is defined as  $D_{bulk} = D_{rel} \times D_0$ , where  $D_0$  is the binary diffusion coefficient which is equal to:

$$D_0 = \frac{1}{3} \lambda v \quad (8.6)$$

where  $\lambda$  is the mean free path of the gas that passes through the porous media.  $v$  is the thermal velocity defined as

$$v = \sqrt{\frac{8k_B T}{\pi m_g}} \quad (8.7)$$

where  $k_B$  is the Boltzmann constant,  $T$  is temperature and  $m_g$  is the molecular mass.  $D_{rel}$  is the relative diffusivity, which represents the reduction of the diffusivity in the porous media due to the presence of the solid phase.  $D_{rel}$  is a material property that is independent of the physical fluid (liquid or gas) that passes through the medium.

#### **8.4.1 Determining the Diffusion Mode**

To determine the mechanism by which diffusion takes place inside the pore space the Knudson number ( $Kn$ ) is used.  $Kn$  is defined as the ratio of the mean free path of a specific fluid ( $\lambda$ ) to the available length scale inside the porous structure [105]. As shown schematically in Figure 8.11, this length scale, which is set as the average chord length ( $\bar{L}_{ch}$ ), dictates the freedom to move inside the pore space.

In the current study, the diffusivity of  $O_2$ ,  $H_2$  and  $H_2O$ , which are used in PEMFCs, are computed. The mean free path for  $H_2$ ,  $O_2$ , and  $H_2O$  are presented in Table 8.7 [92]. Knowing the chord length distribution and its average value from the morphology characterization, the average  $Kn$  numbers are calculated and given in Table 8.7. The Knudsen numbers are smaller than one, indicating that the pore diameters are large compared to the mean free path length of the fluid molecules. Thus, the diffusion in

the pores is governed by the concentration Laplace equation given in Section 8.4.2.

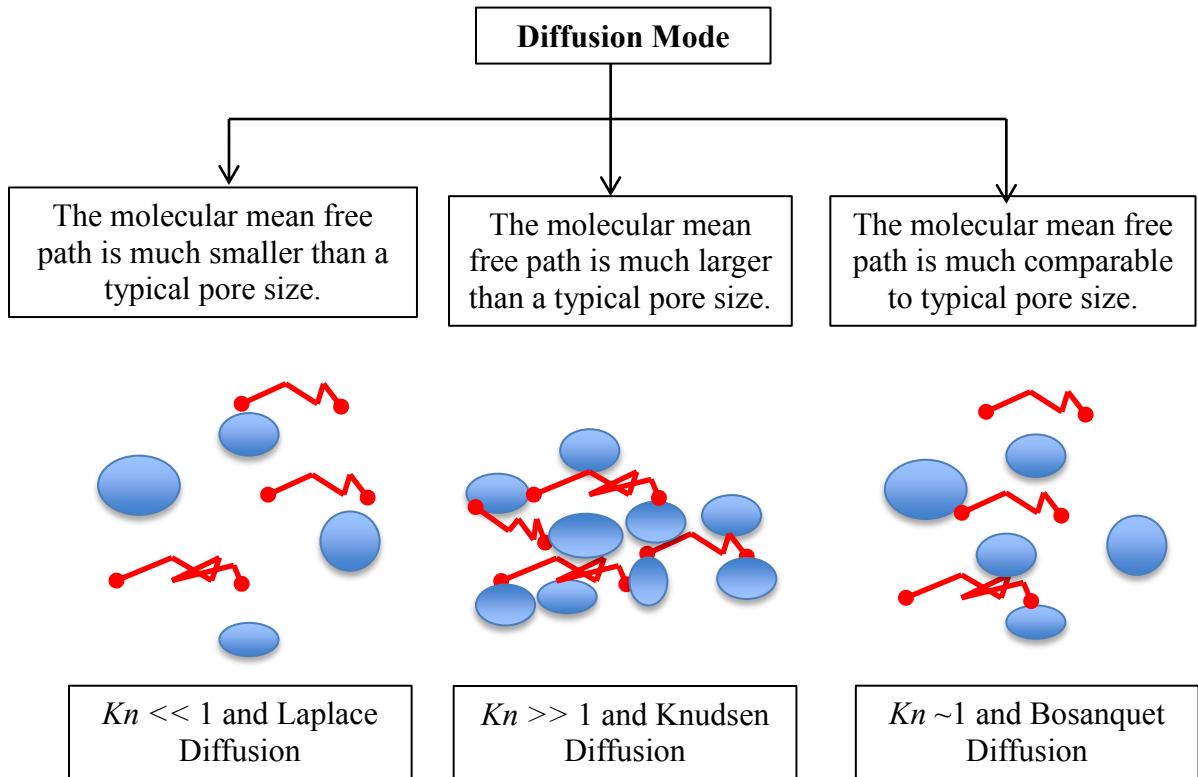


**Figure 8.11** The schematic of a microstructure and the corresponding diffusion mode.

**Table 8.7** Average Knudson number in Toray 060 GDL at T=100°C and P=100 KPa.

Fluid type	$\lambda$ (m)	$Kn$ number
$H_2O$	$7.5 \times 10^{-7}$	$1.2 \times 10^{-2}$
$O_2$	$6.1 \times 10^{-7}$	$9.7 \times 10^{-3}$
$H_2$	$1.3 \times 10^{-7}$	$2.1 \times 10^{-3}$

### 8.4.2 Governing Equations and Computational Domain

The Laplace equation is given by

$$-\Delta C = 0 \quad (8.8)$$

where  $C$  is the concentration of the gas in the pore space. To find  $D_{rel}$ , Equation 8.8 is solved using Geo-Dict software by applying a concentration gradient in the  $D_{rel}$  direction and a zero flux at the solid surfaces, shown schematically in Figure 8.12. Then knowing the concentration gradient and the diffusive flux ( $j$ ) the diffusivity is found from Fick's law given as Equation 8.9. Knowing the diffusivity,  $D_{rel}$  can then be computed.

$$j = -D_{bulk} \nabla C \quad (8.9)$$

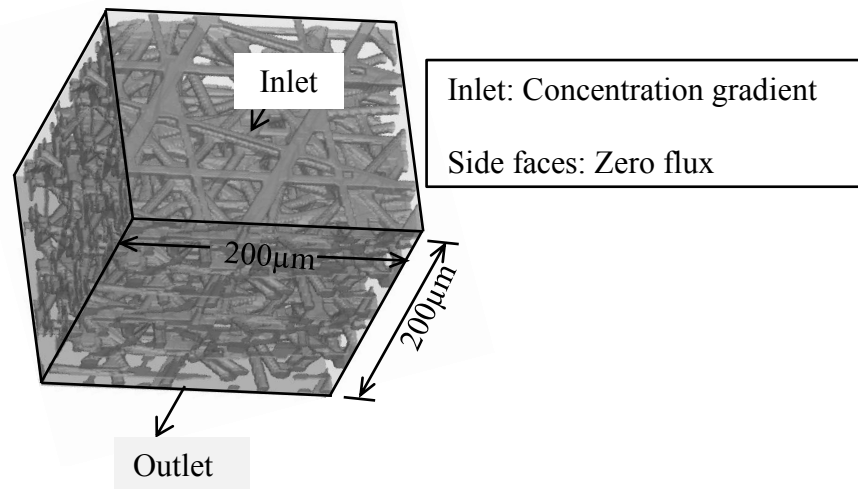


**Figure 8.12** The schematic of the computational domain and boundary conditions.

## 8.5 Determining Tortuosity Factor of Porous Media

After determining  $D_{rel}$ , the tortuosity factor ( $\tau_f$ ) can be calculated by

$$\tau_f = \frac{\varepsilon}{D_{rel}} \quad (8.10)$$

where  $\varepsilon$  is the porosity of the porous domain.

## 8.6 Summary

In this chapter, a dynamic transport characterization approach that is required for a systematic design is introduced. In the suggested approach, the volumetric mesh representation of the computational domain is generated automatically from the virtually constructed geometries of the PS model. The proper mesh generation approaches that can generate a high quality mesh for porous structures with different microstructures are introduced.

The transport properties of fibrous porous media i.e., permeability, tortuosity and diffusivity are explained. The numerical methods, governing equations and the corresponding computational domains that are required to compute these properties are presented. The effects of a microstructure's topology on its transport properties are discussed. It is discussed that the diffusion mode depends upon its Knudson number, which is a function of the chord length distribution in the porous material. The dependency of the diffusivity on the  $Kn$  number illustrates the importance of conducting morphological analysis over the porous media.



## **9. TRANSPORT PROPERTIES OF FIBROUS POROUS MEDIA, RESULTS**

In this chapter the transport properties of carbon paper GDL, composite paper with different binder volume fraction, woven carbon cloth and carbon felt GDLs are found. To check the accuracy of the suggested modeling and characterization approaches the transport properties of virtually generated Toray 060 carbon paper, H2315 felt and woven GDLs are found and compared with experimental data. In addition, the effects of the implemented geometrical modeling approach and the structural properties of the fibrous media on their transport properties are also investigated.

### **9.1 Transport Properties of Paper, Felt and Woven Gas Diffusion Layers**

To verify the accuracy of the suggested modeling and transport characterization approaches the flow field inside the virtual microstructures, as shown in Figure 9.1, is solved. The through-plane and in-plane permeability, relative diffusivity, tortuosity and effective tortuosity of Toray 060 GDL modeled with a disk SE, are calculated and given in Table 9.1.

Due to the semi-layered structure of the GDL, the transport properties in the through-plane direction are lower than the in-plane direction. A good agreement exists between experimental measurements and the numerical data that are extracted from the virtually constructed microstructure. However, It should be mentioned that the discrepancy exist in the available experimental values of the transport properties, which

can be attributed to the unrepeatable manufacturing techniques and the compression of the GDLs during the experimental procedures.

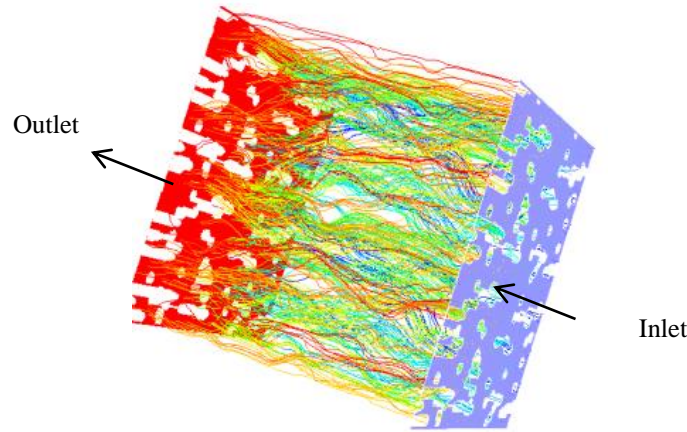


**Figure 9.1** The flow field inside Toray 060 GDL, contour of fluid path lengths.

**Table 9.1** Transport properties of Toray 060 GDL.

Results	Direction	Permeability (m <sup>2</sup> )	Relative diffusivity	Effective Tortuosity	Tortuosity
Numerical	Through-plane	$6.8 \times 10^{-12}$	0.42	1.85	1.19
	In-plane	$1.19 \times 10^{-11}$	0.67	1.17	1.06
Experimental	Through-plane	$5.2 \times 10^{-12}$ [39]	0.38 [27]	2.05	NA
	In-plane	$2.1 \times 10^{-11}$ [160]	0.57[27]	1.36	NA

Transport properties of Freudenberg H2315 GDL generated by the energy coupled modeling approach are computed and given in Table 9.2. The numerical approximations of the transport properties are in good agreement with the experimental

data. Although the porosity and thickness of Freudenberg H2315 felt and Toray 060 are the same, the felt GDL has higher permeability in both through-plane and in-plane directions. The radius of the fibers in the felt GDL is  $4.5\mu\text{m}$  and  $3.5\mu\text{m}$  in the paper. Defining the dimensionless permeability as  $K/r^2$ , the dimensionless permeability of felt and paper GDLs in the in-plane and through-plane directions are 1.4 and 0.98 and 0.58 and 0.34, respectively. The difference between the permeability and dimensionless permeability of felt and paper GDLs is due to the curvature of the fibers in the felt GDL. The curved fibers result in a pore space in which the chord lengths in the in-plane and through-plane directions are close to each other, resulting in round pores. Pores with aspect ratios close to one exert lower resistance to the flow field. Thus, the permeability of the corresponding GDL will be higher.

**Table 9.2.** Transport properties of Freudenberg H2315 GDL.

Results	Direction	Permeability ( $\text{m}^2$ )	Relative diffusivity	Effective Tortuosity	Tortuosity
Numerical	Through-plane	$2.1 \times 10^{-11}$	0.47	1.65	1.72
	In-plane	$2.85 \times 10^{-11}$	0.56	1.39	1.65
Experimental	Through-plane	$2.5 \times 10^{-11}$ [161]	Not available	Not available	NA
	In-plane	$3 \times 10^{-11}$ [160]	0.50 [27]	1.56	NA

Darcy's law is solved in the RVE of a carbon cloth GDL and the resultant flow field is shown in Figure 9.2. The through-plane and in-plane permeability and tortuosity

are found and given in Table 9.3. The through-plane permeability of carbon cloth is on the same order of felt and paper structures. However, the in-plane permeability of carbon cloth is a couple of orders of magnitude higher than felt and paper GDLs.

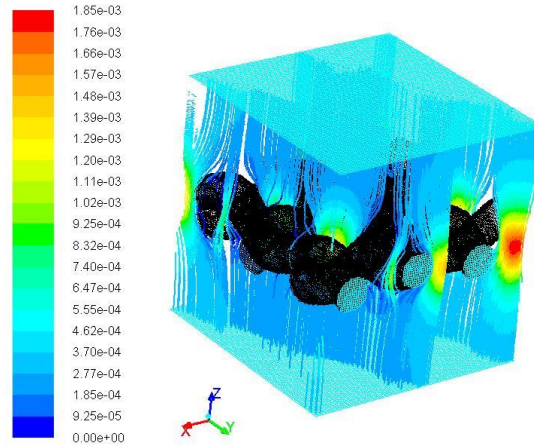


**Figure 9.2** The flow field inside the woven carbon cloth, contour of velocity.

**Table 9.3** Transport properties of woven GDL, in the through-plane direction.

Results	Through -plane Permeability (m <sup>2</sup> )	In-plane Permeability (m <sup>2</sup> )	Through -plane Tortuosity	In -plane Tortuosity
Numerical	$2.55 \times 10^{-12}$	$7.50 \times 10^{-10}$	1.04	1.02
Experimental [10]	$2 \times 10^{-12} \sim 3 \times 10^{-11}$	$4 \times 10^{-11} \sim 4 \times 10^{-9}$	NA	NA

The large difference in the in-plane characteristics of woven and nonwoven materials is due to the difference in their topology. Various layers of fibers in the nonwoven GDLs reduce the flow pressure, while in the woven GDLs the single layer yarn does not exert high resistance to the flow field in the in-plane direction.

## 9.2 Interplay of Morphological and Transport Properties of Porous Structure

As mentioned in Chapter 5, to model the impregnated binder in a composite different types of SE can be used. To determine a SE that can accurately represent the composite fibrous structures, the transport properties of the microstructures generated by 2D and 3D SEs are computed and given in Table 9.4. The transport properties of both structures in the in-plane direction are approximately the same. However, the microstructure generated by 3D SE has higher through-plane permeability compared to the microstructure generated by 2D SE. As mentioned in Section 7.7, the average chord length of the microstructure generated by 3D SE is 30 % larger than the average chord length of the GDL generated by 2D SE in the through-plane direction. This, results in higher through-plane permeability for the GDL generated by 3D SE. However, permeability of the microstructure generated by 2D SE is closer to the experimentally measured data for Toray 060, which is  $5.2 \times 10^{-12} \text{ m}^2$ .

The relative diffusivity of the GDL generated by 3D SE in the in-plane and through-plane directions are closer compared to the GDL generated by 2D SE. This may be due to the similarity of the topology of the generated microstructure with the 3D SE in the through-plane and in-plane directions. The homogenous structure has shorter paths in the through-plane direction compared to the microstructure generated by 2D SE. This results in higher permeability and diffusivity for this direction. Negligible changes are observed in tortuosity for both structures. As given in Table 9.4, including the binder in the geometrical model is important. The transport properties of a GDL, which is only composed of fibers are not close to the experimentally measured data, because the fiber only microstructures do not have the layered topology of the conventional paper media.

**Table 9.4** Transport properties of Toray 060 GDL modeled with different structure elements.

SE type	Direction	Permeability (m <sup>2</sup> )	Relative diffusivity	Effective Tortuosity	Tortuosity
Disk, 2D	Through-plane	$6.8 \times 10^{-12}$	0.42	1.85	1.19
	In-plane	$1.19 \times 10^{-11}$	0.67	1.17	1.06
Cube, 3D	Through-plane	$8.1 \times 10^{-12}$	0.51	1.53	1.18
	In-plane	$1.14 \times 10^{-11}$	0.61	1.28	1.06
Fiber, only	Through-plane	$6.67 \times 10^{-12}$	0.60	1.28	1.17
	In-plane	$6.14 \times 10^{-12}$	0.63	1.30	1.05
Experimental	Through-plane	$5.2 \times 10^{-12}$	0.38	2.05	NA
	In-plane	$2.1 \times 10^{-11}$	0.57	1.36	NA

Based on these results, it is found that to accurately predict the transport behavior finely-detailed geometrical models of porous structures have to be generated. Also it is shown that transport properties are strongly dependent on the morphological properties. Due to the semi-layered structure of the carbon paper GDL, the 2D disk SE is selected as the best filler for virtual representation of the impregnated binder in the GDL. Two methods of energy coupled modeling and geometrical modeling approaches are introduced to model felt porous media. The transport properties of the Freudenberg H2315 GDL modeled with both approaches are found and given in Table 9.5. As

presented in the table, due to unlimited bending of the fibers, the difference between the diffusivity and permeability of the felt structure generated by the geometrical modeling approach in the through-plane and in-plane direction is large and not close to the experimentally measured data. Hence, the energy coupled modeling approach is used for generating the felt structures.

**Table 9.5** Transport properties of Freudenberg H2315 GDL.

Results	Direction	Permeability (m <sup>2</sup> )	Relative diffusivity	Effective Tortuosity
Energy Coupled model	Through-plane	2.1×10 <sup>-11</sup>	0.47	1.65
	In-plane	2.85×10 <sup>-11</sup>	0.56	1.39
Geometrical model	Through-plane	8.8×10 <sup>-12</sup>	0.54	1.44
	In-plane	1.25×10 <sup>-11</sup>	0.63	1.24

### 9.3 Effects of Matrix Properties on the Characteristics of Composite Media

To study the effects of binder quantity (matrix weight fraction in the composite media) on the transport properties, the volume fraction of binder in the GDL is change from 10% to 65% while keeping the solid volume fraction of the fibrous bundle constant and equal to 16%.

The dimensionless permeability,  $K/r^2$ , and relative diffusivity of the microstructures are calculated and given in Figure 9.3. As the binder volume fraction increases both properties decrease, but larger changes are observed in the through-plane

direction. By increasing the binder volume fraction from 10% to 65%, permeability decreases 37% and 67% and relative diffusivity reduces by 22% and 69% in the in-plane and through-plane directions, respectively. It is shown that although increasing binder volume fraction reduces both properties, the in-plane permeability is more sensitive to the volume of binder compared to the in-plane relative diffusivity.

The variation of tortuosity and effective tortuosity versus the amount of binder in the GDL is shown in Figures 9.4 and 9.5. As shown, effective tortuosity in the through-plane direction depends heavily on the volume fraction of binder. This behavior is due to the change in the morphological properties of the GDL under different binder loading.

In Section 7.3, it is shown that the average chord length in the in-plane direction slightly increases with increasing binder. On the other hand, in the through-plane direction chord length sharply decreases. The average chord length in the in-plane direction changes 25%, while in through-plane direction changes by 76%. Because effective tortuosity is a function of relative diffusivity ( $D_{rel}$ ) and the free space available in the porous structure, it shows higher sensitivity to the volume fraction of the binder in the GDL. Although tortuosity changes with increasing volume fraction of binder, its change is relatively insignificant.



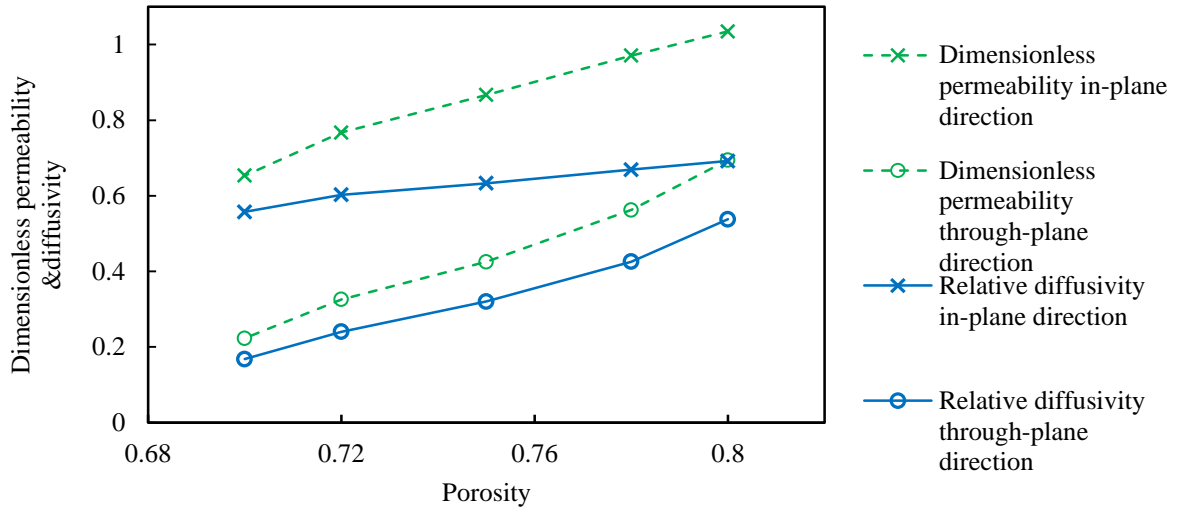


**Figure 9.3** Effect of volume fraction of binder in the GDL's structure on the permeability and relative diffusivity [156].

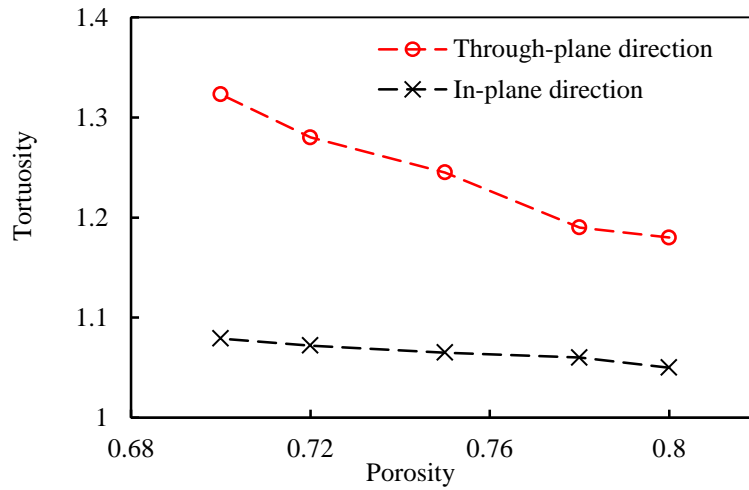


**Figure 9.4** Effect of volume fraction of binder in the GDL's structure on the tortuosity [156].

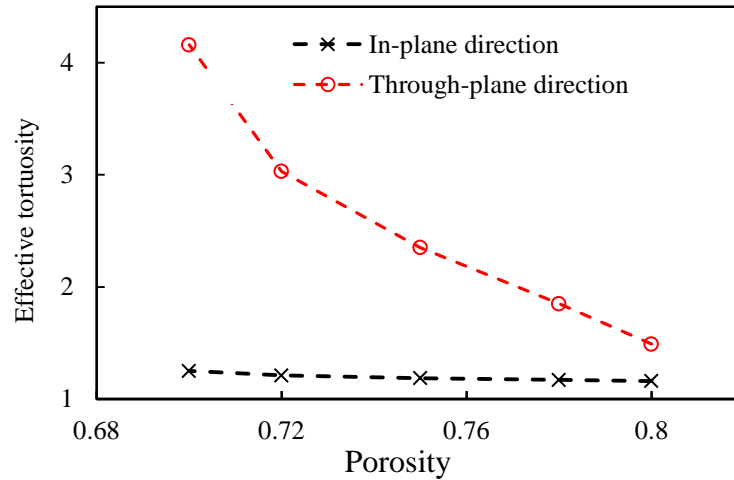


**Figure 9.5** Effect of volume fraction of binder in the GDL's structure on the effective tortuosity [156].

#### 9.4 Effects of Porosity of Felt Porous Media on the Transport Properties

The microstructures of felt porous GDLs are generated using the energy coupled PS model. The dimensionless permeability and relative diffusivity of felt GDLs are found. As shown in Figure 9.6, the through-plane and in-plane permeability reduces largely by decreasing the porosity. But, the through-plane and in-plane diffusivity of felt structure does not show high sensitivity to the porosity of the GDL. Due to the curvature of fibers in the felt GDL and the resulting tortuous paths, the effect of the topology of the microstructure on the diffusivity is dominant compared to the bulk porosity.

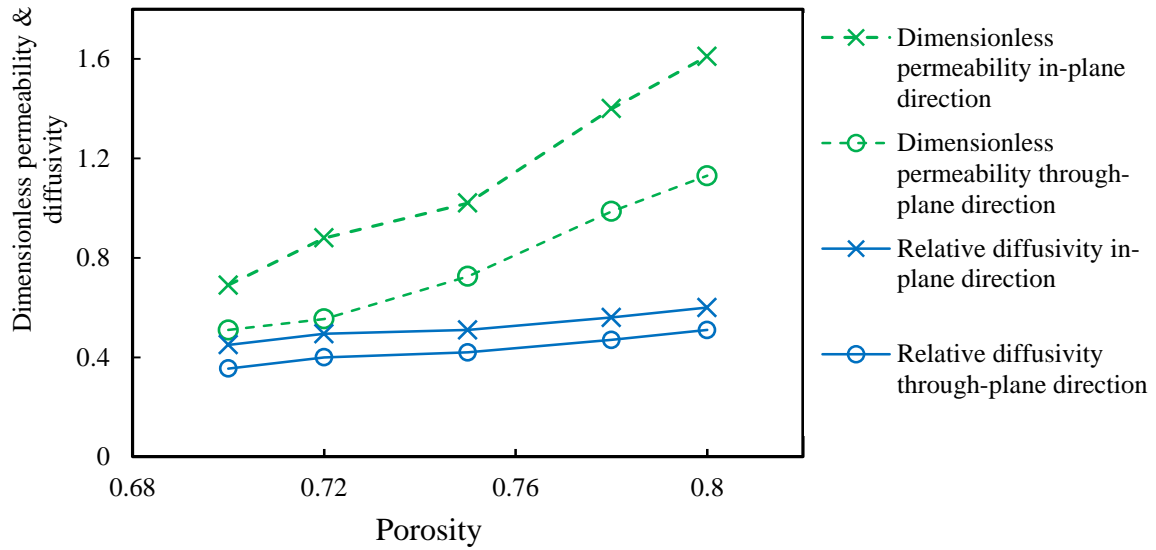


**Figure 9.6** Effect of porosity of felt GDLs on the permeability and diffusivity.

The change of the effective tortuosity versus the porosity for in-plane and through-plane directions is shown in Figure 9.7. As shown in the figure, the effective tortuosity of the felt structure in the through-plane direction is larger for the denser structures. However, the effective tortuosity of the felt structure is not as sensitive as the paper structures to the porosity. It is concluded that the diffusivity of the felt structures heavily depends on the tortuous topology rather than the bulk material properties such as porosity.

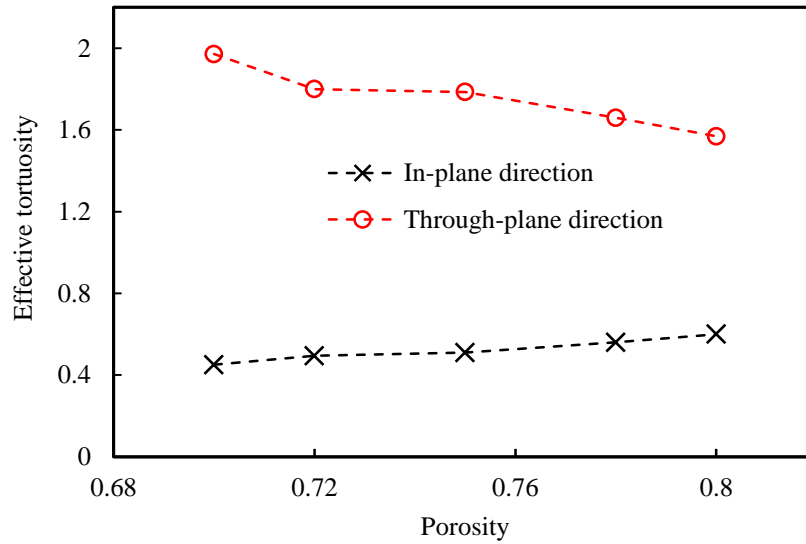


**Figure 9.7** Effect of porosity of felt GDLs on the effective tortuosity.

#### 9.4 Summary

Transport properties of the virtually generated Toray 060, Freudenberg H2315 and carbon cloth GDLs are found utilizing the methods described in Chapter 8. The computed transport properties are compared and verified against the experimentally measured data. Showing good agreement to experimental data proves the accuracy of the suggested modeling and characterization approaches.

To study the importance of utilizing a precise geometrical modeling approach, the impregnated binder in the composite carbon paper GDLs is modeled with different structure elements. Also carbon felt GDL is constructed with both geometrical modeling and energy coupled modeling approaches. As discussed in the chapter, it is found that both morphological and transport properties of the GDLs depend upon the topology of the virtually constructed microstructures.

The effect of binder volume fraction on the transport properties of composite GDLs is investigated. It is shown that the volume fraction of binder in the microstructure not only changes its morphological characteristic, but also its transport properties. It is found that binder volume fraction has a larger impact on permeability, relative diffusivity and effective tortuosity compared to tortuosity. However, higher changes are observed in the through-plane direction compared to the in-plane direction. This behavior can be due to the larger reduction of chord length in the through-plane direction, which illustrates the interplay between the morphological and transport properties of composite fibrous structures.

The effects of the porosity of the felt GDLs on their transport properties are studied. It is found that permeability of felt and composite paper structures depend heavily on the porosity. Decreasing porosity reduces the diffusivity and permeability in the in-plane and through-plane directions. But the change in the diffusivity of felt structures is smaller compared to the paper materials. Thus, it is concluded that the determinant factor on the diffusivity of felt structures is their topology. Due to the curvature of fibers in the felt GDLs, their diffusivity largely depends on the available pore spaces of the media rather than porosity.

# **10. VIRTUAL CHARACTERIZATION OF COMPLEX POROUS MEDIA, METHODOLOGY**

To analyze a complex porous structure i.e, the structure with a thin-coated film over a porous medium, the penetration of a coating solution into a porous web has to be studied. In this chapter, the numerical simulation developed to model the penetration of a coating solution during slot die coating process is presented. For this purpose, a multi-scale approach is introduced that couples the macro scale slot die coating procedure to the micro scale penetration process. The first section of this chapter presents how this coupling is accomplished. Then, the macro scale simulation of a coating bead, the governing equations, required boundary conditions and the utilized numerical schemes are discussed. The micro scale simulation of penetration into a porous medium along with the relevant governing equations and the required boundary conditions are also discussed.

## **10.1 Multi Scale Simulation Approach for Modeling Coating Process**

In the slot die coating process a fluid or a coating solution is forced through the die and is suspended onto a moving web/substrate to form a thin layer on the substrate. If the web is porous, the coating solution is distributed on the substrate and pushed into the pore space by the convection-driven pressure field of the coating bead and capillary forces. As shown schematically in Figure 10.1, the coating bead can be divided in three distinct regions. In the first region, the pressure distribution on the web has a peak value that is a function of the operating conditions, including the capillary forces [131, 132]. In region (II), located beyond the slot die lip the pressure on the substrate is approximately

atmospheric. In region (II) and region (III) the time required by the solution to penetrate more into the web is much larger than region (I). In region (III), which is far away from the slot die lips, the coating solution may even solidify.

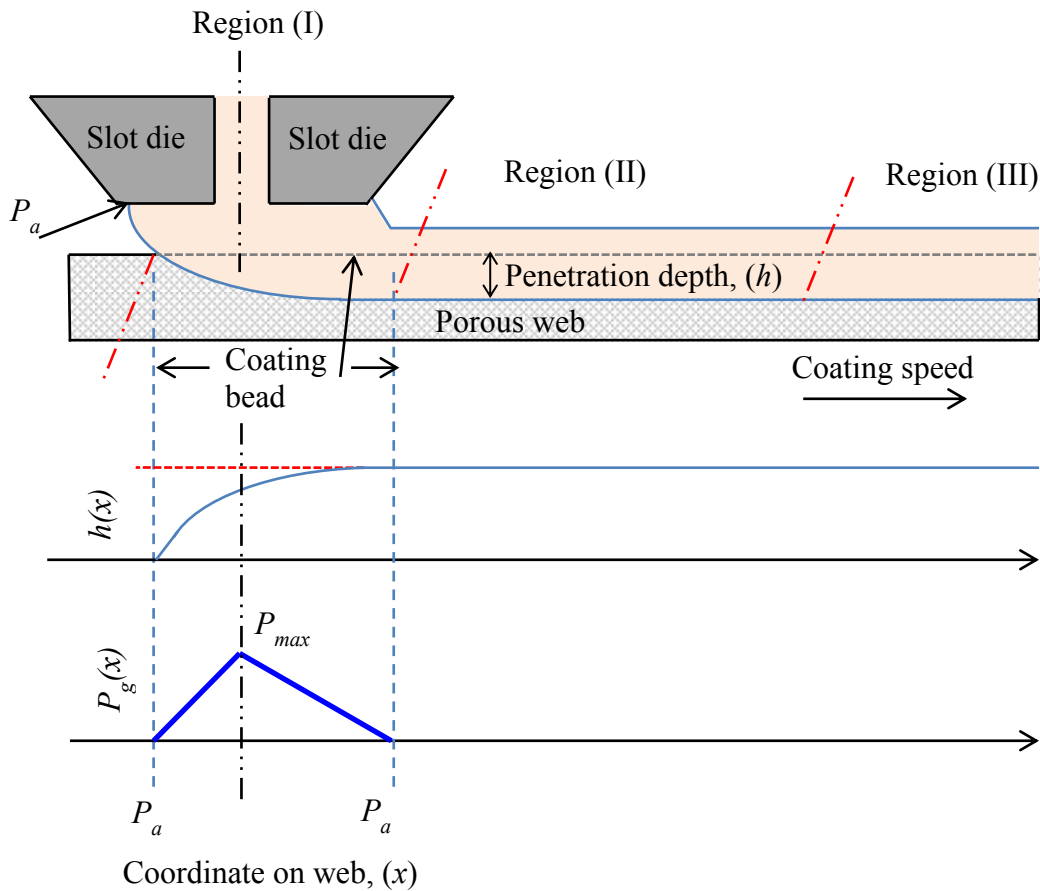


**Figure 10.1** Schematic of slot die coating process, the penetration depth and the pressure distribution on the web.

The liquid penetration into the porous web in region (I) is similar to the forced imbibition process, whereas in region (II) the penetration process is driven by capillary forces, similar as the free imbibition [123, 131, 133, 134]. The penetration process in region (I) is mainly due to the pressure pulses applied over very short time scale on the order of milliseconds. However, in region (II) and (III) is mainly due to the capillary

forces [123]. Thus, in this study it is assumed that the penetration mainly takes place in region (I) and approximately reaches to its final value in this region.

The convective-driven pressure field applied by the coating fluid on the top surface of the porous web is an important factor not only on the success or failure of the coating process but also on the amount of penetration into the substrate. As the coating web passes from Region (I) to region (II), the pressure at its top surface changes from atmospheric pressure to a maximum value in the film region then decreases to the atmospheric pressure at downstream. This pressure distribution is used as the boundary condition for the micro scale computational domain assuming that the flow at the coating bead is coupled with the flow into the porous medium by the pressure field.

To simulate the penetration process, a model that consists of the cross section of the fibrous structure with the boundary conditions extracted from the macro scale numerical simulation of the coating procedure is established. Coupling the macro and micro scales simulations, the dynamic equations for this two-phase microfluidic problem are found.

The micro scale domain is treated as a dimensionless point on the substrate, thus the pressure at the top surface of the domain is assumed to be uniform. When the coating is stable, the flow in the coating bead is assumed to be in steady state and the pressure distribution on the substrate does not change over time [162, 163]. By solving the macro scale coating bead the pressure through the web,  $P = f(x)$ , is extracted. Knowing the coating



serves as the boundary condition for micro scale domain can be found. Because of the linear dependency of the coating speed and time ( $u_w = dx/dt = x/t$ )  $x$  can be substituted with time, given  $P = f(u_w t) = g(t)$ , where  $x$  and  $u_w$  are the  $x$ -coordinate and coating speed,  $t$  is time and  $f$  and  $g$  are tentative functions describing the dependency of pressure on  $x$  and  $t$ .

The pressure distribution along the web is found by numerical simulation of the coating process in a computational domain shown schematically in Figure 10.2. Didari et al. [164] numerically solved the slot die coating process of impermeable webs using a two phase transient VOF method and found the pressure distribution over the solid substrate. However, the porosity of the web may alter the pressure distribution. Thus, using the pressure distribution found for impermeable web may result in inaccurate approximations.

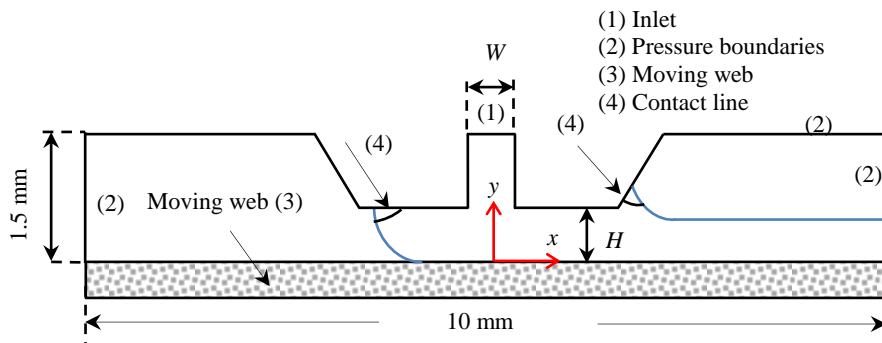


**Figure 10.2** The schematic of computational domain including the porous web.

The limitation of numerical simulation of the coating bead of a porous web lies in the abrupt change of porosity from the film to the moving porous web that results in a

numerical instability. To overcome this problem Ding et al. [16] developed a simulation approach that is implemented in this study.

## 10.2 Macro Scale Modeling of Coating Process

The slot die coating process of a porous web is simulated using Comsol 4.2a software for a computational domain shown in Figure 10.3. The two phase transient level set model embedded in Comsol software is used to solve the flow field equations. To avoid the numerical instability due to the porosity and velocity of porous web, the modeling approach suggested by Ding et al. [16] is implemented. The penetration of the coating solution into the porous web is modeled using an effective porosity with a leakage wall all across a moving web. As shown in Figure 10.3, the coating solution is assumed to leak from predefined control points through the web. At each control point, the speed of the coating solution front is found from Darcy's law.

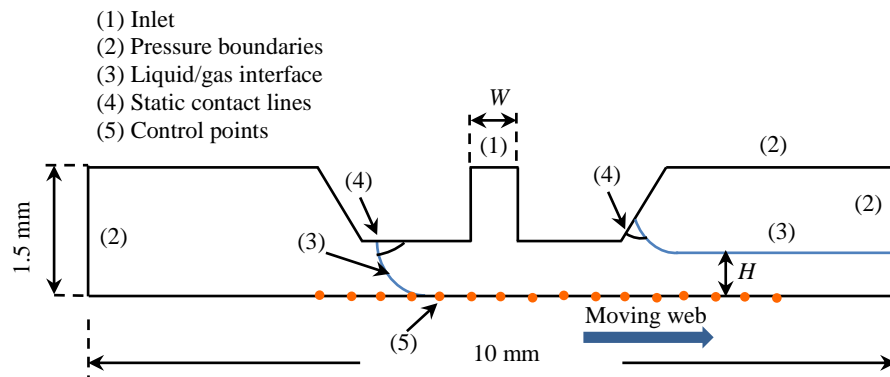


**Figure 10.3** The schematic of computational domain including the porous web.

### 10.2.1 Governing Equations

In the laminar two phase level set model, the interface is represented by a level set function ( $\varphi_l$ ) of 0.5. For air (gas) the level set function is assigned to 0 and for the coating solution  $\varphi_l$  is considered to be 1. The fluid interface can be tracked by solving Equation 10.1 given as:

$$\frac{\partial \varphi_l}{\partial t} + \mathbf{u} \cdot \nabla \varphi_l = \gamma \nabla \cdot \left( \epsilon \nabla \varphi_l - \varphi_l (1 - \varphi_l) \frac{\nabla \varphi_l}{|\nabla \varphi_l|} \right) \quad (10.1)$$

where  $\mathbf{u}$  is the velocity vector,  $\epsilon$  is the thickness of the interface that is set as half of the mesh size.  $\gamma$  is the initialization value that is set as the characteristic speed of the computational domain, which is equivalent to the coating speed.

The material properties, such as density ( $\rho$ ) and viscosity ( $\mu$ ) of the two phase flow occupying the cells of the computational domain can be found from Equation 10.2.

$$\rho = \rho_{air} + (\rho_{liquid} - \rho_{air})\varphi_l \quad (10.2)$$

The Navier-Stokes equations given by Equations 10.3 and 10.4 are used to solve for mass and momentum transports, respectively

$$\rho \frac{\partial \mathbf{u}}{\partial t} + \rho (\mathbf{u} \cdot \nabla) \mathbf{u} = \nabla \cdot (-P \mathbf{I} + \mu (\nabla \mathbf{u} + (\nabla \mathbf{u})^T)) + \mathbf{F}_{st} + \rho \mathbf{g} \quad (10.3)$$

$$\nabla \cdot \mathbf{u} = 0 \quad (10.4)$$

where  $t$ ,  $P$ ,  $\mathbf{I}$  and  $\mathbf{g}$  are time, pressure, identity matrix and gravitational vector, respectively. The surface tension force ( $\mathbf{F}_{st}$ ) that is modeled as a body force in Navier-Stokes equation is computed from Equation 10.5.

$$\mathbf{F}_{st} = \sigma(\mathbf{I} - (\mathbf{nn}^T))\delta \quad (10.5)$$

where  $\mathbf{n}$ ,  $\sigma$  and  $\delta$  are the normal vector at the interface, surface tension and Dirac delta function, respectively.

To model the leakage of coating solution through the control points Darcy's law is solved. It is assumed that the capillary pressure ( $P_c$ ) is exhibited while the coating solution penetrates into the porous web. At each control point the penetration speed is found from Equation (10.6).

$$v_j = \frac{(P_j - P_c) K}{h_j \mu} \quad (10.6)$$

where  $j$  is the index referring to the  $j^{\text{th}}$  control point.  $v_j$ ,  $h_j$  and  $P_j$  are the penetration speed, penetration depth and the pressure of coating bead at the  $j^{\text{th}}$  control point, respectively.  $K$  and  $\mu$  are the permeability of the porous web in the through-plane direction and the viscosity of the coating solution.

### ***10.2.2 Computational Domain and Boundary Conditions***

The schematic of the computational domain, its boundary conditions and the size of the domain are depicted in Figure 10.3. The boundary conditions used for the simulation are

- (1) Inlet boundary condition, where a fully developed velocity is defined for the coating solution.

(2) Free stream boundary condition, where the pressure is equal to the atmospheric pressure. Thus, zero gauge pressure, i.e.  $P_g = 0$  is applied.

(3) The liquid/gas interface boundary condition, where the sum of the capillary force and hydrostatic pressure on the air side balances the normal stress in the coating solution. At this boundary condition it is assumed that no mass transfer occurs across the interface, thus,

$$\mathbf{n} \cdot \mathbf{u} = 0$$

(4) Static contact lines, where capillary forces, momentum and viscous forces balance each other.

(5) Moving and leaking wall. The leakage is modeled through the control points.

### ***10.2.3 Verification of the Numerical Method***

To investigate the accuracy of the suggested modeling approach a custom designed roll feed imaging system (RFIS) is used to conduct the experimental studies. The RFIS is a roll-to-roll coating setup as shown in Figure 10.4. Using RFIS, carbon paper GDLs are coated and the penetration depth versus the coating speed is measured.

The RFIS is equipped with a slot die, a vision system, and has adjustable web speed, coating gap ( $H$ ) control, and an inline imaging capability. RFIS is equipped with two sets of camera/microscope systems positioned at the bottom and side of the slot die. Cameras are Olympus UC30 with a 12-bit 1/1.8" CCD color sensor capable of 7 frames per second at the full resolution of 2080×1544 and C-mount lens connector, and equipped

with the image acquisition software. The coating gap is set to the desired value by adjusting the distance between the slot die and the substrate using a vertical rail system with worm gears. The coating solution is pumped onto the moving substrate using a Nitrogen pressurized tank and forms a thin film on the top of it.

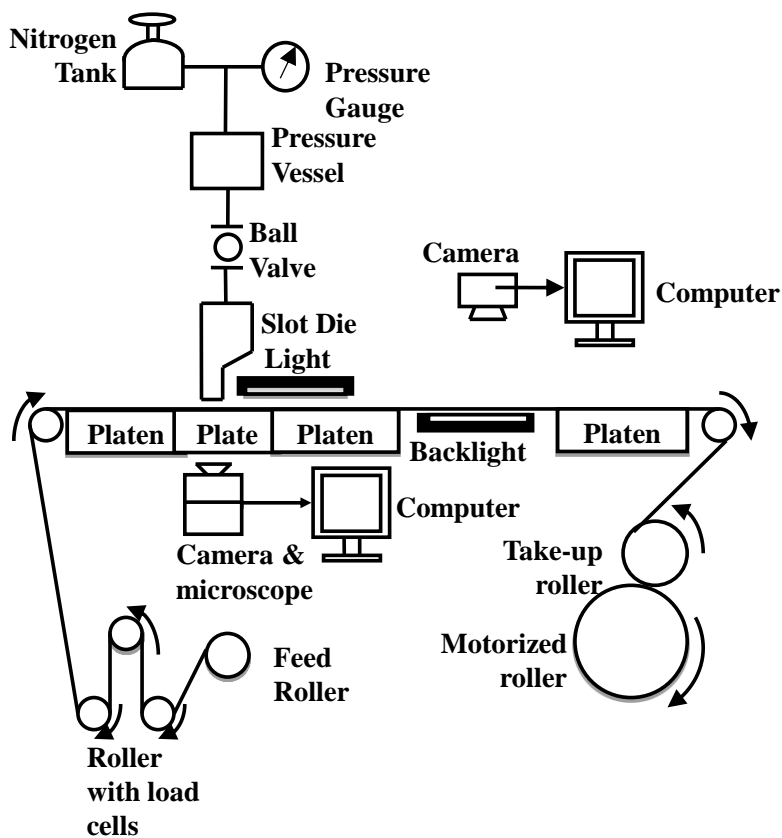


**Figure 10.4** The schematic of the experimental setup.

In this study glycerin as purchased from Sigma Aldrich, is used as the coating solution. The material properties of glycerin are given in Table 10.1. Surface tension of glycerin is measured by Pendent method using Ramé-hart Goniometer Model 250. Viscosity of the solution is measured using an ARES rheometer by performing steady

shear rate sweep using a parallel plate configuration.

**Table 10.1** Material properties of glycerin.

Density (kg/m <sup>3</sup> )	Viscosity (Pa.s)	Surface tension (N/m)
1260	0.91	0.063

Since slot die coating technique is a premetered coating method, if the web is not porous, the thickness of the coated film can be easily found from the mass conservation. To measure the penetration depth the thickness of the coated film on top of the porous web is measured and the difference between the measured thickness and the thickness of the film over impermeable substrate is considered as the penetration depth. Hence, the average penetration depth is actually measured.

### **10.3 Micro Scale Simulation of Penetration Process**

Finding the pressure distribution from the macro scale model, the transient pressure boundary condition is inserted to the computational domain shown in Figure 10.5. The 2D cross sections of the virtually generated porous media are used for the micro scale simulations. The size of the computational domain is selected as 200 $\mu\text{m}$ ×200 $\mu\text{m}$ . To model the interface between the porous substrate and the coating bead a reservoir with the height of 20  $\mu\text{m}$  is placed above the 2D cross sections of the porous structure, as shown in Figure 10.5.

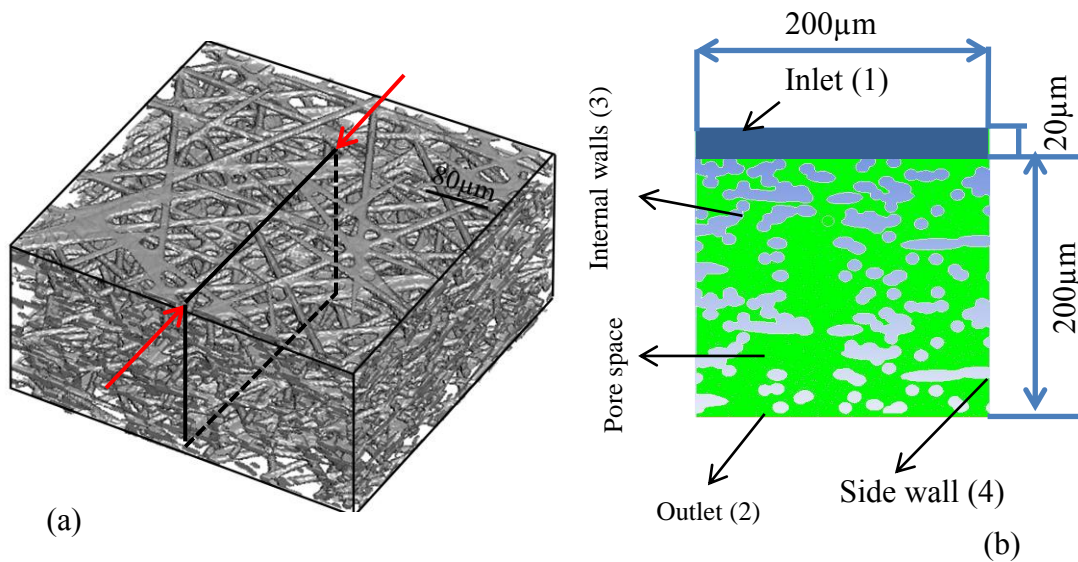


**Figure 10.5** (a) The cross section of the virtually generated microstructure (b) 2D view.

### 10.3.1 Boundary Conditions of the Micro Scale Simulation

The schematic of the computational domain, its boundary conditions and the size of the domain are shown in Figure 10.5. The boundary conditions used for the simulation are

- (1) Pressure inlet, where a transient pressure boundary condition found from macro scale simulation is applied. The transient boundary condition is inserted as a user defined function (udf) as follow

```
#include "udf.h"

DEFINE_PROFILE (unsteady_pressure, thread, position)
{
    face_t f;
    real t = CURRENT_TIME;
```



```

begin_f_loop (f, thread)
{
    F_PROFILE (f, thread, position) = function defining P versus time;
}
end_f_loop (f, thread)
}

```

- (2) Outlet, where the pressure is set as the atmospheric pressure. Thus, zero gauge pressure i.e.,  $P_g = 0$  is applied.
- (3) Internal wall, where no slip boundary condition is applied.
- (4) Side wall, where it is assumed that the penetrating coating solution cannot exit the domain.

It is assumed that the reservoir located at the top of the porous domain is always filled with the coating solution and the porous domain is initially filled with air.

### 10.3.2 Governing Equations

The two phase flow field is solved by volume of fluid (VOF) model embedded in FLUNET ANSYS 14 software. The momentum and mass conservation equations are given by Equation 10.3 and 10.4. However, in VOF the surface tension force is modeled as

$$\mathbf{F}_{st} = \sigma \frac{\kappa \nabla \alpha_{liquid} (\alpha_{air} \rho_{air} + \alpha_{liquid} \rho_{liquid})}{0.5(\rho_{air} + \rho_{liquid})} \quad (10.7)$$

where  $\alpha$  is the volume fraction and is the same as level set function,  $\varphi$ .  $\kappa$  is the curvature

of the interface.

## **10.4 Summary**

To study the penetration of coating solution into a porous medium with irregular topology, such as fibrous porous structures, it is required to develop a methodology that couples the macro scale coating bead to the micro scale penetration process. The amount of penetration mainly depends upon the pressure field in the coating bead and the capillary forces. The convective-driven pressure field is determined by the macro scale flow field, while the capillary forces are mainly due to the micro scale features of the porous structure. Thus, to fully investigate the penetration process, a multi scale approach is introduced.

In this chapter the methods developed to solve the penetration process both at the macro and micro scales are described, the computational domains, the corresponding boundary conditions and the implemented numerical approaches along with the governing equations are presented.

To verify the accuracy of the suggested modeling approach, the numerical results of the penetration depth will be compared with the experimental data in Chapter 11. The setup used for the experimental study of the coating of a porous substrate is introduced and the method of measuring the penetration depth is discussed.

# 11. VIRTUAL CHARACTERIZATION OF COMPLEX POROUS MEDIA, RESULTS

In this chapter, penetration of a coating solution into a porous web during the slot die coating procedure is studied. The numerical predictions are compared to experimental data and the results obtained from an analytical model developed by Ding et al. [16]. Implementing the modeling approach discussed in Chapter 10, effects of coupling of flow in the coating bead and porous web on the pressure distribution is investigated. The pressure distribution of the coupled flow field is used as a transient pressure inlet boundary condition. Then, the dependency of the penetration depth upon the operating conditions i.e., coating gap ( $H$ ), slot gap ( $W$ ), flow rate ( $Q$ ), coating speed ( $u_w$ ), viscosity ( $\mu$ ) and surface tension ( $\sigma$ ) of the coating solution is investigated.

## 11.1 Coupling of Flow Field in the Coating Bead and Porous Media

The macro scale slot die coating process is simulated for three cases, using the operating conditions listed in Table 11.1. In the first case, the porosity of the web is ignored and the pressure distribution is found assuming the web as a solid substrate. For the second case, the pressure distribution is found when the porosity of the web is taken into account, but the capillary forces in the porous domain are ignored. As described in Chapter 10, the flow in the porous web is modeled as a leaking flow from the web. For the last case, the pressure distribution is found considering the porosity of the web and the capillary forces in the porous web. As discussed in Chapter 10, to model the Capillary forces it is assumed that the flow front experiences a resistance equal to the capillary

forces while passing through the porous web.

**Table 11.1** Setting for determining the pressure distribution over the porous web.

Parameter	$H(\mu\text{m})$	$W(\mu\text{m})$	$Q(\text{m}^3/\text{s})$	$u_w(\text{m/s})$	$\mu(\text{Pa}\cdot\text{s})$	$K(\text{m}^2)$	$\varepsilon$	$P_c(\text{Pa})$
Setting	115	250	$6 \times 10^{-7}$	$3 \times 10^{-3}$	0.91	$8.8 \times 10^{-12}$	0.8	-2500

Solving the flow field, the pressure distribution over the web is extracted from the numerical simulation at steady state. The pressure distribution for these three cases is shown in Figures 11.1 and 11.2. As illustrated in the figures, coupling of the coating bead and porous web has strong effect on the pressure distribution. Since penetration of coating solution into the web mainly depends upon the pressure field, inaccurate prediction of the pressure results in an inaccurate approximation of penetration depth.

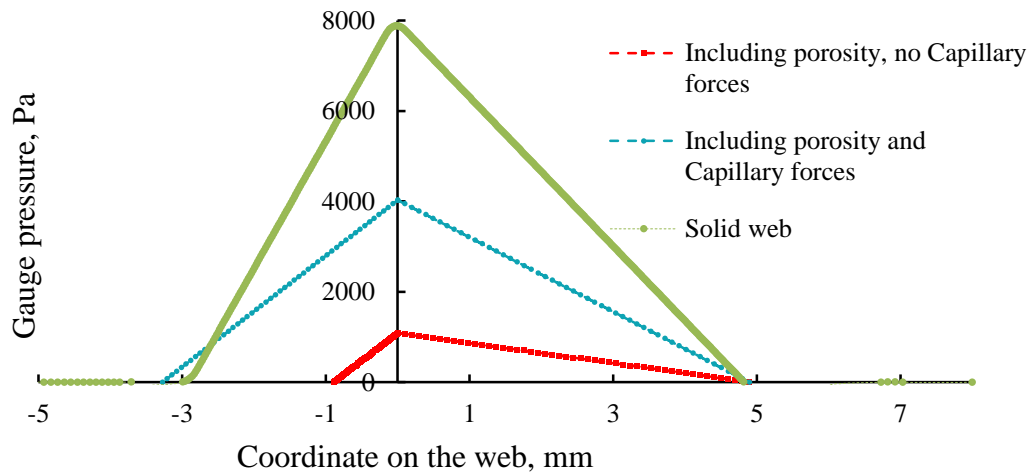


**Figure 11.1** The pressure distribution over the web, ignoring porosity of web and capillary forces, including porosity of the web, and considering porosity of the web and capillary forces.

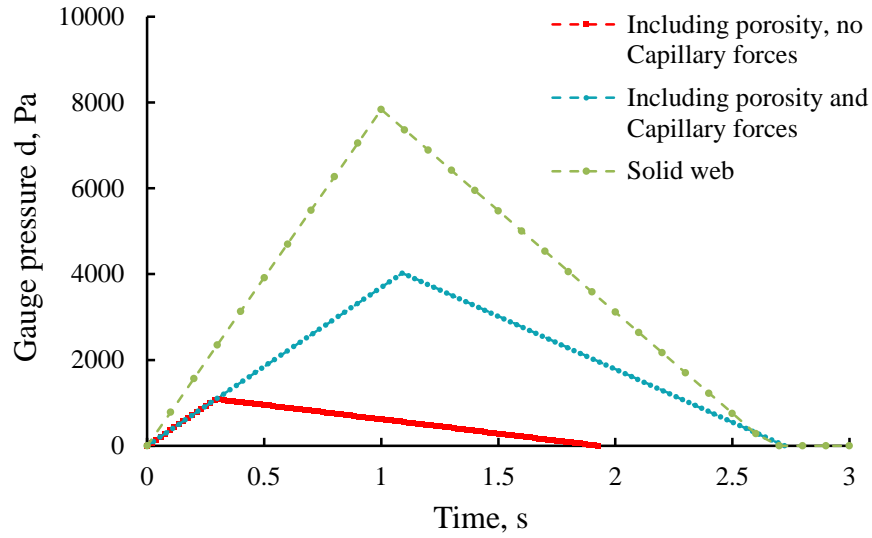


**Figure 11.2** The transient pressure inlet boundary condition for the micro scale domain.

## 11.2. Effect of Operating Conditions on the Penetration of Coating Solution into the Porous Web

To study the effect of the operating conditions on the penetration depth the transient pressure boundary condition is extracted from macro scale simulations and implemented in the 2D cross sectional computational domain for the settings listed in the Table 11.2 through 11.5. The average volume fraction of the coating solution ( $\alpha_{liquid}$ ) in the porous domain is computed at each time step and stored. Knowing  $\alpha_{liquid}$ , the penetration depth ( $h$ ) at each time step is found from Equation 11.1

$$h = \frac{\alpha_{liquid}}{\varepsilon} L \quad (11.1)$$

where  $L$  is the size of the domain and  $\varepsilon$  is the porosity of the computational domain. The final penetration depth is found when the simulation reaches steady state.

To verify the accuracy of the suggested simulation approach, the numerically computed values of penetration depth are compared to the result found from the experiments and the analytical model proposed by Ding et al. [16]. The developed analytical model is based on the lubrication theory and determines the penetration depth due to the convective driven pressure field in the coating bead. Thus, in the VOF numerical simulations wall adhesion is ignored. The inlet pressure boundary condition, which includes the effect of porosity of the web, is extracted from the macro scale simulation and utilized in the micro scale computational domain.

One of the important parameters in the slot die coating process is coating gap ( $H$ ). Didari et al. [164] showed that in the slot die coating of a solid web for mildly viscous Newtonian and non-Newtonian shear thinning fluids, increasing the coating gap results in air entrainment at lower coating speed. However, the effect of the coating gap on the slot die coating of a porous substrate has not been investigated. Since, the focus of current study is on the penetration process, the effect of the coating gap on the penetration depth is investigated. The numerical simulations are conducted for various  $H$  for the operating conditions listed in Table 11.2.

The change in the penetration depth versus the change of coating gap is shown in Figure 11.3. As shown in the figure, increasing the coating gap decreases the penetration depth. The transient pressure experienced by the web for different coating gaps is shown in Figure 11.4. As illustrated in the figure, at larger gaps lower pressure is exerted on the web, hence, the penetration depth is smaller. As shown in Figure 11.3, as  $H$  increases the pressure profile becomes less sensitive to the change of the coating gap. This behavior

leads to pseudo convergence behavior depicted in Figure 11.3.

**Table 11.2** Settings for simulation of penetration depth versus coating gap ( $H$ ).

Parameter	$W$ ( $\mu\text{m}$ )	$Q$ ( $\text{m}^3/\text{s}$ )	$u_w$ ( $\text{m/s}$ )	$K$ ( $\text{m}^2$ )	$\varepsilon$	$\mu$ ( $\text{Pa}\cdot\text{s}$ )	$\sigma$ ( $\text{N/m}$ )	$\rho$ ( $\text{kg}\cdot\text{m}^3$ )
Setting	250	$6\times 10^{-7}$	$3\times 10^{-3}$	$8.8\times 10^{-12}$	0.8	0.91	0.063	1260

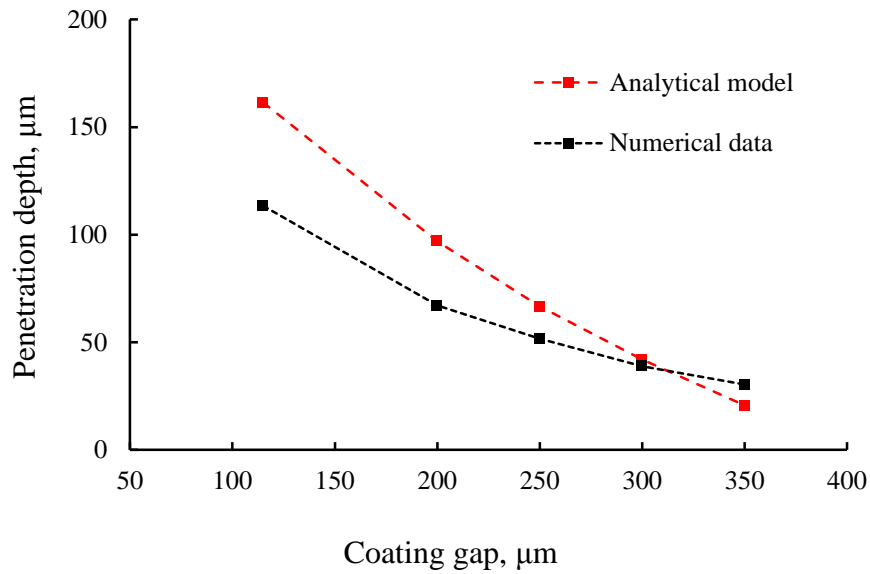


**Figure 11.3** Penetration depth versus coating gap ( $H$ ).

The penetration depths found from the analytical model are also shown in Figure 11.3. As depicted in the figure, the numerical and analytical predictions are close (with the maximum error of 29%). However, at smaller coating gap larger discrepancies exist between numerical and analytical results. In the analytical model the surface tension forces are neglected. Thus, penetration depth continuously decreases with decreasing  $H$ . However, in the numerical simulations the surface tension forces are considered, so the penetration depth reaches to a steady state condition at large coating gap. The difference

between the numerical and analytical results at smaller gaps are due to the difference between the topology of the cross section of the RVE used in the micro scale computational domain and the actual porous media modeled with the Darcy's law in the analytical model.

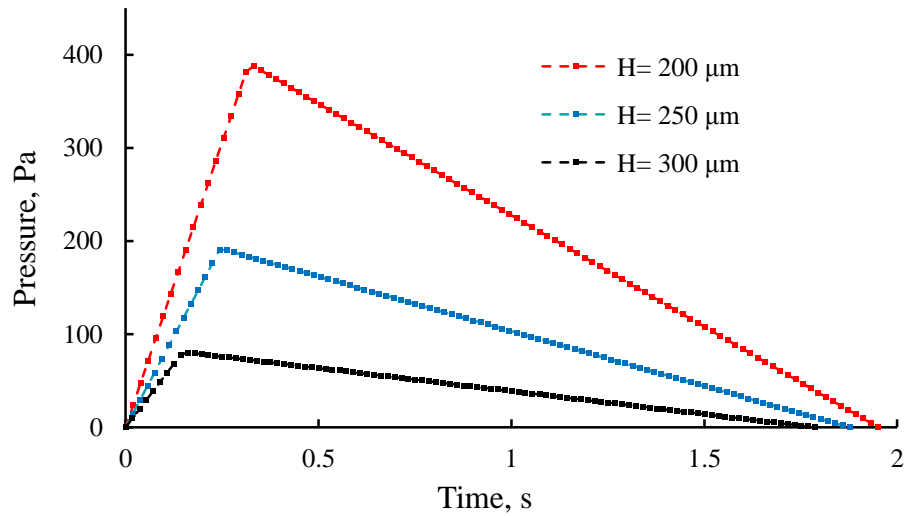


**Figure 11.4** The transient pressure profile versus coating gap ( $H$ ).

The time dependent behavior of the penetration depth for various coating gaps is shown in Figure 11.5. As explained in Chapter 10, to determine the penetration depth it is assumed that the penetration mainly takes place in region (I) during slot die coating and it reaches close to its final value within this region. As illustrated in Figure 11.5, the penetration depth for the coating gaps between 200 to 300  $\mu\text{m}$  reaches steady state condition.



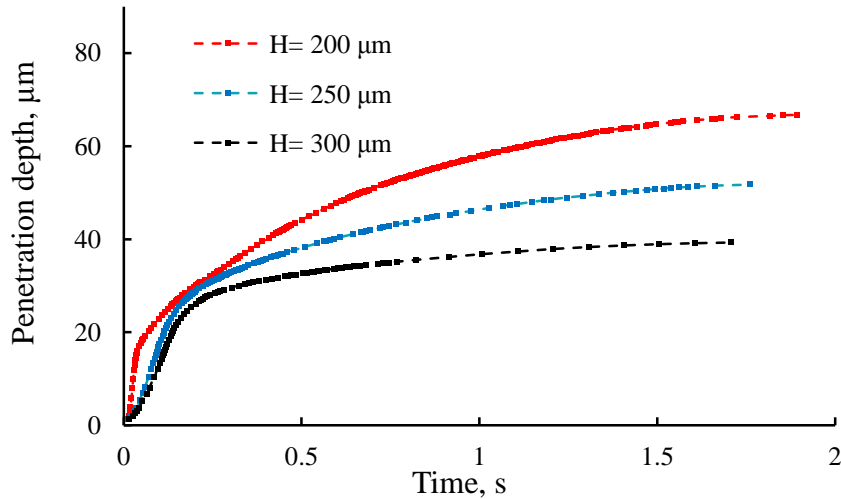


**Figure 11.5** Transient Penetration depth profile versus coating gap ( $H$ ).

To study the effect of slot gap ( $W$ ), macro and micro scale simulations are conducted for the operating condition listed in Table 11.3. For this purpose, the flow rate of coating solution into the die ( $Q$ ) is kept constant, but the slot gap is changed. In this case, the velocity of the coating solution entering the slot die changes. The change of the penetration depth versus the change of the slot gap is shown in Figure 11.6. As shown in the figure, the change in penetration depth is insignificant. Thus, it is concluded that the penetration depth is not a function of the slot gap, or the velocity of the coating solution at the inlet of the slot die. Since the coating gap during the slot die coating is small i.e., on the order of micrometers, at the steady state, the flow field in the coating bead depends heavily upon the capillary, momentum and viscous forces near the web. Thus, changing the inlet velocity while keeping the substrate speed and flow rate constant, does not affect the pressure in the flow field and the resultant penetration depth. The penetration depths found from the analytical model are also depicted in Figure 11.6. As shown in the figure, the numerical simulation and analytical model show that the penetration depth does not

depend upon the slot gap. As mentioned earlier, the discrepancy between the numerical predictions and the analytical data can be due to the difference between the topology of the 2D microstructure and the actual porous media.

**Table 11.3** Settings for simulation of penetration depth versus slot gap ( $W$ ).

Parameter	$H(\mu\text{m})$	$Q (\text{m}^3/\text{s})$	$u_w (\text{m/s})$	$K (\text{m}^2)$	$\varepsilon$	$\mu (\text{Pa}\cdot\text{s})$	$\sigma (\text{N/m})$	$\rho (\text{kg}\cdot\text{m}^3)$
Setting	115	$6 \times 10^{-7}$	$3 \times 10^{-3}$	$8.8 \times 10^{-12}$	0.8	0.91	0.063	1260

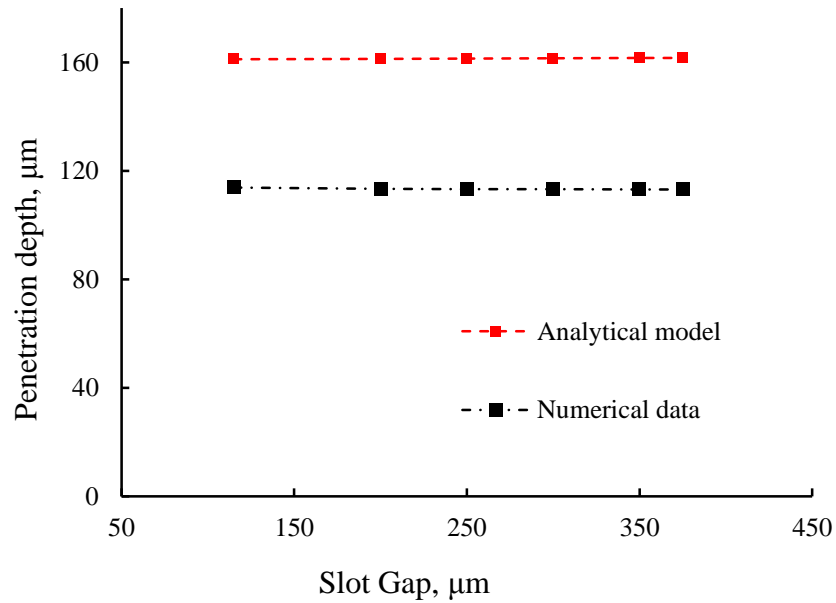


**Figure 11.6** Penetration depth versus coating gap ( $H$ ).

To study the effect of flow rate ( $Q$ ) simulations are conducted for the settings given in Table 11.4. The numerical predictions of the penetration depth are presented in Figure 11.7. As shown in the figure, increasing the flow rate increases the penetration depth. Because the coating speed is kept constant while changing the flow rate, at higher

flow rates the thickness of the film formed above the substrate increases and consequently the pressure on the web increases. Thus, the penetration depth increases as flow rate increases.

**Table 11.4** Settings for simulation of penetration depth versus Flow rate ( $Q$ ).

Parameter	$H$ ( $\mu\text{m}$ )	$W$ ( $\mu\text{m}$ )	$u_w$ (m/s)	$K$ ( $\text{m}^2$ )	$\varepsilon$	$\mu$ (Pa.s)	$\sigma$ (N/m)	$\rho$ ( $\text{kg.m}^3$ )
Setting	115	250	$3 \times 10^{-3}$	$8.8 \times 10^{-12}$	0.8	0.91	0.063	1260

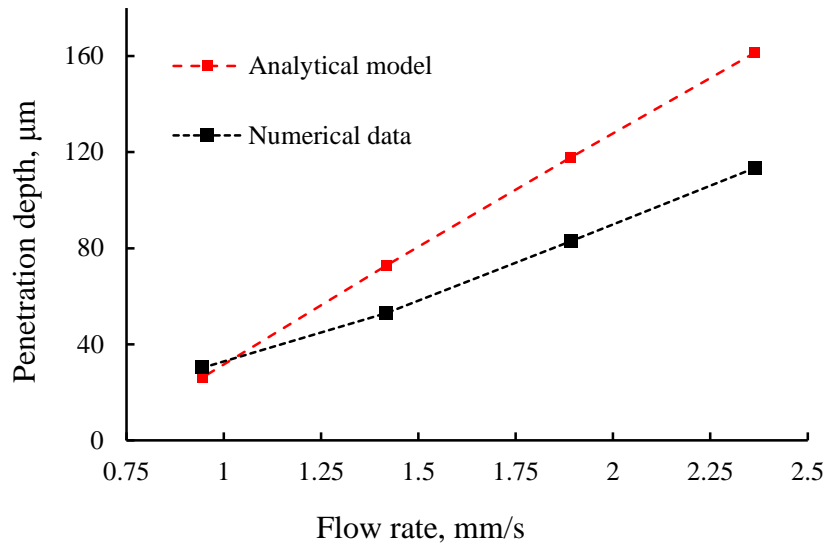


**Figure 11.7** Penetration depth versus Flow rate ( $Q$ ).

As shown in Figure 11.7, numerical predictions and the results found from the analytical model have the same trend. However, due to the limitation of the analytical model at larger flow rates larger discrepancies exist between the numerical and analytical results. The analytical model is developed assuming that the materials are coated at relatively high coating speed [16]. Because the coating speed is constant, at the higher

flow rates this assumption is not valid. Thus, the analytical model fails to precisely predict the penetration depths. By decreasing the flow rate the pressure exerted on the web also decreases. But due to surface tension forces, the penetration depth should approach a final value at the lower flow rates. As shown in Figure 11.7, the numerical simulation is able to capture this behavior.

To study the effect of the coating speed on the penetration depth the numerical simulations are conducted for the operating conditions listed in Table 11.5 and the results are shown in Figure 11.8. As illustrated in the figure, as coating speed increases, the thickness of the film formed at the top surface of the web and subsequently the pressure exerted on the coating bead decreases. Thus, the penetration depth also decreases

To verify the accuracy of the numerical simulations, the numerically predicted values of the penetration depth are compared with the experimental data and the results of the analytical model. The coating solution used in the numerical and experimental studies is glycerol. The porous web used in the experiments is Toray carbon paper. As shown in Figure 11.8, the numerical results follow the same trend as the experimental data and the results from the analytical model. The difference between the numerical predictions and the analytical and experimental results is smaller than 28% and 17%, respectively. Due to neglecting the surface tension forces in the analytical model and also the hydrophobicity of glycerol, the experimentally measured penetration depths are smaller than results from analytical model. The discrepancy between the experimental measurements and the numerical predictions can be attributed to the difference between the topology of the virtual 2D microstructures and actual porous media.

**Table 11.5** Settings for simulation of penetration depth versus coating speed ( $u_w$ ).

Parameter	$H(\mu\text{m})$	$W(\mu\text{m})$	$Q (\text{m}^3/\text{s})$	$K (\text{m}^2)$	$\varepsilon$	$\mu (\text{Pa}\cdot\text{s})$	$\sigma (\text{N}/\text{m})$	$\rho (\text{kg}\cdot\text{m}^3)$
Setting	115	250	$6 \times 10^{-7}$	$8.8 \times 10^{-12}$	0.8	0.9	0.063	1260

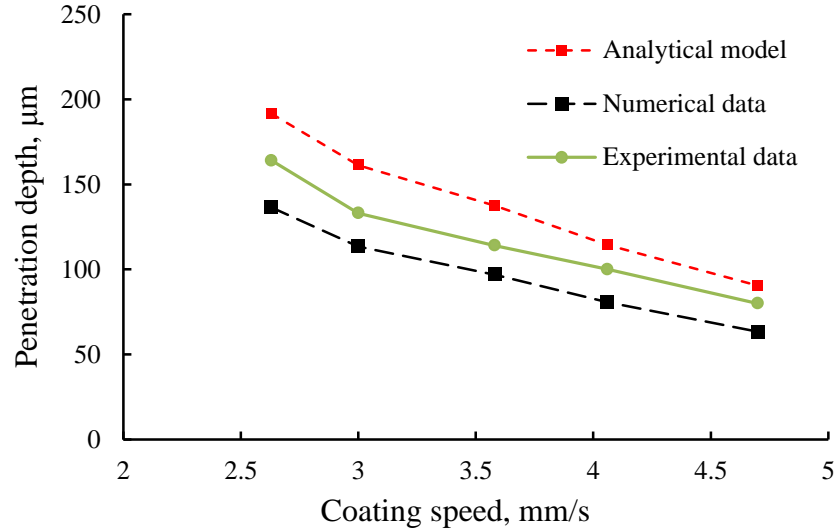


**Figure 11.8** Penetration depth versus coating speed ( $u_w$ ).

### 11.3 Effect of Viscosity and Surface Tension of the Coating Solution on the Penetration into the Porous Web

To study the effect of the viscosity of the coating solution on the penetration process the numerical simulations are conducted for the operating conditions listed in Table 11.6. The transient pressure inlet boundary condition including the effect of the porosity of the web is extracted from the macro scale simulations, shown in Figure 11.9. As illustrated in the figure, increasing the viscosity increases the pressure exerted on the web. According to the lubrication theory, the change in pressure in the coating bead

during the slot die coating is given by:

$$\frac{\partial P}{\partial x} \sim \mu \frac{\partial^2 u}{\partial y^2}$$

where  $P$ ,  $x$ ,  $\mu$ ,  $u$  and  $y$  are pressure, coordinate along the web, viscosity, speed in the  $x$  direction and the coordinate along the film thickness, respectively. Because coating speed and film thickness are kept constant, according to the lubrication theory increasing the viscosity will increase the pressure gradients in the coating bead.

**Table 11.6** Settings for simulation of penetration depth versus viscosity ( $\mu$ ).

Parameter	$H(\mu\text{m})$	$W(\mu\text{m})$	$Q(\text{m}^3/\text{s})$	$u_w(\text{m/s})$	$K(\text{m}^2)$	$\varepsilon$	$\sigma(\text{N/m})$	$\rho(\text{kg}\cdot\text{m}^3)$
Setting	115	250	$6 \times 10^{-7}$	$3 \times 10^{-3}$	$8.8 \times 10^{-12}$	0.8	0.063	1260

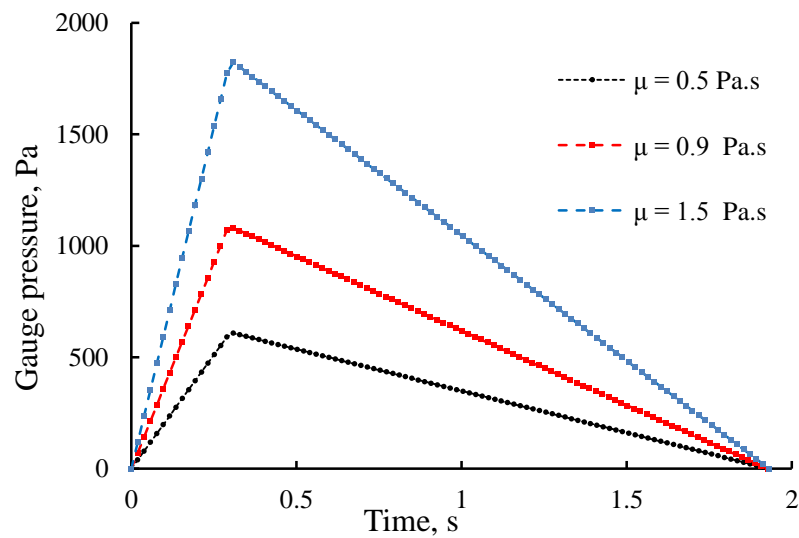


**Figure 11.9** Transient pressure inlet boundary condition versus viscosity ( $\mu$ ), for a macro scale simulation.

To predict the penetration depth the numerical simulations are conducted assuming that the coating solution completely wets the internal surfaces of the porous media and considering the wall adhesion in the VOF model. The time dependent behavior of the penetration depth versus the change in coating solution viscosity is shown in Figure 11.10. As shown in the figure, increasing the viscosity decreases the penetration depth. Although a larger pressure is generated in the coating gap when coating solution has higher viscosity, but due to the higher amount of viscous forces exerted to the penetrating solution, the penetration depth decreases.

Using the analytical model, the penetration depth for the listed operating conditions is found and shown in Figure 11.11. As illustrated in the figure, the effect of viscosity on the penetration process cannot be studied using the analytical model. Due to neglecting the capillary forces, the coating solution does not face any resistance while penetrating into the porous structure. Thus, low and highly viscous solutions behave the same.

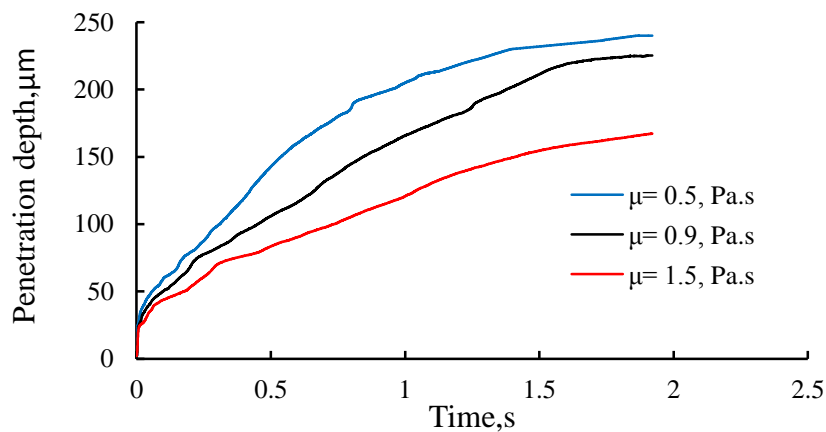


**Figure 11.10** Time dependent behavior of penetration depth versus viscosity of coating solution ( $\mu$ ).

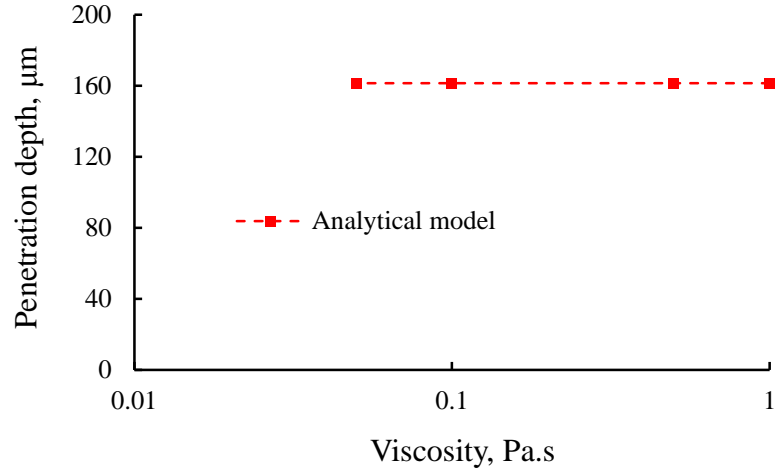


**Figure 11.11** Penetration depth versus viscosity of the coating solution ( $\mu$ ), found from analytical model.

To study the effect of surface tension during the penetration process, the numerical simulations are conducted for the operating conditions given in Table 11.7. The transient pressure profile, which includes the effect of the porosity, is extracted and used as the pressure inlet boundary condition in the micro scale simulations. The numerically determined transient penetration depth profiles are shown in Figure 11.12. As shown in the figure, as surface tension increases the penetration depth increases and capillary forces increases dragging larger amounts of coating solution into the porous web. Since the analytical model neglects the surface tension forces, it cannot be used for the verification of the suggested numerical approach.

**Table 11.7** Settings for simulation of penetration versus surface tension ( $\sigma$ ).

Parameter	$H(\mu\text{m})$	$W(\mu\text{m})$	$Q (\text{m}^3/\text{s})$	$u_w (\text{m/s})$	$K (\text{m}^2)$	$\varepsilon$	$\mu (\text{Pa.s})$	$\rho (\text{kg.m}^3)$
Setting	115	250	$6 \times 10^{-7}$	$3 \times 10^{-3}$	$8.8 \times 10^{-12}$	0.8	0.5	1260



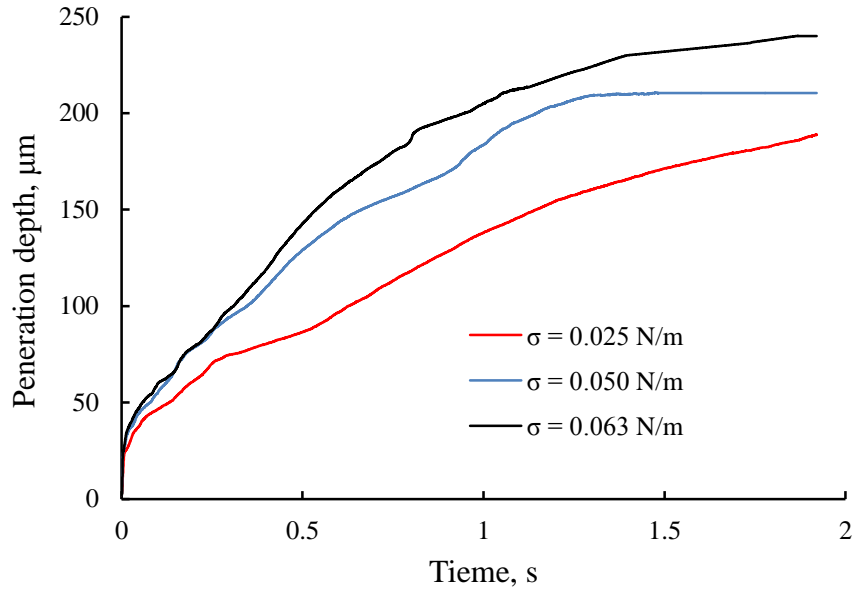


**Figure 11.12** Penetration depth versus viscosity of coating solution ( $\sigma$ ).

#### 11.4 Summary

In this chapter, the penetration of the coating solution into the porous web during the slot die coating process is studied. To accurately estimate the penetration depth a multi scale approach is developed that couples the flow fields in the macro scale coating bead and the virtually reconstructed microstructure of the porous web. To track the coating solution front inside the porous substrate, the pressure distribution over the porous web is extracted from the coating bead and inserted as a transient pressure inlet boundary condition into the virtual microstructures. It is found that the pressure boundary condition, which determines the penetration depth, heavily depends upon the precise coupling of the macro scale and micro scale flow fields.

The effects of coating solution properties i.e., viscosity and surface tension and processing conditions i.e., coating speed, coating gap, slot gap and coating flow rate on

the penetration depth are investigated. It is found that increasing viscosity, coating speed and coating gap decreases the penetration depth, while increasing surface tension and flow rate increases the penetration depth. It is shown that the penetration process is not sensitive to the change of the slot gap if the flow rate is kept constant.

To verify the accuracy of the numerical simulations the penetration depths are found numerically, using the microstructures developed by generalized PS model. The numerical predictions are compared with the results found from an existing analytical model and the experimentally measured data. It is shown that the developed numerical procedure can predict the behavior of the penetration process versus the change of the operating conditions. However, some discrepancies are observed between the numerical and analytical results. The difference between the numerical approximations and results found from analytical model is attributed to the deviation of the topology of the 2D cross section of the virtual microstructures used in this study and the actual porous media.

The developed numerical procedure is able to predict the change in the penetration depth with respect to the viscosity and surface tension of the coating solution. The analytical model cannot predict the change of the penetration depth versus the surface tension and viscosity of the coating solution since these factors are overlooked in the analytical model. Also, due to considering the surface tension forces in the numerical procedure, the developed numerical procedure is able to predict the penetration depth at higher coating speed and flow rate more precisely.

## 12. CONCLUSION AND CONTRIBUTIONS

Fibrous porous media have become important light-weight and multi-functional composite materials in textile, energy generation, filtration, tissue engineering, and other applications. Yet there is a lack of integrated and easy-to-use computational design tools for engineers to design and optimize their properties. Hence, in this research a framework is developed so that the design and manufacture of these materials can be conducted in a virtual environment with reduced time and cost. Specifically, modern computational tools are integrated in the design and manufacturing processes to replace the ongoing trial and error approaches.

The proposed modeling and simulation framework for design of fibrous porous media is shown in Figure 12.1. Various design and process parameters can be the inputs to generate fibrous and composite models. The virtually constructed geometrical models of porous structures are utilized to predict transport properties. These predicted properties are used as design targets.

The developed design methodology can also be used as a characterization tool for the actual porous media. As shown schematically in Figure 12.2, implementing an image based technique the voxel representation of an existing porous medium can be extracted. Using the voxel representation of the porous medium, its morphological and transport properties are found via the developed numerical approaches, presented in this work.

To characterize the complex porous structure i.e., the porous structure with a coated layer, the penetration of a coating solution into the porous web during slot die coating process is virtually simulated. Since the final properties of the resultant complex composite fibrous medium depend upon the penetration of the coating solution into its pore space, the penetration depth under various processing conditions is found.

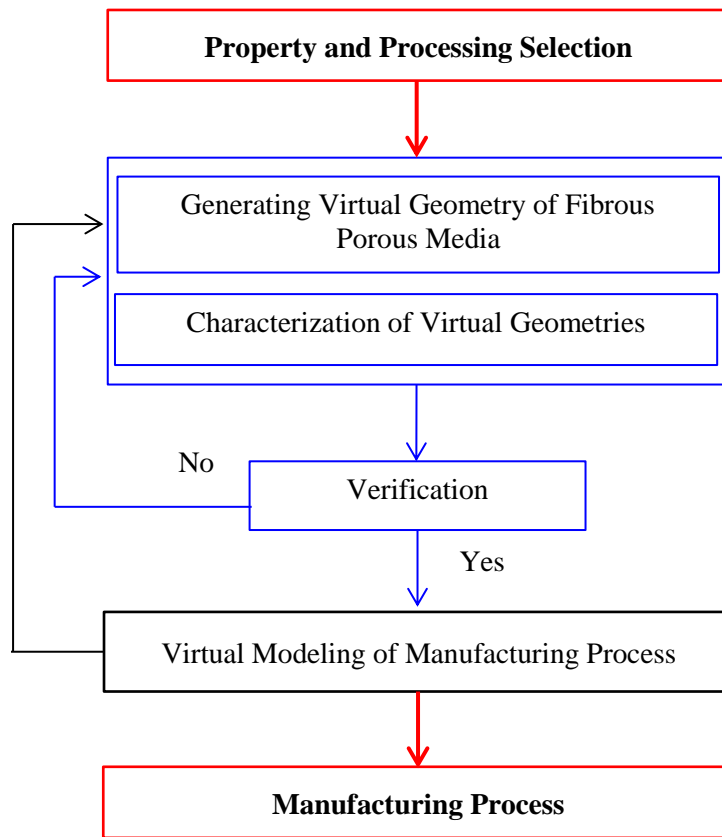


**Figure 12.1** The framework for design of fibrous porous media.

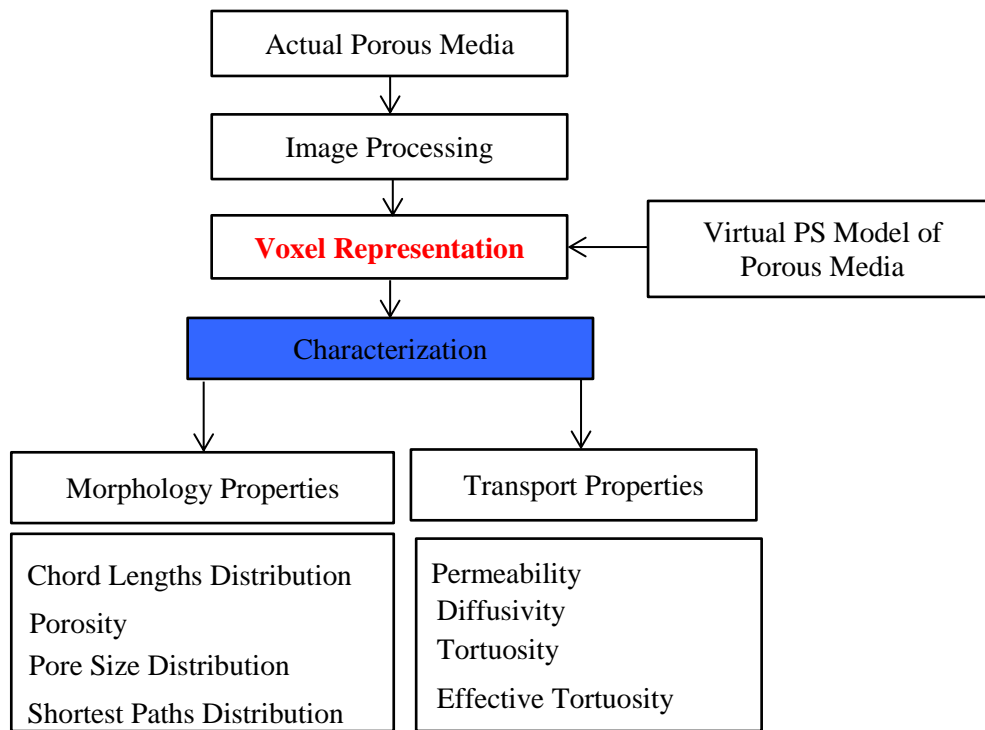


**Figure 12.2** The framework for characterization of virtual and actual fibrous porous media.

## 12.1 Conclusions

Based on the observations made in the current study, several important conclusions can be drawn regarding virtual representation of porous media, virtual characterization of porous media and coating of porous media used to fabricate complex porous media as follow.

### 12.1.1 Virtual Representation of Porous Media

The very first step in the design process of porous media is to build geometric models of their structures. However, existing CAD tools and geometric modeling

approaches are not developed for this purpose. The existing geometric modeling approaches cannot handle the high degree of irregularity and complexity in the porous microstructures. Thus, in this research PS modeling approach is modified to construct three main types of fibrous porous media. To model paper structures PS model of a rod shown schematically in Figure 12.3 (a) and described by Equation 12.1 is used.

$$\psi(r) = \sum_{l=1}^L \sum_{m=1}^M \mu_{lm} \cos(2\pi k_l (\mathbf{P}_m^T \cdot \mathbf{r})) = 0 \quad (12.1)$$

To model felt porous media, which have highly curved fibers, the PS model is modified by introducing an extra minor phase. The generalized PS model of a curved fiber, shown schematically in Figure 12.3 (b) and described by Equation 12.2, is used to construct felt structures.

$$\psi(r) = \sum_{l=1}^L \sum_{m=1}^M \mu_{lm} \cos\left(2\pi k_l (\mathbf{P}_m^T \cdot \mathbf{r}) + \sum_{s=1}^S \sum_{t=1}^T u_{lmst} \cos\left(2\pi f r_{lms} (\mathbf{q}_{lmt}^T \cdot \mathbf{r})\right)\right) = 0 \quad (12.2)$$

The woven media are modeled using the generalized PS model with one minor phase term i.e.,  $S = 1$  and  $T = 1$ . As shown in Figure 12.3 (c), it is assumed that due to the external forces the cross section of the fiber is changed.

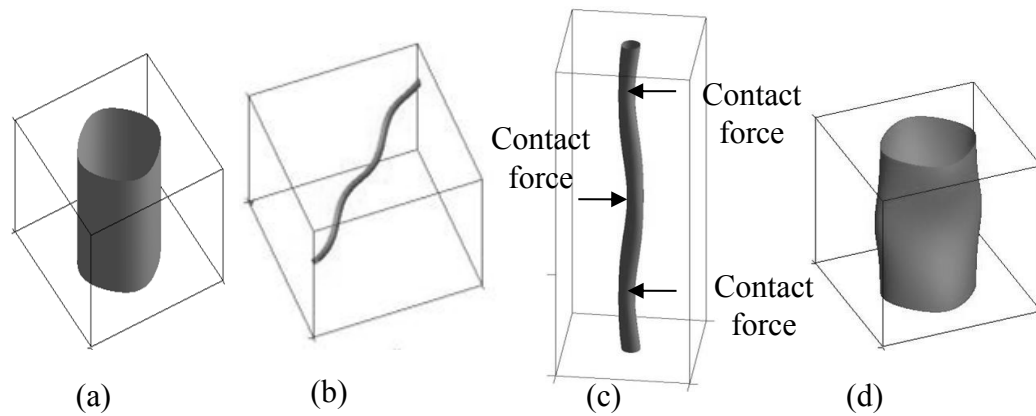


**Figure 12.3** The PS model used for construction of (a) paper, (b) felt, (c) and (d) woven fibrous porous media [152].

Using the PS model of a rod and generalized PS model of a bent rod, the woven, paper and felt GDLs are constructed as shown in Figure 12.4. It is found that although the geometrical modeling of the nonwoven porous structures can generate microstructures that resemble the actual porous media, for higher accuracy additional criteria have to be considered.

Paper and felt porous media have undetermined statistical structures due to the randomness in spatial orientation of each fiber. The random distribution of fibers in the RVE might result in intersecting fibers. Hence, to accurately model a microstructure these intersections have to be reduced or eliminated, which will aid obtaining the optimal spatial distribution and curvature of all. For this purpose, the PS model is coupled with a genetic algorithm optimization (GA) to reduce the intersection of fibers with one another.

It is found that the GA algorithm can reduce the intersection especially for the





To model felt structures, the curvature of the fibers is model by superposition of cosine waves with different amplitudes and frequencies. To determine the number of the superposed waves and their amplitude and frequency two constrains have to be implemented. The intersection of fibers with one another must be minimized and the stored strain energy of the felt microstructure has also to be minimized. It is found that determining the curvature of the fibers and their spatial orientations just by minimizing the intersection volume results in largely curved fibers as given in Table 12.1.

**Table 12.1** The total curvature of fibers in the felt structures.

Porosity	Min of intersection	Min of intersection and strain energy
	Total Curvature	
72	6763	648
78	4920	194

As given in Table 12.1, it is found that the lower the porosity of the felt medium the higher is the curvature of fibers, this is because more fibers are located in the RVE of denser porous medium and, fibers tend to be bent to a higher degree to avoid intersecting with one another.

### ***12.1.2 Virtual Characterization of Porous Media***

Prior to fabrication, virtual models can be used as virtual prototypes to estimate and optimize the performance of fibrous porous media. For instance, using computational fluid dynamics (CFD) analysis, the permeability with respect to the porosity of the

microstructure can be computed. However, to enable systematic design and optimization of porous materials with enhanced performance the interplay between the microstructure and macroscopic transport characteristics has to be studied.

For this purpose, the integration between modeling and simulation in the design process of porous media is crucially important. Existing finite-volume based CFD or finite-element based transport property simulations require mesh generation. Given the high irregularity of the internal structure of porous media, conversion of geometric models to mesh models using the existing methods is a challenging and time-consuming manual task. Thus, in this study a new method of mesh generation is developed that couples the PS modeling and mesh generation procedures. Implementing this method high quality volumetric mesh representations of the porous media are generated in an automated way. Consequently, morphological and transport properties of the porous media that can be used as design targets can be computed.

The set of structural properties of porous media that are discussed in this study includes porosity, pore size, chord length and shortest path distributions. The pore size distribution from the virtual representation of porous media is found by deleting the closed end and dead end pores from the set of spherical pores. As shown in Figure 12.6, this leads to a pore size distribution that has the same trend numerically and experimentally. The discrepancy of the data could be attributed to the sample sizes used in the experimental tests. The test samples are commonly on the order of couple of centimeters while the generated microstructures are in the order of hundreds of micrometers. Generating and characterization of a virtual geometry in this order is

computationally expensive.

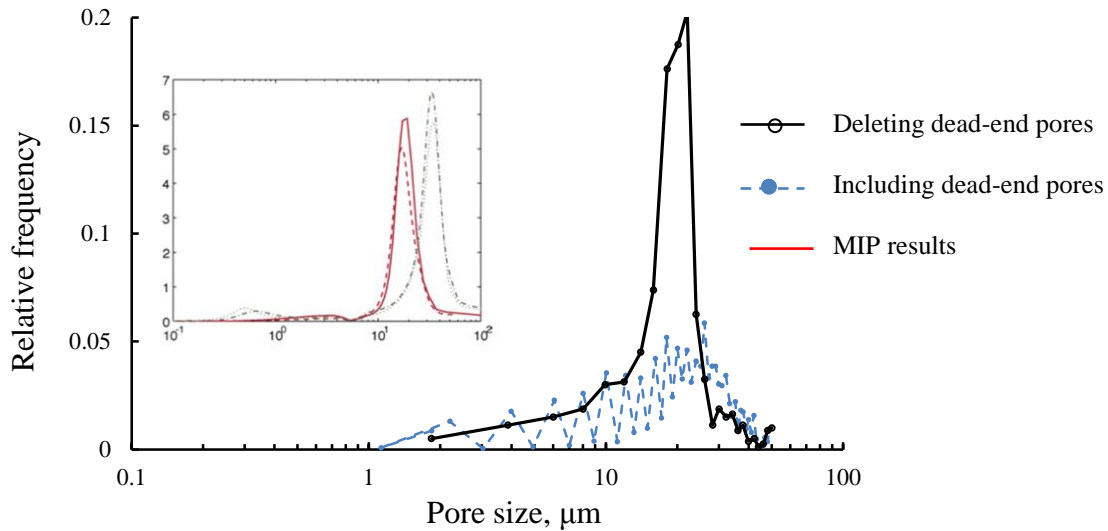


**Figure 12.6** Numerical and experimental pore size distributions [27].

One focus of this study is determining the transport properties of fibrous porous media, because the test case for this study is a gas diffusion layer used in polymer electrolyte membrane fuel cells. However, the proposed modeling and simulation approach is generic and can be similarly applied to any other types of porous structures. The transport properties of the composite paper, felt and carbon cloth GDLs are found and verified against experimental data.

It is found that both permeability and diffusivity of paper and felt structures decrease by reducing the porosity. Permeability of felt structures is higher than the paper media. For felt structures the in-plane and through-plane chord lengths are closer to each other compared to paper porous media. Thus, the pores of felt porous media have rounder cross sections that exert lower resistance to the flow field.

Felt structures have lower diffusivity compared to paper porous media. This behavior is attributed to the higher tortuosity of the felt structure due to their highly curved fibers. Although, for both structures at lower porosities diffusivity is lower, but paper structures show higher sensitivity to the change of porosity. The diffusivity of felt structures also depends on the tortuous paths exist inside their pore space, thus felt shows lower sensitivity to the change of porosity.

### ***12.1.3 Analyzing Complex Porous Media***

To analyze a complex porous structure i.e., the structure with a thin-coated film over a porous medium, the penetration of a coating solution into a porous web has to be studied. In this research the slot die coating process of a porous web is studied. The coating process is simulated numerically and the penetration of the coating solution into the web is determined both numerically and experimentally. To accurately predict the penetration depth, a multi scale approach is developed that couples the macro scale coating bead to the virtually reconstructed micro scale representation of the porous web. The coupling is accomplished by extracting the pressure distribution over the web from the macro scale coating bead simulation and inserting it as a transient boundary condition into the micro scale domain. The effect of various operating conditions on the penetration of coating solution into the porous web is investigated and the results are summarized in Table 12.2. The arrows pointing up represent a proportional behavior while the arrows pointing down represents an inverse relationship between operating conditions and final penetration depth. As given in the Table, increasing the coating

speed, coating gap and viscosity of the coating solution decreases the penetration depth, while increasing flow rate and surface tension of the coating solution increases the penetration into the web. It is also found that slot gap has no effect on determining the penetration depth.

**Table 12.2** Effect of operating conditions on the penetration of the coating solution into the porous web. The arrows pointing up represent a proportional behavior while the arrows pointing down represents an inverse relationship between operating conditions and final penetration depth.

Parameters	Coating speed ( $u_w$ )	Flow rate ( $Q$ )	Coating gap ( $H$ )	Slot opening ( $W$ )	Viscosity ( $\mu$ )	Surface tension ( $\sigma$ )
Penetration depth	↓	↑	↓	NA	↓	↑

## 12.2 Key Contributions

This research offers the manufacturing industry and material engineers an efficient approach to analyze new porous materials in a virtual environment that enables their rational design. The presented framework for the generic modeling and simulation is applicable in many industries, to optimize the design and manufacturing conditions for porous materials.

The expected original contributions of the proposed research in the fundamental science and engineering aspects can be described as below.

### 12.2.1 Fundamental Contributions

This work:

- Provides a physical based geometry generation method for fibrous porous media by integrating the energy of the deformation to the geometrical modeling approach
- Provides a framework to correlate the relationship between the morphological properties of the fibrous porous media and their transport properties for the design of porous media
- Provides a numerical model to analyze the two phase flow in the porous media

### ***12.2.2 Engineering Contributions***

This work:

- Provides a parametric implicit surface modeling approach to generate various types of woven and nonwoven fibrous structures, such as cloth, composite and felt fibrous materials to expose the connectivity between the design and manufacturing phase in the virtual space
- Determines the effect of processing conditions on the penetration of coating solution into the porous media during the slot die coating process used for development of complex porous media

## 13. FUTURE WORK

The future work can be classified into four sections: (1) Modeling non-Fibrous Porous Structures (2) Physics-based Empirical Force Field to Model Deformation of Fibers (3) Mechanical Behavior of Fibrous Porous Media (4) Coating of Porous Media. A brief review of these tentative research topics are explained in this chapter.

### 13.1 Modeling non-Fibrous Porous Structures

Non-fibrous porous media, as shown in Figure 13.1(a), have heterogeneous structure with different pore sizes, and often the difference between their structural features is one or two order of magnitude.

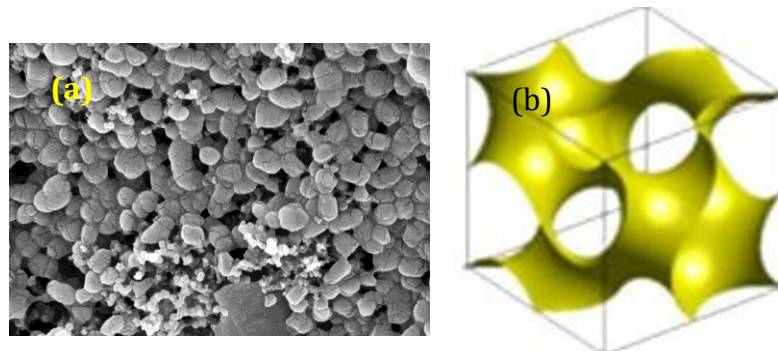


**Figure 13.1** (a) SEM image of micro porous layer, (b) G-type periodic surface model [165].

To fully explore the interplay between the morphology and transport properties of non-fibrous porous media a pore level simulation has to be conducted. However, Due to the spatial variation of the features of non-fibrous porous structures, their design and

overall characterization are challenging tasks. To accurately represent their microstructures a modeling approach has to be developed that combines the statistical approaches with the PS model to build the proper RVE. For this purpose, an implicit surface model such as the G-type PS model shown in Figure 13.1(b) can be used. Different G-type PS models with statistically defined iso-values should be inserted into the RVE. However, to insure the connectivity of the surfaces an interpolation approach needs to be developed. The size of RVE, the utilized PS element, its statistical distribution and the connectivity of the PS models in the RVE are the questions that need to be explored.

### **13.2. Physics-based Empirical Force Field to Model Deformation of Fibers**

In this study, the effect of forces that fibers exert to one another on the fibers profile is modeled in the form of stored strain energy. The curvature of the fibers is found by implementing a double objective optimization function, which not only minimize the volume of intersection of the fibers but also the amount of stored strain energy. In the physical world, systems tend to stabilize at the configurations with minimum potential energies. This general principle can be used to model the shape deformation of fibers such as yarn and tows in woven fibrous porous media. For this purpose a well-defined function of potential energy for fibers needs to be developed.

During fabrication of fibrous porous media fibers are bent, and the cross-sections are compressed at the contact points. As shown in Figure 13.2(a), when modeling of soft fibers, the fibers should not pass through each other or dangle. Figure 13.2 (b), illustrates that the fibers can bend and their cross sections can deformed while being in contact.



Therefore, other than optimizing cross section of fibers, the total potential energy of assembled fibers should be redefined for realistic modeling. A localized potential energy can be defined by using the Hertzian contact stress model, which determines the stresses developed when two curved surfaces are in contact. The amount of stress depends upon the radii of curvature of the contact point and their modulus of elasticity. More study in this area is needed.

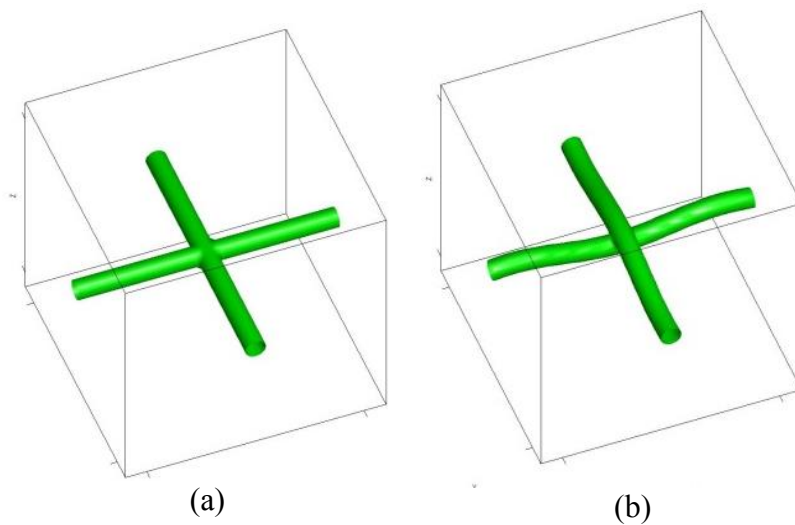


**Figure 13.2** (a) Intersecting fibers, (b) the contacting bent fibers with compressed cross sections [152].

### 13.3 Mechanical Behavior of Fibrous Porous Media

Fibrous porous media, which have high porosity, are most often under compression due to the common assembly forces. The compression of these materials may alter their transport properties. Also the fibrous porous media might mechanically degrade which leads to unpredicted failure of the system. For example, it has been found that the compression of GDLs in the PEMFCs due to the assembly forces changes their

contact resistance, porosity, and permeability and ultimately the performance of PEMFC [166].

Various types of fibrous porous media behave differently under mechanical loads and their mechanical response varies from the mechanical response of non-porous materials. As shown in Figure 13.3, Toray 060 carbon paper and woven GDLs do not respond to the compression force similarly.

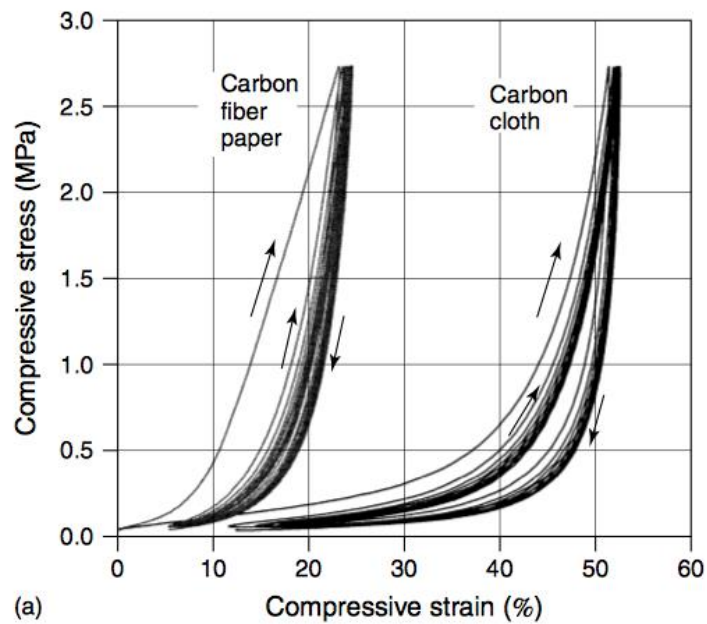


**Figure 13.3** Compression data for Toray 060 carbon paper and woven carbon cloth [166].

Due to the increase of the contact points of the fiber with each other by increasing the compression force a nonlinear response is observed. By having a precise model that can model the contact points of fibers with high accuracy, a better understanding of the coupled mechanical and transport behavior of fibrous porous media can be achieved. This knowledge can be utilized for the purpose of the relevant system performance

enhancement.

### **13.4 Coating of Porous Media**

In this study, the penetration of the coating solution into the porous web during the slot die coating process is studied at macro and micro scales. The effect of the operating conditions i.e., coating speed, flow rate and coating gap on the penetration is investigated. However, the different types of defects and the origin of the defects that might be generated during coating of a porous web have not been studied. The operating conditions in which a defect free film will be coated for the slot die procedure of porous media are not determined.

In this study, it is shown that VOF simulation can predict the penetration depth. But, it is found that it cannot accurately capture the interplay between the topology and the penetration process. Thus, alternative approaches such as the Lattice Boltzmann method (LBM) have to be implemented. Using a 3D LBM formulation the penetration behavior should be studied. However, that might be computationally expensive. The challenge in developing a generic simulation is common in the existing multi-phase LBMs. The density and viscosity ratios between coating fluid and air, which is filling the pores, are large. But, in the existing numerical approaches these ratios are relatively low. Large ratio of density and viscosity results in high gradients at interfaces and numerical instabilities. Thus, developing an accurate numerical approach with lower computational time is necessary.

## REFERENCES

1. Yang, F., et al., *Electrospinning of nano/micro scale poly(l-lactic acid) aligned fibers and their potential in neural tissue engineering*. Biomaterials, 2005. **26**(15): p. 2603-2610.
2. Foitzik, R.C., A. Kaynak, and F.M. Pfeffer, *Conductive poly( $\alpha,\omega$ -bis(3-pyrrolyl)alkanes)-coated wool fabrics*. Synthetic Metals, 2007. **157**(13–15): p. 534-539.
3. Ding, X., et al., *Membrane Electrode Assembly Fabrication Process for Directly Coating Catalyzed Gas Diffusion Layers*. Journal of The Electrochemical Society, 2012. **159**(6): p. B746-B753.
4. Didari, S., et al., *Feasibility of periodic surface models to develop gas diffusion layers: A gas permeability study*. International Journal of Hydrogen Energy, 2012. **37**(19): p. 14427-14438.
5. Dobrego, K.V., et al., *Water purification of organic inclusions by the method of combustion within an inert porous media*. International Journal of Heat and Mass Transfer, 2010. **53**(11–12): p. 2484-2490.
6. Wang, Y., et al., *Self-supporting porous zeolite membranes with sponge-like architecture and zeolitic microtubes*. Advanced Materials, 2002. **14**(13-14): p. 994-997.
7. Huang, F., et al., *Surface functionalization of silk fabric by PTFE sputter coating*. Journal of Materials Science, 2007. **42**(19): p. 8025-8028.
8. Das, D., et al., *Composite nonwovens*. Textile Progress, 2012. **44**(1): p. 1-84.
9. Vafai, K., *Handbook of porous media*. 2009: CRC Press.
10. Caston, T.B., A.R. Murphy, and T.A. Harris, *Effect of weave tightness and structure on the in-plane and through-plane air permeability of woven carbon fibers for gas diffusion layers*. Journal of power sources, 2011. **196**(2): p. 709-716.
11. Mantell, S.C. and G.S. Springer, *Manufacturing process models for thermoplastic composites*. Journal of Composite Materials, 1992. **26**(16): p. 2348-2377.
12. Advani, S.G. and E.M. Sozer, *Process modeling in composites manufacturing*. Vol. 59. 2002: CRC.
13. Ding, X., et al., *Membrane Electrode Assembly Fabrication Process for Directly Coating Catalyzed Gas Diffusion Layers*. Journal of The Electrochemical Society, 2012. **159**(6): p. B746-B753.
14. Ding, X., et al., *A New Fabrication Technique to Manufacture an MEA Using Direct Coating of Nafion® onto Catalyzed GDL*. ECS Transactions, 2010. **33**(1): p. 255-265.
15. Didane, N., S. Giraud, and E. Devaux, *Fire performances comparison of back coating and melt spinning approaches for PET covering textiles*. Polymer Degradation and Stability, 2012. **97**(7): p. 1083-1089.
16. Ding, X., T.F. Fuller, and T.A. Harris, *Fluid penetration into porous media during slot-die coating*.
17. Cui Lab @ Stanford Chemistry. 2013; Available from: <http://www.stanford.edu/group/cui/>.

18. Rehnby, W., *Coating of Textile Fabrics with Conductive Polymers for Smart Textile Applications* 2013.
19. Outlook, A.E., *Energy Information Administration*. United States, 2010.
20. Musti, S., K. Kortum, and K.M. Kockelman, *Household energy use and travel: Opportunities for behavioral change*. Transportation Research Part D: Transport and Environment, 2011. **16**(1): p. 49-56.
21. Vielstich, W., H.A. Gasteiger, and A. Lamm, *Handbook of Fuel Cells: Fuel Cell Technology and Applications*, vol. 4, 2009, Wiley-VCH Verlag GmbH, Weinheim.
22. Hoogers, G., *Fuel cell technology handbook*. 2002: CRC.
23. Jordan, L., et al., *Diffusion layer parameters influencing optimal fuel cell performance*. Journal of power sources, 2000. **86**(1): p. 250-254.
24. Lee, H.-K., et al., *A study on the characteristics of the diffusion layer thickness and porosity of the PEMFC*. Journal of power sources, 2004. **131**(1): p. 200-206.
25. Inoue, G., Y. Matsukuma, and M. Minemoto, *Evaluation of the thickness of membrane and gas diffusion layer with simplified two-dimensional reaction and flow analysis of polymer electrolyte fuel cell*. Journal of power sources, 2006. **154**(1): p. 8-17.
26. Zhao, Q.Q., A. Boxman, and U. Chowdhry, *Nanotechnology in the chemical industry—opportunities and challenges*. Journal of Nanoparticle Research, 2003. **5**(5-6): p. 567-572.
27. Flückiger, R., et al., *Anisotropic, effective diffusivity of porous gas diffusion layer materials for PEFC*. Electrochimica Acta, 2008. **54**(2): p. 551-559.
28. Wargo, E., et al., *Focused Ion Beam Tomography of Diffusion Media for Fuel Cells*. Microscopy and Microanalysis, 2011. **17**(S2): p. 962-963.
29. Wargo, E., et al., *Selection of representative volume elements for pore-scale analysis of transport in fuel cell materials*. Journal of power sources, 2011.
30. Flegler, S.L., J.W. Heckman Jr, and K.L. Klomparens, *Scanning and transmission electron microscopy: an introduction*. Oxford University Press(UK), 1993, 1993: p. 225.
31. Stroschio, J.A., R. Feenstra, and A. Fein, *Electronic structure of the Si (111)  $2 \times 1$  surface by scanning-tunneling microscopy*. Physical review letters, 1986. **57**(20): p. 2579-2582.
32. Kinney, J.H. and M.C. Nichols, *X-ray tomographic microscopy (XTM) using synchrotron radiation*. Annual Review of Materials Science, 1992. **22**(1): p. 121-152.
33. Fredrich, J., B. Menendez, and T. Wong, *Imaging the pore structure of geomaterials*. Science (New York, NY), 1995. **268**(5208): p. 276.
34. Rintoul, M., et al., *Structure and transport properties of a porous magnetic gel via X-ray microtomography*. Physical Review E, 1996. **54**(3): p. 2663.
35. Lee, J., J. Hinebaugh, and A. Bazylak, *Synchrotron X-ray radiographic investigations of liquid water transport behaviour in a PEMFC with MPL-coated GDLs*. Journal of power sources, 2012.
36. Hinebaugh, J., P. Challa, and A. Bazylak, *Accounting for low-frequency synchrotron X-ray beam position fluctuations for dynamic visualizations*. Journal of synchrotron radiation, 2012. **19**(6): p. 0-0.

37. Fishman, Z. and A. Bazylak, *Heterogeneous through-plane distributions of tortuosity, effective diffusivity, and permeability for PEMFC GDLs*. Journal of The Electrochemical Society, 2011. **158**(2): p. B247-B252.
38. Fishman, Z., J. Hinebaugh, and A. Bazylak, *Microscale tomography investigations of heterogeneous porosity distributions of PEMFC GDLs*. Journal of The Electrochemical Society, 2010. **157**(11): p. B1643-B1650.
39. Becker, J., et al., *Determination of material properties of gas diffusion layers: experiments and simulations using phase contrast tomographic microscopy*. Journal of The Electrochemical Society, 2009. **156**(10): p. B1175-B1181.
40. *Geocycles Research Center*. 2013; Available from: <http://www.geocycles.uni-mainz.de/eng/index.php>.
41. *tescan*. 2013; Available from: <http://www.tescan.com/en/other-products/software/3d-tomography>.
42. *sgi*. 2013; Available from: <http://www.sgi.com>.
43. Brown, R., *Theory of airflow through filters modelled as arrays of parallel fibres*. Chemical Engineering Science, 1993. **48**(20): p. 3535-3543.
44. Brown, R., *A many-fibre model of airflow through a fibrous filter*. Journal of aerosol science, 1984. **15**(5): p. 583-593.
45. Herman, P.K., M.J. Lehmann, and Y.K. Velu, *Predicting Initial Pressure Drop of Fibrous Filter Media—Typical Models and Recent Improvements*. Journal of Textile and Apparel, Technology and Management, 2006. **5**(2): p. 1-15.
46. Cheah, C., et al., *Development of a tissue engineering scaffold structure library for rapid prototyping. Part 1: investigation and classification*. The International Journal of Advanced Manufacturing Technology, 2003. **21**(4): p. 291-301.
47. Cheah, C., et al., *Development of a tissue engineering scaffold structure library for rapid prototyping. Part 2: parametric library and assembly program*. The International Journal of Advanced Manufacturing Technology, 2003. **21**(4): p. 302-312.
48. Chow, H., S. Tan, and W. Sze, *Layered modelling of porous structures with Voronoi diagrams*. Computer-Aided Design & Applications, 2007. **4**(1-4): p. 321-330.
49. Kou, X. and S. Tan, *A simple and effective geometric representation for irregular porous structure modeling*. Computer-Aided Design, 2010. **42**(10): p. 930-941.
50. Sudarmadji, N., et al., *Investigation of the mechanical properties and porosity relationships in selective laser-sintered polyhedral for functionally graded scaffolds*. Acta Biomaterialia, 2011. **7**(2): p. 530-537.
51. Peirce, F.T., *The geometry of cloth structure*. The journal of the Textile Institute. Transactions, 1937. **28**: p. 45-96.
52. Hewitt, J., D. Brown, and R. Clarke, *Computer modelling of woven composite materials*. Composites, 1995. **26**(2): p. 134-140.
53. Turan, R. and G. Başer, *Three - dimensional computer simulation of 2/2 twill woven fabric by using B - splines*. The Journal of the Textile Institute, 2010. **101**(10): p. 870-881.
54. Smith, M.A. and X. Chen, *CAD and constraint-based geometric modelling algorithms for 2D and 3D woven textile structures*. J. of Information and Computing Science, 2008. **3**(3): p. 199-214.

55. Sreprateep, K. and E. Bohez, *Computer Aided Modelling of Fiber Assemblies*. Comput. Aided Des. Appl, 2006. **3**(1-4): p. 367-376.
56. Sun, W., F. Lin, and X. Hu, *Computer-aided design and modeling of composite unit cells*. Composites Science and Technology, 2001. **61**(2): p. 289-299.
57. *Applications of carbon nanofibers*. 2013; Available from: <http://sites.duke.edu/chem26hannahnaughton/2012/04/17/scanning-electron-microscopy/>.
58. Liu, H.L. and W.R. Hwang, *Permeability prediction of fibrous porous media with complex 3D architectures*. Composites Part A: Applied Science and Manufacturing, 2012.
59. Schulz, V.P., et al., *Modeling of two-phase behavior in the gas diffusion medium of PEFCs via full morphology approach*. Journal of The Electrochemical Society, 2007. **154**(4): p. B419-B426.
60. Hao, L. and P. Cheng, *Lattice Boltzmann simulations of anisotropic permeabilities in carbon paper gas diffusion layers*. Journal of power sources, 2009. **186**(1): p. 104-114.
61. Becker, J., V. Schulz, and A. Wiegmann, *Numerical determination of two-phase material parameters of a gas diffusion layer using tomography images*. Journal of fuel cell science and technology, 2008. **5**(2): p. 21006.
62. Schulz, V.P., et al., *Numerical Evaluation of Effective Gas Diffusivity-Saturation Dependence of Uncompressed and Compressed Gas Diffusion Media in PEFCs*. ECS Transactions, 2006. **3**(1): p. 1069-1075.
63. *Implicit surfaces*. 1997 [cited 2013; Available from: <http://paulbourke.net/geometry/implicitsurf/>].
64. Wang, Y., *Geometric modeling of nano structures with periodic surfaces*, in *Geometric Modeling and Processing-GMP 2006*. 2006, Springer. p. 343-356.
65. Fishman, J.Z., *Investigation of Surface Properties and Heterogeneity in Gas Diffusion Layers for Polymer Electrolyte Membrane Fuel Cells*, 2010.
66. Bazylak, A., *Liquid water visualization in PEM fuel cells: A review*. International journal of hydrogen energy, 2009. **34**(9): p. 3845-3857.
67. Sinha, P.K., P. Halleck, and C.-Y. Wang, *Quantification of liquid water saturation in a PEM fuel cell diffusion medium using X-ray microtomography*. Electrochemical and Solid-State Letters, 2006. **9**(7): p. A344-A348.
68. Ostadi, H., et al., *3D reconstruction of a gas diffusion layer and a microporous layer*. Journal of membrane science, 2010. **351**(1): p. 69-74.
69. Berejnov, V., D. Sinton, and N. Djilali, *Structure of porous electrodes in polymer electrolyte membrane fuel cells: An optical reconstruction technique*. Journal of Power Sources, 2010. **195**(7): p. 1936-1939.
70. Gao, B., et al., *Visualization of unstable water flow in a fuel cell gas diffusion layer*. Journal of Power Sources, 2009. **190**(2): p. 493-498.
71. Mukherjee, P.P., et al., *Digital Volume Imaging of the PEFC Gas Diffusion Layer*. ECS Transactions, 2010. **33**(1): p. 1483-1491.
72. Zhan, Z., et al., *Effects of porosity distribution variation on the liquid water flux through gas diffusion layers of PEM fuel cells*. Journal of Power Sources, 2006. **160**(2): p. 1041-1048.

73. Mukherjee, P.P., Q. Kang, and C.-Y. Wang, *Pore-scale modeling of two-phase transport in polymer electrolyte fuel cells—progress and perspective*. Energy Environ. Sci., 2010. **4**(2): p. 346-369.
74. Inoue, G., et al., *Development of simulated gas diffusion layer of polymer electrolyte fuel cells and evaluation of its structure*. Journal of power sources, 2008. **175**(1): p. 145-158.
75. Thiedmann, R., et al., *Local structural characteristics of pore space in GDLs of PEM fuel cells based on geometric 3D graphs*. Journal of The Electrochemical Society, 2009. **156**(11): p. B1339-B1347.
76. Wang, X., et al., *Development of hydrophilic barrier layer on nanofibrous substrate as composite membrane via a facile route*. Journal of Membrane Science, 2010. **356**(1–2): p. 110-116.
77. Tamayol, A., F. McGregor, and M. Bahrami, *Single phase through-plane permeability of carbon paper gas diffusion layers*. Journal of Power Sources, 2012. **204**: p. 94-99.
78. Van Doormaal, M.A. and J.G. Pharoah, *Determination of permeability in fibrous porous media using the lattice Boltzmann method with application to PEM fuel cells*. International journal for numerical methods in fluids, 2009. **59**(1): p. 75-89.
79. Hamilton, D., *A numerical method to determine the effective transport coefficient in porous media with application to PEM fuel cells*, 2005, Queen's university.
80. Park, J.W., K. Jiao, and X. Li, *Numerical investigations on liquid water removal from the porous gas diffusion layer by reactant flow*. Applied Energy, 2010. **87**(7): p. 2180-2186.
81. Gaiselmann, G., et al., *Stochastic 3D modeling of fiber-based materials*. Computational Materials Science, 2012. **59**: p. 75-86.
82. Daino, M.M. and S.G. Kandlikar, *3D phase-differentiated GDL microstructure generation with binder and PTFE distributions*. International Journal of Hydrogen Energy, 2011.
83. Thiedmann, R., et al., *Stochastic 3D Modeling of the GDL Structure in PEMFCs Based on Thin Section Detection*. Journal of The Electrochemical Society, 2008. **155**(4): p. B391-B399.
84. Van Genuchten, M.T., F. Leij, and L. Wu. *Characterization and measurement of the hydraulic properties of unsaturated porous media. Parts 1 & 2*. in *Proceedings of the International Workshop, Riverside, Calif., 22–24 Oct. 1997*.
85. Malluche, H.H., D.S. Porter, and D. Pienkowski, *Evaluating bone quality in patients with chronic kidney disease*. Nature Reviews Nephrology, 2013.
86. van Drunen, J., et al., *Comprehensive Structural, Surface-Chemical and Electrochemical Characterization of Nickel-Based Metallic Foams*. ACS Applied Materials & Interfaces, 2013.
87. Rootare, H.M. and C.F. Prenzlów, *Surface areas from mercury porosimeter measurements*. The Journal of physical chemistry, 1967. **71**(8): p. 2733-2736.
88. Kruk, M., M. Jaroniec, and A. Sayari, *Application of large pore MCM-41 molecular sieves to improve pore size analysis using nitrogen adsorption measurements*. Langmuir, 1997. **13**(23): p. 6267-6273.
89. Thiedmann, R., et al., *Random geometric graphs for modelling the pore space of fibre-based materials*. Journal of Materials Science, 2011. **46**(24): p. 7745-7759.



90. Gostick, J.T., et al., *In-plane and through-plane gas permeability of carbon fiber electrode backing layers*. Journal of power sources, 2006. **162**(1): p. 228-238.
91. Gostick, J.T., et al., *Pore network modeling of fibrous gas diffusion layers for polymer electrolyte membrane fuel cells*. Journal of power sources, 2007. **173**(1): p. 277-290.
92. Çeçen, A., et al., *3-D Microstructure Analysis of Fuel Cell Materials: Spatial Distributions of Tortuosity, Void Size and Diffusivity*. Journal of The Electrochemical Society, 2012. **159**(3): p. B299-B307.
93. Dijkstra, E.W., *A note on two problems in connexion with graphs*. Numerische mathematik, 1959. **1**(1): p. 269-271.
94. Dullien, F.A., *New network permeability model of porous media*. AIChE Journal, 1975. **21**(2): p. 299-307.
95. Suchomel, B.J., B.M. Chen, and M.B. Allen, *Network model of flow, transport and biofilm effects in porous media*. Transport in Porous Media, 1998. **30**(1): p. 1-23.
96. Gostick, J.T., et al., *Capillary pressure and hydrophilic porosity in gas diffusion layers for polymer electrolyte fuel cells*. Journal of power sources, 2006. **156**(2): p. 375-387.
97. Lee, K.-J., J.H. Nam, and C.-J. Kim, *Steady saturation distribution in hydrophobic gas-diffusion layers of polymer electrolyte membrane fuel cells: A pore-network study*. Journal of power sources, 2010. **195**(1): p. 130-141.
98. Vogel, H.-J. and K. Roth, *Quantitative morphology and network representation of soil pore structure*. Advances in Water Resources, 2001. **24**(3): p. 233-242.
99. Al-Raoush, R. and C. Willson, *Extraction of physically realistic pore network properties from three-dimensional synchrotron X-ray microtomography images of unconsolidated porous media systems*. Journal of hydrology, 2005. **300**(1): p. 44-64.
100. Al-Kharusi, A.S. and M.J. Blunt, *Network extraction from sandstone and carbonate pore space images*. Journal of petroleum science and engineering, 2007. **56**(4): p. 219-231.
101. Schena, G. and S. Favretto, *Pore space network characterization with sub-voxel definition*. Transport in Porous Media, 2007. **70**(2): p. 181-190.
102. Glantz, R. and M. Hilpert, *Dual models of pore spaces*. Advances in Water Resources, 2007. **30**(2): p. 227-248.
103. Bhamidipati, K.L., et al., *Wetting phenomena during processing of high-viscosity shear-thinning fluid*. Journal of Non-Newtonian Fluid Mechanics, 2011. **166**(12): p. 723-733.
104. Didari, S., et al., *Transport Phenomena in Carbon Paper Gas Diffusion Layers*. ECS Transactions, 2011. **41**(1): p. 499-512.
105. Becker, J., et al., *A multi-scale approach to material modeling of fuel cell diffusion media*. International Journal of Heat and Mass Transfer, 2011. **54**(7): p. 1360-1368.
106. Bird, G., *Molecular gas dynamics and the direct simulation monte carlo of gas flows*. Clarendon, Oxford, 1994.
107. Rapaport, D.C., *The art of molecular dynamics simulation*. 2004: Cambridge university press.

108. He, X., S. Chen, and G.D. Doolen, *A novel thermal model for the lattice Boltzmann method in incompressible limit*. Journal of Computational Physics, 1998. **146**(1): p. 282-300.
109. Shan, X., D. Montgomery, and H. Chen, *Nonlinear magnetohydrodynamics by Galerkin-method computation*. Physical Review A, 1991. **44**(10): p. 6800.
110. Martinez, D.O., et al., *Comparison of spectral method and lattice Boltzmann simulations of two - dimensional hydrodynamics*. Physics of Fluids, 1994. **6**: p. 1285.
111. Swift, M.R., et al., *Lattice Boltzmann simulations of liquid-gas and binary fluid systems*. Physical Review E, 1996. **54**(5): p. 5041.
112. Nourgaliev, R., et al., *The lattice Boltzmann equation method: theoretical interpretation, numerics and implications*. International Journal of Multiphase Flow, 2003. **29**(1): p. 117-169.
113. Kang, Q., et al., *Lattice Boltzmann simulation of chemical dissolution in porous media*. Physical Review E, 2002. **65**(3): p. 036318.
114. Pan, C., M. Hilpert, and C. Miller, *Lattice-Boltzmann simulation of two-phase flow in porous media*. Water Resources Research, 2004. **40**(1): p. W01501.
115. Li, H., C. Pan, and C.T. Miller, *Pore-scale investigation of viscous coupling effects for two-phase flow in porous media*. Physical Review E, 2005. **72**(2): p. 026705.
116. Wang, Q., et al., *A case study of simulating submicron aerosol filtration via lightweight spun-bonded filter media*. Chemical Engineering Science, 2006. **61**(15): p. 4871-4883.
117. Tomadakis, M.M. and T.J. Robertson, *Viscous permeability of random fiber structures: comparison of electrical and diffusional estimates with experimental and analytical results*. Journal of Composite Materials, 2005. **39**(2): p. 163-188.
118. Ascanio, G., B. Taboada, and P.A. Tanguy, *Misting droplet size analysis in a metered film coater*. Chemical Engineering Research and Design, 2008. **86**(2): p. 215-218.
119. Triantafillopoulos, N. and T. Grankvist, *Coating viscoelasticity and blade coating defects*. Paperi ja Puu/Paper and Timber, 1994. **76**(10): p. 663-667.
120. Janes, R.L. and J.D. McKenzie, *The Behavior of Bentonites in Pigmented Paper Coatings-Effects on Rheology, Application, Coated Paper Properties and Printability*, in *TAPPI Coating Conference 1976*: Boston. p. 31-51.
121. Pavlidou, S., et al., *Mechanical Properties of Glass Fabric/Polyester Composites: Effect of Silicone Coatings on the Fabrics*. Journal of Applied Polymer Science, 2004. **91**(2): p. 1300-1308.
122. Hopkins, J., *Nordson: Porous coating with hot melts*. Textile World, 1996. **146**(4): p. 79-80.
123. Ghassemzadeh, J., et al., *Pore Network Simulation of Imbibition into Paper during Coating: I. Model Development*. AIChE Journal, 2001. **47**(3): p. 519-535.
124. Ghassemzadeh, J. and M. Sahimi, *Pore Network Simulation of Fluid Imbibition into Paper During Coating-III: Modeling of the two-phase flow*. Chemical Engineering Science, 2004. **59**: p. 2281-2296.

125. Schrödner, M., et al., *Reel-to-reel wet coating by variation of solvents and compounds of photoactive inks for polymer solar cell production*. Solar Energy Materials and Solar Cells, 2012.
126. Dam, H.F. and F.C. Krebs, *Simple roll coater with variable coating and temperature control for printed polymer solar cells*. Solar Energy Materials and Solar Cells, 2012. **97**: p. 191-196.
127. Larsen-Olsen, T.T., et al., *Simultaneous multilayer formation of the polymer solar cell stack using roll-to-roll double slot-die coating from water*. Solar Energy Materials and Solar Cells, 2012. **97**: p. 22-27.
128. Romero, O.J., et al., *Low-Flow Limit in Slot Coating of Dilute Solutions of High Molecular Weight Polymer*. Journal of Non-Newtonian Fluid Mechanics, 2004. **118**: p. 137-156.
129. Lin, Y.-N., T.-J. Liu, and S.-J. Hwang, *Minimum Wet Thickness for Double-Layer Slide-Slot Coating of Poly (Vinyl-Alcohol) Solutions*. Polymer Engineering and Science, 2005. **45**: p. 1590-1599.
130. Lu, S.-Y., Y.-P. Lin, and T.-J. Liu, *Coating Window for Double Layer Extrusion Slot Coating of Poly (Vinyl-Alcohol) Solutions*. Polymer Engineering and Science, 2001. **41**: p. 1823-1829.
131. Sartor, L., *Slot coating: fluid mechanics and die design*, 1990, University of Minnesota.
132. Devisetti, S.K. and D.W. Bousfield, *Fluid absorption during forward roll coating of porous webs*. Chemical Engineering Science, 2010. **65**(11): p. 3528-3537.
133. Ghassemzadeh, J. and M. Sahimi, *Pore network simulation of fluid imbibition into paper during coating: II. Characterization of paper's morphology and computation of its effective permeability tensor*. Chemical Engineering Science, 2004. **59**(11): p. 2265-2280.
134. Ghassemzadeh, J. and M. Sahimi, *Pore network simulation of fluid imbibition into paper during coating—III: modelling of the two-phase flow*. Chemical Engineering Science, 2004. **59**(11): p. 2281-2296.
135. Wiklund, H. and T. Uesaka, *Microfluidics of imbibition in random porous media*. Physical Review E, 2013. **87**(2): p. 023006.
136. Davard, F. and D. Dupuis, *Blade coating of fabrics: rheology and fluid penetration*. Coloration technology, 2002. **118**(2): p. 69-74.
137. Miller, B. and I. Tyomkin, *Spontaneous transplanar uptake of liquids by fabrics*. Textile Research Journal, 1984. **54**(11): p. 706-712.
138. Yesilalan, H.E., S.B. Warner, and R. Laoulache, *Penetration of Blade-Applied Viscous Coatings into Yarns in a Woven Fabric*. Textile Research Journal, 2010. **80**(18): p. 1930-1941.
139. Letzelter, P. and D. Eklund, *Coating color dewatering in blade coaters. I: Mathematical model and the influence of color parameters*. Tappi journal, 1993. **76**(5): p. 63-68.
140. Letzelter, P. and D. Eklund, *Coating color dewatering in blade coaters. II: The influence of machine configuration*. Tappi journal, 1993. **76**(6): p. 93-98.
141. Chen, K. and L. Scriven, *Liquid penetration into a deformable porous substrate*. Tappi journal, 1990. **73**(1): p. 151-161.

142. Ninness, B., D. Bousfield, and N. Triantafillopoulos. *Fluid dynamics model of the film-fed rolling nip with a porous web*. in *COATING PAPERMAKERS CONFERENCE*. 1998. TAPPI PRESS.
143. Washburn, E.W., *The dynamics of capillary flow*. Physical review, 1921. **17**(3): p. 273.
144. Matthews, P.G.G., C. Ridgway, and P.-S.A. OMYA, *FLUID TRANSPORT INTO POROUS COATING STRUCTURES: SOME NOVEL FINDINGS*. Tappi journal, 2000. **83**(5): p. 42.
145. Schoelkopf, J., et al., *Measurement and network modeling of liquid permeation into compacted mineral blocks*. Journal of colloid and interface science, 2000. **227**(1): p. 119-131.
146. Gribble, C.M., et al., *Porometry, porosimetry, image analysis and void network modelling in the study of the pore-level properties of filters*. Chemical Engineering Science, 2011. **66**(16): p. 3701-3709.
147. Diotallevi, F., et al., *Lattice Boltzmann simulations of capillary filling: Finite vapour density effects*. The European Physical Journal-Special Topics, 2009. **171**(1): p. 237-243.
148. Diotallevi, F., et al., *Capillary filling using lattice Boltzmann equations: The case of multi-phase flows*. The European Physical Journal-Special Topics, 2009. **166**(1): p. 111-116.
149. Pooley, C., H. Kusumaatmaja, and J. Yeomans, *Modelling capillary filling dynamics using lattice Boltzmann simulations*. The European Physical Journal-Special Topics, 2009. **171**(1): p. 63-71.
150. Hyv aluoma, J., et al., *Simulation of liquid penetration in paper*. Physical Review E, 2006. **73**(3): p. 036705.
151. Rofaie, A., et al., *Heterogeneous through-plane distributions of polytetrafluoroethylene in polymer electrolyte membrane fuel cell gas diffusion layers*. Journal of Power Sources, 2012. **201**: p. 219-225.
152. Huang, W., et al., *Modeling of Porous Media with Periodic Surfaces*. Engineering Computations, 2012.
153. Zhao, P., et al., *Nickel foam and carbon felt applications for sodium polysulfide/bromine redox flow battery electrodes*. Electrochimica Acta, 2005. **51**(6): p. 1091-1098.
154. Dicks, A.L., *The role of carbon in fuel cells*. Journal of Power Sources, 2006. **156**(2): p. 128-141.
155. *Image Processing Toolbox - MATLAB - MathWorks*. 2013; Available from: [www.mathworks.com/products/image/](http://www.mathworks.com/products/image/).
156. Didari, S., Y. Wang, and T. Harris, *Virtual Modeling of Composite Fibrous Porous Diffusion Media*. International Journal of Hydrogen Energy, 2013: p. under review.
157. ANSYS-FLUENT, *User Guide*, 2009.
158. Clague, D.S. and R.J. Phillips, *A numerical calculation of the hydraulic permeability of three-dimensional disordered fibrous media*. Vol. 9. 1997: AIP. 1562-1572.
159. Clague, D.S., et al., *Hydraulic permeability of (un)bounded fibrous media using the lattice Boltzmann method*. Physical Review E, 2000. **61**(1): p. 616.

160. Feser, J., A. Prasad, and S. Advani, *Experimental characterization of in-plane permeability of gas diffusion layers*. Journal of Power Sources, 2006. **162**(2): p. 1226-1231.
161. *Freudenberg FCCT Kg webpage* 2013; Available from: [http://www.freudenbergfcct.com/GDL%20Technical%20Data%20and%20Recommendation\\_engl\\_2010.pdf](http://www.freudenbergfcct.com/GDL%20Technical%20Data%20and%20Recommendation_engl_2010.pdf).
162. Bhamidipati, K., S. Didari, and T.A. Harris, *Experimental Study on Air Entrainment in Slot Die Coating of High-Viscosity, Shear-Thinning Solutions*. Chemical Engineering Science, 2012.
163. Bhamidipati, K.L. and T.A. Harris, *Numerical analysis of defect formation during fabrication of high temperature polymer electrolyte membrane solutions*. Polymer Engineering & Science, 2011. **51**(9): p. 1701-1709.
164. Didari, S., et al., *Wetting behavior of the shear thinning power law fluids*. Journal of Coatings Technology and Research, 2013: p. 1-8.
165. Wang, Y., *Periodic surface modeling for computer aided nano design*. Computer-Aided Design, 2007. **39**(3): p. 179-189.
166. Mathias, M., et al., *Diffusion media materials and characterisation*. Handbook of fuel cells, 2010.